

# Physics of Oocyte Growth and Selection

**A mesoscopic perspective**

DISSERTATION

zur Erlangung des akademischen Grades

Doctor rerum naturalium

vorgelegt

dem Bereich Mathematik und Naturwissenschaften  
der Technischen Universität Dresden

von

Arghyadip Mukherjee  
geboren am 17.10.1993 in Asansol

Max-Planck-Institut für Physik komplexer Systeme  
Zentrum für Systembiologie Dresden  
Max-Planck-Institut für molekulare Zellbiologie und Genetik  
Technische Universität Dresden

Dresden, 2020

Eingereicht am 11. November 2020

Verteidigt am 22. February 2021

Gutachter:

Prof. Dr. Frank Jülicher co-signed by Prof. Dr. Stephan W. Grill

Prof. Dr. Karsten Kruse







”I suspect that the fate of all complex adapting systems in the biosphere,  
from single cells to economies  
–is to evolve to a natural state between order and chaos,  
a grand compromise between structure and surprise. ”

— **Stuart Kauffman** in *At home in the universe*

Dedicated to the memory of  
**Stephen Jay Gould.**  
*(1941-2002)*



# Acknowledgements

Scientific endeavor is a social one, for there is very little joy in a discovery if not shared. More than anything, I am grateful towards my supervisors Frank Jülicher and Stephan Grill for this experience of a lifetime. I am thankful to Stephan for opportunity, guidance, feedback, help and criticism and also for broadening my mind to my own future. Much of my scientific personality has developed over my interactions with Stephan, for that I shall always be grateful. I am grateful for the careful guidance of Frank, for teaching me the value of science in our lives. I am thankful to Frank for allowing me the freedom to develop my own scientific rhythm and most importantly taste, while grounding my imagination with rigor as often as it was necessary. Along with my thanks I shall also offer my apologies for causing sleepless nights. I cannot imagine this unique learning experience without the presence of you both.

I would like to thank the close colleagues that I have learnt the most from, Nicolas, Keisuke, Teije, who held my hand and walked me into the fascinating world of the living, a gift I can hardly repay. Over the years I have worked closely and learnt from Julia, Sebastian, Rana, Akanksha, all of whom I thank. I would like to acknowledge valuable comments, discussions and support from Jan Brugues who has not only played a crucial role as a committee member but also as a mentor.

I have had the pleasure of sharing the environment of a few beautiful institutes and groups. I would like to acknowledge the very engaging environment of the Biological Physics group at MPI-PKS, especially the members of the PhD seminars. I would like to thank the current and past members of the Grill lab that I overlapped with and learnt from. I would like to thank the Brugues lab for exceptional hospitality and friendship. Overall I would like to thank the members of the MPI-CBG and fellow PhD students of the IMPRS who have over the years influenced my thinking to a great degree.

I would like to thank the administration of the institutes (MPI-PKS, MPI-CBG) for help in making my life easier. I would like to thank Ulrike Burkert for making my life easier with administration. Over the years I have received exceptional support from Ulrike, without which I suspect I would be caught in a spider web of my own making. I would like to thank my family and friends, without whom this endeavor seems futile. I have always had the privilege of having kind people in my life, whom I have done very little to deserve and often less so to keep. As I look back at my time here, I find it rich in friendship, kindness, laughter and love. I shall not point out each person individually to avoid missing someone out of this long and special list. Nonetheless it would be amiss to not mention my closest friends Keisuke, Lora, Niladri, Rekha, Rohit, Martin, who collectively preserve the remnants of my sanity. I would like to thank my sister and brother in law for their love and support. I would like to thank my grandparents for a wonderful influence during my childhood. I would like to thank

my mother without whose love and constant effort, I would not amount to anything. At last I would like to thank my father for love, guidance, sense of humor and whose relentless curiosity and unshakable determination inspire me everyday.

Collaboration note:

I would like to thank Dr. Nicolas Chartier for this close collaborative work and for providing experimental data used in this thesis. Details regarding the methods of data acquisition can be found in [1].

# Abstract

To live is to reproduce. The propensity to pass on essential genetic identity to progeny is fundamental to all forms of life. As living organisms have evolved in structure and complexity, the mechanisms that arbitrate and safeguard this inheritance also have evolved, often in the form of unique cells, called gametes. A vast majority of multicellular organisms reproduce via formation of oocytes (oogenesis). The process of oogenesis across species shows remarkable similarity and a crucial step is the isolation and individualization of germ cells fated to carry on this essential role. Amidst a seemingly homogeneous population of germ cells that share cytoplasm within a syncytial structure, hence also their chemical identity, how a select subset of cells are robustly identified is a puzzling phenomena that has troubled developmental biology for decades. We find the answer in the underlying physical interactions of these cells with its environment in the context of the nematode *Caenorhabditis elegans*. These cells behave as tiny non-equilibrium elements as they pump cytosol from outside and fill in the cytoplasmic luminal core "rachis" generating flows at long lengthscales. Later along the germ line, the disappearance of such external sources reduce the pressure difference of the cells and rachis, eventually leading to an inversion of pressure difference. This inversion in turn reverses direction of the cytoplasmic exchange and lead to an inflation mediated growth phase of germ cells. We derive a minimal physical framework to identify and evaluate the stability of such growth phases. We find that such inflation driven growth is inherently unstable and lead to coarsening/condensation, amplifying small differences in volumes between connected cells leading to increasingly disparate population of cells, an instability mediated by tissue hydraulics. This bears fundamental similarity to coarsening of connected soap bubbles where due to curvature driven forces symmetric configurations are unstable. Here however using dynamic pumping from outside, such symmetric configurations are stabilized actively, a feature that is truly non-equilibrium. This alludes to that grown cells then become future oocytes and the shrunken ones apoptose and are removed. We test these ideas by comparing to experiments and find strong agreement, furthermore using genetic techniques we predict the existence of the instability independent of apoptotic pathways under predicted flow fields. The persistence of such a volume instability under elimination of apoptosis along with excellent agreement of predicted and experimental flow field consolidates our abstract yet simple idea of instability driven heterogeneity of growth and shrinkage. This presents a novel and fresh outlook to this decade old problem, where the cell fates are not robustly selected but are rather emergent via hydrodynamic interactions. It is fascinating to identify such a unique physical mechanism where the eventual fate of the germ cells are determined in response to flow/pressure fields that are in turn generated by a constantly replenishing pool of germ cells that constitute the germline. The decision making hence truly is emergent out of interactions and activity of these

constituent cells. This presents an excellent example of self-organized decision making exploiting a symmetry breaking transition of the underlying physical structure.

Spontaneous symmetry breaking, a conceptual pillar of modern physics, provides a new perspective on questions of decision making and questions of selection. Starting from our hydrodynamic model of symmetry-breaking we provide a mapping to evolutionary dynamics. This derivation is one of its kind, where fundamental equations of evolutionary dynamics are derived from basic principles of hydrodynamics rather than phenomenologically written down. This combines remarkably the aesthetics of evolutionary dynamics with the strength of physical intuition and interpretation. Together we bring forth an elegant theoretical framework that bridges various concepts and formalisms of hydrodynamics, mechanics and evolutionary dynamics to discover a novel physical strategy that underlies a fundamental decision of life and death of germ cells.

# Contents

<b>List of Figures</b>	<b>xiii</b>
<b>1 Introduction</b>	<b>1</b>
1.1 Morphogenesis: forces that shape life . . . . .	1
1.1.1 Mechanics of living matter . . . . .	1
1.1.2 Dynamics of biological fluids . . . . .	4
1.2 Oogenesis : the stepping stone of complex life . . . . .	8
<b>2 Biophysical measurements of germline homeostasis</b>	<b>10</b>
2.1 Growth and motion of germ cells along the germline . . . . .	11
2.1.1 Homeostasis of <i>C.elegans</i> germline . . . . .	11
2.1.2 Motion and maturation of germ cells . . . . .	14
2.1.3 Growth of germ cells along the germline . . . . .	17
2.1.4 Statistics of germ cell volumes along the germline . . . . .	19
2.1.5 Homogeneous and heterogeneous growth modes of germ cells . . . . .	26
2.2 Flow fields within the germline . . . . .	28
2.2.1 Volume flux through the rachis . . . . .	29
2.2.2 Cell volume flux . . . . .	32
2.2.3 External source current . . . . .	34
2.3 Conclusion . . . . .	35
<b>3 Biophysical theories of the germline dynamics</b>	<b>37</b>
3.1 Hydrodynamics of the germline . . . . .	38
3.1.1 1 D hydraulic description . . . . .	39
3.1.2 Hydrodynamic flows through rachis bridges . . . . .	40
3.1.3 Solutions to simplified geometries . . . . .	43
3.2 Germline Mechanics and Stability of Symmetric States . . . . .	50
3.2.1 Radial mechanics of the germline tissue . . . . .	50
3.2.2 Azimuthal stability of a germ-cell doublet . . . . .	54
3.2.3 Axial stability of germ cells . . . . .	61
3.3 Hydraulic symmetry breaking and theory of oogenic growth . . . . .	64
3.4 Cooperation, conflict and altruism . . . . .	66
3.5 Conclusion . . . . .	72
<b>4 Summary</b>	<b>73</b>
<b>Appendices</b>	

<b>A</b>	<b>Germ cell nuclear growth and allometry</b>	<b>78</b>
A.1	Nuclear growth . . . . .	78
A.2	Allometric scaling and proportional growth . . . . .	78
A.3	Conclusion . . . . .	81
<b>B</b>	<b>Viscous steady flow through a pipe</b>	<b>83</b>
B.1	Viscous flow through an ideal pipe . . . . .	83
B.2	Influence of curvature on Poiseuille flow . . . . .	87
B.3	Influence of slip on Poiseuille flow . . . . .	87
B.4	Viscous flow through a leaky pipe . . . . .	89
	<b>Bibliography</b>	<b>91</b>



# List of Figures

1.1	Vertex model of tissue geometry . . . . .	3
1.2	Cell extrusions drive tissue folding . . . . .	4
1.3	Cytoplasmic streaming across species . . . . .	5
1.4	Cortical flow in <i>C.elegans</i> single cell zygote . . . . .	8
1.5	Germariums of various species . . . . .	9
2.1	Gonadogenesis in <i>C.elegans</i> . . . . .	11
2.2	Germ cell number over time . . . . .	12
2.3	Germline in <i>C.elegans</i> . . . . .	13
2.4	Birth and death profile of germ cells . . . . .	15
2.5	Mean germ cell density . . . . .	16
2.6	Estimated germ cell velocity . . . . .	16
2.7	Germ cell volumes along the germline . . . . .	17
2.8	Mean cell volumes along the germline . . . . .	18
2.9	Growth rates of germcells . . . . .	19
2.10	Emergence of bimodal germ cell volumes . . . . .	20
2.11	Std. of Germ cell Volumes . . . . .	21
2.12	CV of Volumes . . . . .	21
2.13	Crossover . . . . .	22
2.14	Collapse of distal volume distributions . . . . .	23
2.15	Normalized volume distributions along DP axis . . . . .	23
2.16	Skewness of cell volumes . . . . .	24
2.17	CDF of cell volumes . . . . .	25
2.18	Inequality indices . . . . .	27
2.19	Schematic of the germline . . . . .	28
2.20	Flow profile within the rachis . . . . .	30
2.21	Spatial profile of cytoplasmic flux through rachis . . . . .	31
2.22	Germ cell to rachis current . . . . .	32
2.23	Cross-sectional tissue area . . . . .	33
2.24	Cell volume flux . . . . .	34
2.25	Profile of source . . . . .	35
3.1	Schematic of flows in the germline . . . . .	39
3.2	Schematic of a germ cell . . . . .	41
3.3	Fluxes with stepwise linear source . . . . .	46
3.4	Fluxes with stepwise source with leakage . . . . .	47
3.5	Tuning rachis flux with relative friction . . . . .	47
3.6	Theoretical fits to measured fluxes . . . . .	48

3.7	Theoretical and experimental current profile . . . . .	49
3.8	Radial mechanics of the germline . . . . .	51
3.9	Work function for radial stability . . . . .	52
3.10	Phase diagram for radial stability . . . . .	53
3.11	Germ cell doublet schematic . . . . .	54
3.12	Azimuthal Stability of cell doublet . . . . .	56
3.13	Kinetics of homogenization . . . . .	57
3.14	Kinetics of symmetry breaking . . . . .	57
3.15	Potential function for stability . . . . .	58
3.16	Position of symmetry-broken state . . . . .	59
3.17	Stability of germ cell doublet with offset . . . . .	60
3.18	Axial stability when $\tilde{p} > 0$ . . . . .	62
3.19	Axial stability when $\tilde{p} < 0$ . . . . .	63
3.20	Scheme of symmetry breaking in the germline . . . . .	64
3.21	Nonapoptotic germline shows hydraulic instability . . . . .	65
3.22	Stability for $N=30$ and $\epsilon_p = +ve$ . . . . .	67
3.23	Stability for $N=300$ and $\epsilon_p = +ve$ . . . . .	67
3.24	Stability for $N=30$ and $\epsilon_p = -ve$ . . . . .	68
3.25	Stability for $N=300$ and $\epsilon_p = -ve$ . . . . .	68
A.1	Profile of germ cell nuclear volume . . . . .	78
A.2	Allometric scaling of nuclear volume . . . . .	79
A.3	CV of nuclear volumes . . . . .	81
B.1	Pipe flow . . . . .	84
B.2	Flow in curved pipes . . . . .	87
B.3	Flow in leaky pipes . . . . .	90

# Chapter 1

## Introduction

The academic scrutiny of the physical world around us, is not only driven by relentless curiosity but also by confusion and aesthetics. A fundamental question that has puzzled all scientists alike, is the question of morphogenesis - how a simple and often spherical bag of biology grows, deforms, compartmentalizes to increasingly complex functional structures - from water lilies to elephants. Achieving all of this with remarkable reproducibility while battling fluctuations and variation at multiple scales of length and time is a herculean task that an embryo must attain everytime without fail. The mysteries of this perennial phenomena has sparked scientific research over centuries – from biochemists that strive to understand the molecular basis of life [2–4] to physicists and applied mathematicians that are drawn by the aesthetic questions of shape, size and symmetry [5–7]. The latter of which, we enthusiastically share.

This chapter serves to introduce some essential concepts and questions later invoked in this thesis and the philosophy with which we approach these questions.

### 1.1 Morphogenesis: forces that shape life

The study of morphogenesis encompasses the elements that conspire together to build an organ and organism reproducible in shape and size. We shall limit our discussion to multicellular organisms, where a plenitude of cells emerge out a single cell zygote to give rise to variety of structures and functions. The ability of constituent cells to move, grow, change shape, sense and respond enables biological tissues and organisms to dynamically create self-organized patterns of geometry. The changes of geometry must follow forces that drive them. Hence a notable amount of work is done understanding how form follows force, at short as well as long timescales. A significant advance in this field comes from careful experiments that established the basis of force generation at a cellular scale by the cytoskeletal elements (reviewed in [8–10]). This has allowed various physical theories to be tested with simple perturbations, providing more convincing evidences than mere correlations. We shall discuss this with few simple examples.

#### 1.1.1 Mechanics of living matter

A simple yet powerful view is to understand a biological structure as a static one, considering the geometry and mechanics with an equilibrium-like framework. This

argument holds true with a quasi-steadystate approximation, which is essentially a study of short time-scales. In that case we seek to evaluate the minima of a pseudo-potential, an analogue for free energy of a system with hidden variables. Say the structure of our choice is represented by position vector of  $N$  special points, which is sufficient to describe the structure, here the minima of the pseudo-potential  $W$  will yield structures that should transpire naturally as they are favored energetically. Although no global minima may exist, it allows us to prescribe dynamical rules to study how shapes emerge and behave over time,

$$\frac{\partial \vec{x}_i}{dt} = -\frac{\partial W}{\partial \vec{x}_i} \quad \forall i \quad (1.1)$$

where  $\vec{x}_i$  denotes the position vector of the  $i^{\text{th}}$  special particle and pseudo-potential  $W$  may include terms such as surface energy, volume energy, edge tension etc. In this spirit a class of models called vertex models have been successfully implemented to understand various biological structures and problems [11–13] (reviewed in [14]). Let us discuss the case of [13] where the authors consider a two dimensional lattice of points, namely the junctions of cells. Cell edges that connect these junctions are assumed to be straight and no curvature energy is used. The proposed pseudo-potential is,

$$W = \sum_{\alpha \in \mathbf{C}} \frac{K_\alpha}{2} (A_\alpha - A_\alpha^0)^2 + \sum_{\langle ij \rangle} \Lambda_{ij} l_{ij} + \sum_{\alpha} \frac{\Gamma_\alpha}{2} L_\alpha^2 \quad (1.2)$$

where for each cell  $\alpha \in \mathbf{C}$  the first term captures the elastic penalty as the cell area  $A_\alpha$  deviates from the target area  $A_\alpha^0$  with an elastic modulus  $K_\alpha$ ; the second term merely is a edge energy which wants to shrink cell edges of length  $l_{ij}$  that connect vertex  $i$  &  $j$  with line-tension  $\Lambda_{ij}$ , which is balanced by a global constraint term of perimeter  $L_\alpha$  elasticity of elastic coefficient  $\Gamma_\alpha$ . For a homogeneous system an order-disorder transition is found (see Fig.1.1). For negative reduced line tension and low reduced contractility the groundstate is degenerate and yields many floppy modes and one can deform the structure at no energy cost. Beyond this region the two dimensional lattice is stiff and hexagonal and fluctuations around this state maintain average connectivity number to be 6. This idea was extended with a simulation framework to compare with a very dynamic tissue of *Drosophila m.* wing epithelium where cell division, extrusions as well local non-affine movements of cells may disrupt such hexagonal order and excellent agreement in prediction and experiments of cellular order and packing revealed the strength of such a reductionist approach. An alternative point of view and framework of the same cellular packing problem can be found in [15].

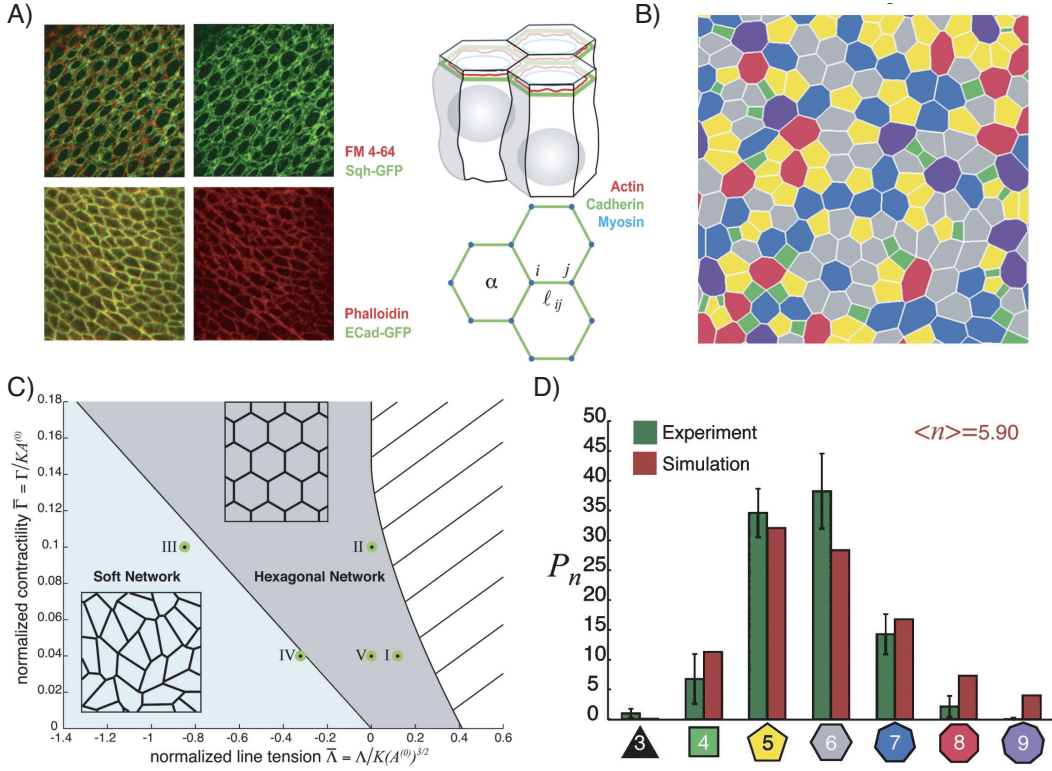


**Figure 1.1:** A) Tissue geometry is shown for the *Drosophila m.* wing epithelium. B) Snapshot of vertex model simulations. C) Phase diagram of vertex model predicts an order-disorder transition. D) Comparison of predicted and experimentally observed cell packing statistics. *Adapted from [13]*

These concepts can be generalized to a three dimensional structure [16], where one must introduce a pressure related term as a Lagrange multiplier for the volume constraints. Surface tensions  $T_s$  and edge tensions can be accounted for in a similar spirit. The pseudo-potential then modifies to,

$$W = \sum_{\alpha \in \mathbf{C}} \frac{K_\alpha}{2} (V_\alpha - V_\alpha^0)^2 + \sum_{s \in \mathbf{S}} T_s A_s + \sum_{\langle ij \rangle} \Lambda_{ij}^{(a,b)} l_{ij}^{(a,b)} + \delta W_{ext} \quad (1.3)$$

where similar to area elasticity in the two dimensional case a volume elasticity/control term is introduced as the first term with target volume  $V_\alpha^0$  and "bulk" modulus  $K_\alpha$ . It is a valuable realization that in principle this general idea can be extended to any sort of constitutive relationships of geometric factor and their corresponding forces. For example, the volume constraint demands only a simple Lagrange multiplier  $P$  and introduces a term  $-PV$ , in which case we can demand that the cell volume with a specific shape is  $V$  and evaluate the corresponding  $P$  that is necessary to satisfy that minima, this is a hard constraint which can be relaxed with the proposed constitutive relationship  $P_\alpha = -K_\alpha(V_\alpha - V_\alpha^0)/2$ , which is implemented here. The hard constant can be recovered in the limit  $K_\alpha \rightarrow +\infty$ . Any number of such relations can be written to capture basic elements of the system at hand.

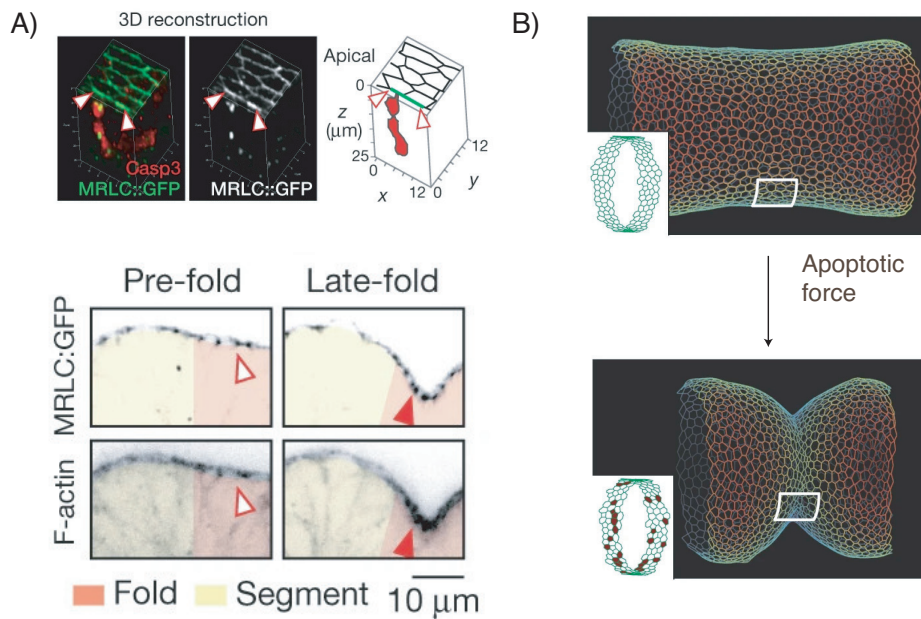


**Figure 1.2:** A) Apico-basal asymmetries in apoptotic cells are indicated and as a result local folding of the tissue. B) A 3D vertex model confirms the mechanism of folding due to extrusions. *Adapted from [17]*

Using such framework one can study the influence of various cellular events and forces on three-dimensional shape. One beautiful example is found in folding of an epithelia driven by polarized extrusion of cells out of the tissue, which generates out-of-plane stresses [17].

Let us discuss the case of volume control in further detail. The volume elasticity term is motivated by two essential elements, 1) cytoplasm is a fluid with low compressibility 2) cells sense and respond to changes in volume. Both of these arguments rely on existence of well defined boundaries of the cell. As we shall see in this thesis, this often may not be the case and may have fascinating non-equilibrium effects that originate from it.

### 1.1.2 Dynamics of biological fluids

On the other end biology presents us with systems that grow, evolve, flow in observable timescale and in such cases very little can be understood from a static point of view. In this section we shall discuss how various biological processes depend on fluid flows and basic concepts required to think about fluids. A conserved physical phenomena across species is protoplasmic streaming [18], originally reported first by Corti (1774). Cytoplasmic streaming can originate from various underlying physical mechanisms and may materialize in complex flow patterns (reviewed in [19]).

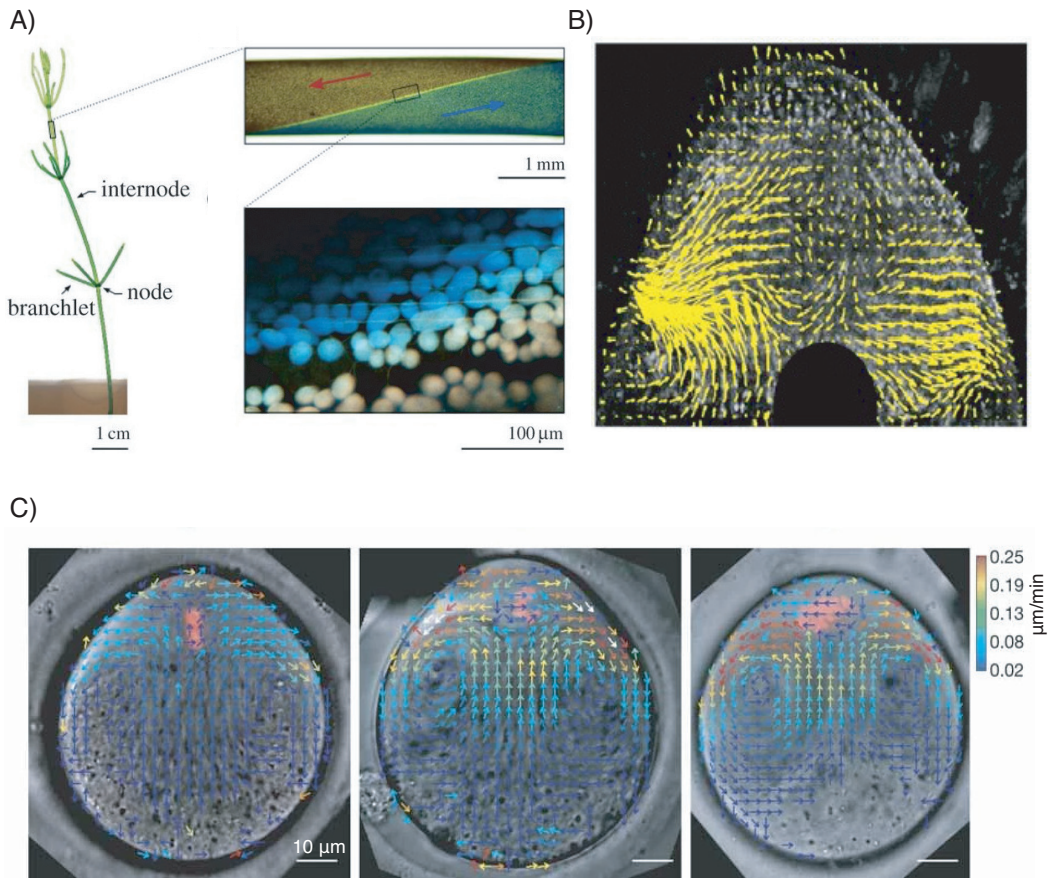


**Figure 1.3:** A) Cytoplasmic streaming in a plant, driven by active shear flow. Adapted from [19]. B) Cytoplasmic streaming within *D.melanogaster* oocyte. Adapted from [20] C) Cytoplasmic streaming within the mouse embryo. Adapted from [21]

It is widely thought that cytoplasmic streaming mediate various biological function e.g. chemical dispersion across long distances, homogenization of cytoplasm etc. The study of fluid flows is inherently the study of the associate velocity field. The governing equation for fluids is the celebrated Navier-Stokes equation [22]. Let us consider a volume element of fluid with Eulerian velocity field  $\vec{v}(\vec{x}, t)$  at position  $\vec{x}$ . The total time derivative following the fluid motion,

$$\frac{d}{dt} = \frac{\partial}{\partial t} + \vec{v} \cdot \nabla$$

can be expressed as a sum of the local rate of change  $\partial/\partial t$  and the advective rate of change  $\vec{v} \cdot \nabla$ , which occurs as the volume element moves through gradient. An important realization is that the acceleration of a fluid is,

$$\frac{d\vec{v}}{dt} = \frac{\partial\vec{v}}{\partial t} + \vec{v} \cdot \nabla\vec{v}$$

where the second term is non-linear in  $\vec{v}$ , turning out to be the fundamental difficulty in

solution of problems in fluid dynamics. We shall derive the equations of fluid dynamics. Starting from consideration of mass conservation, let us denote  $\rho(\vec{x}, t)$  as the density. Then,

$$\frac{\partial \rho}{\partial t} + \nabla \cdot (\rho \vec{v}) = 0 \quad (1.4)$$

which can also be expressed as,

$$\nabla \cdot \vec{v} = -\frac{1}{\rho} \frac{d\rho}{dt} \quad (1.5)$$

This can be interpreted as the incompressibility condition, where negligible changes in density equate to  $\nabla \cdot \vec{v} = 0$ . The conservation of momentum demands,

$$\rho \frac{d\vec{v}}{dt} = \rho \left( \frac{\partial \vec{v}}{\partial t} + \vec{v} \cdot \nabla \vec{v} \right) = \nabla \cdot \sigma + \rho \vec{f} \quad (1.6)$$

where  $\sigma$  is the stress tensor and  $\vec{f}$  is external body force. In the case of an incompressible viscous ideal fluid,

$$\rho \left( \frac{\partial \vec{v}}{\partial t} + \vec{v} \cdot \nabla \vec{v} \right) = -\nabla p + \eta \nabla^2 \vec{v} + \rho \vec{f} \quad (1.7)$$

where  $p$  is the hydrodynamics pressure and  $\eta$  is the shear viscosity. In viscosity dominated regimes the inertial terms drop out and we obtain the Stoke's equation that describe steady flow fields,

$$\nabla p = \eta \nabla^2 \vec{v} \quad (1.8)$$

Virtually all biological flows are viscosity dominated and Stoke's equation provides us with a convenient framework to study them. One must comment that the geometry and boundary conditions play crucial roles in determining the flow fields. Application of fluid dynamics in biology is age-old and originates from physiology. The flow of blood through our vascular system is one the first physiological hydrodynamic problem that fascinated scientists. One can assume our vasculature to be ideal cylinder and compute discharge rate and it's relationship to the geometry. This is given by the Hagen-Poiseuille's law (for a discussion see Appendix B.),

$$Q = \frac{\pi R^4}{8\eta} \frac{\Delta p}{l} \quad (1.9)$$

where  $R$  &  $l$  are respectively the radius and length of the capillary and  $\Delta p$  the pressure difference between two ends. Now if the capillary dilates or expands by a factor of  $\epsilon$  as  $R \rightarrow R(1+\epsilon)$  the total discharge  $Q \sim R^4(1+\epsilon)^4$  implying  $Q/Q_o \sim (1+4\epsilon)$ . Hence for a mere 5% change in radii a 20% effect is expected.

Another lesson one can learn from the study of ideal fluids is about incompressibility, which we simply assumed so far. Let us assume that the density varies with pressure as  $\rho(p)$ . The incompressibility of a flow is simply the statement that changes of density



due to flow via pressure changes are negligible. Given such pressure changes in flow we can write,  $\Delta\rho = d\rho/dp\Delta p$  and in isothermal conditions,  $dp/d\rho = c^2$  where  $c$  is the isothermal speed of sound ( $\sim 10^3$  m/s for water). Hence we find,

$$\frac{\Delta\rho}{\rho} = \frac{\Delta p}{\rho c^2} \quad (1.10)$$

For moderate to high-Reynolds number flows with characteristic velocity  $v_0$ , we have  $\Delta p \simeq \rho v_0^2$ , hence the incompressibility assumption should hold when,

$$\frac{\Delta\rho}{\rho} = \frac{v_0^2}{c^2} \ll 1 \quad (1.11)$$

As a result virtually all flows at physiological scale are incompressible.

Biological fluids are inherently active and may develop stresses due to complex biochemical processes that generate local stresses. Moreover there could be many broken symmetry variables that introduce new hydrodynamic fields and hence cross-couplings that can give rise to a rich variety of phenomena unforeseen in simple abiotic matter. This is an active area of research, for an elaborate discussion see [23–27].

The cortex is a thin layer of condensed phase of cytoskeletal matter just beneath the cell membrane. It is already interesting how such a condensed phase may be stable being embedded within the bulk cytoplasm and whether it bears similarity to a wetting layer [28]. The active gel theory of the cortex captures shape changes [29], cell motility [30, 31], cell divisions [32, 33] with great success. We shall consider a simple yet elegant example of such an active fluid - actomyosin cortex of the *C.elegans* single cell zygote. Here an anterior posterior gradient of myosin is seen to drive polarizing flows.

The force balance can be written as,

$$\partial_x T = f \quad (1.12)$$

where  $T$  is the two dimensional in-plane stress and  $f$  is the external force. Let's assume that the external force purely due to friction  $\gamma$  with the surface outside  $f = \gamma v$  where  $v$  is the velocity of the thin film. Under a viscous thin film approximation one can assume,

$$T(x) = \beta C(x) + \eta \frac{\partial v}{\partial x} \quad (1.13)$$

where the first term accounts for activity and  $C(x)$  denotes the concentration of active force generating elements (here Myosin) and the second term is purely viscous dissipation. As a result we obtain,

$$\beta \frac{\partial C}{\partial x} = -\eta \frac{\partial^2 v}{\partial x^2} + \gamma v \quad (1.14)$$

which related the gradient of molecular force generator to a macroscopic flow field. This equation along with its' extension have successfully captured the effective physics of various morphogenetic processes e.g. cortical flow in nematode embryo [34–36], mor-

phogenetic flows in flies [37] and beetles [38], emphasizing the importance of effective field theories in morphogenesis.

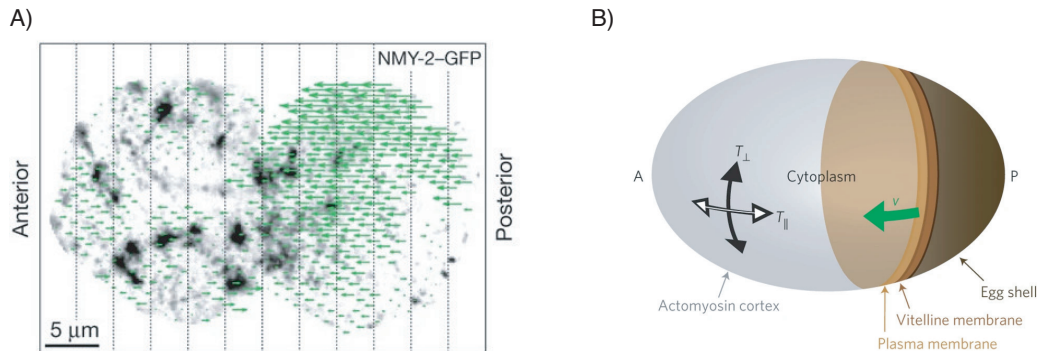


**Figure 1.4:** A) Velocity field of cortical flows in Posterior to Anterior direction is shown for *C.elegans* single cell zygote. B) A schematic model depicts how anisotropic tension underlies symmetry breaking flows in the cell. *Adapted from* [34]

## 1.2 Oogenesis : the stepping stone of complex life

Oogenesis is a fundamental morphogenetic process that sets the basis of all future developmental events of an organism. Although born as regularly sized germ cells, oocytes undergo tremendous growth during their maturation from germ cells and are one of the largest cells in an organism. Amongst many species the germ cells develop into future oocytes as part of a syncytial architecture, sharing a common cytoplasmic pool. Both male and female germcells of a wide variety of animal (vertebrate and invertebrate) species develop within a syncytial structure. The prevalence of structural similarities and stereotypic maturation steps of germ cells argue possibly for a conserved mechanism (reviewed in [39–42] ).

The ultimate growth of some germ cells into oocytes is often achieved at the expense of other germ cells, where cytoplasmic partitioning between these connected cells become disparate and unequal. This in turn creates population of shrinking germ cells that contribute cytoplasm to the growing oocyte and are eventually removed via apoptosis. This poses an interesting mystery of how, out of a seemingly homogeneous population of connected cells that share a common chemical identity embedded in the cytoplasmic pool, some cells individualise into growing oocytes and some into shrinking cells. One may think of this as a symmetry breaking phenomena, where the original symmetry of the system where all cells are seemingly equivalent, is lost in the course of maturation. While many factors may play important role in the maintenance and disappearances of such symmetries of a living and growing organ over time, certain simplifications can yield fundamental insights into this perplexing phenomena. This process of growth and cytoplasmic redistribution within such a syncytial tissue involve bulk flows/exchange of cytoplasm and poses interesting aspect of tissue hydraulics.

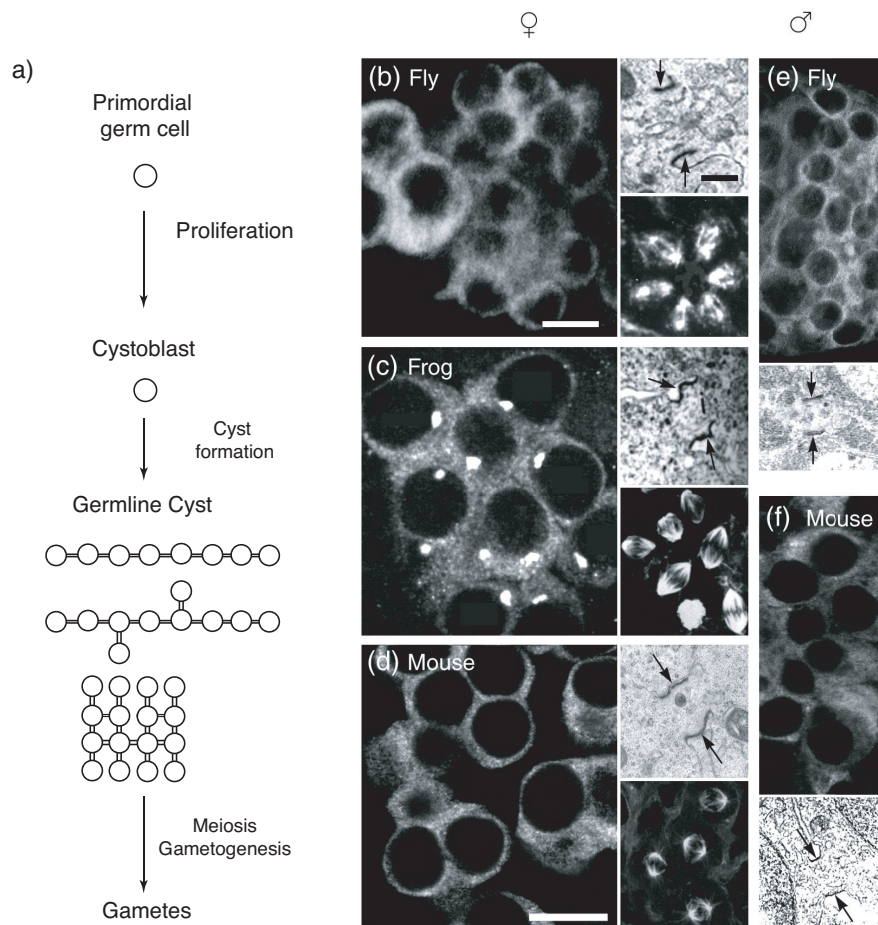


**Figure 1.5:** Germline development proceeds in stereotypic steps across species. (A) Demonstrates generic developmental stages of germline cyst growth. (B-D) shows ovaries of *Drosophila m.*, *Xenopus l.* and mouse. (E-F) shows *Drosophila* and mouse testis. (B, D, E, F) are stained with corresponding germ cell markers and (C) is stained with gamma-tubulin. Top insets (B-D) and insets in (E-F), are electron micrographs from each species. Bottom insets (B-D) show synchronous germ cell division for each species. Adapted from [41].

In the following chapters we will address this fundamental question of embryology borrowing and developing concepts of hydrodynamics and hydraulics and discuss the physical basis of such a symmetry breaking event in the context of nematode *C. elegans*.

# Chapter 2

## Biophysical measurements of germline homeostasis

Across species germ cells develop into oocytes within syncytial architecture going through stages of maturation and tremendous growth. This tremendous growth of the future oocytes is often achieved at the expense of shrinkage of connected sister germ cells, which are eventually eliminated by apoptosis. This conserved feature of germ cells across species, where a seemingly homogeneous population of cells sharing a common cytoplasm and hence an equivalent chemical identity, diverge into two distinct fates- one that grow and lives on and the other that shrinks and is discarded. This essential cell fate decision of life and death of a germ cell is intertwined with the physical transition of growth and shrinkage.

In this chapter, we investigate the underlying growth kinetics and hydrodynamics of germ cells connected within the syncytial germline of adult hermaphrodite *C.elegans* to understand better this divergent cell fates from the perspective of growth and shrinkage. Using state of the art microscopy and image analysis, we quantify and infer cell volumes, discharge rates, fluid flux etc. From these quantities we further extract physically meaningful quantifiers, that help us build a physical description of germ cell growth and shrinkage. In the first half, signatures of growth and variation of germ cell volumes is discussed applying various statistical methods. The later half emphasizes on understanding the material basis of such growth and variation by applying concepts of fluid dynamics.

For the rest of this thesis, while discussing oocyte growth we shall simply limit ourselves to the volume of cytoplasmic matter contained rather than its content. It is noteworthy that naturally various biochemical aspects as well as sub-cellular contents evolve during the life of a germ cell, for a discussion see Appendix A.

## 2.1 Growth and motion of germ cells along the germline

### 2.1.1 Homeostasis of *C.elegans* germline

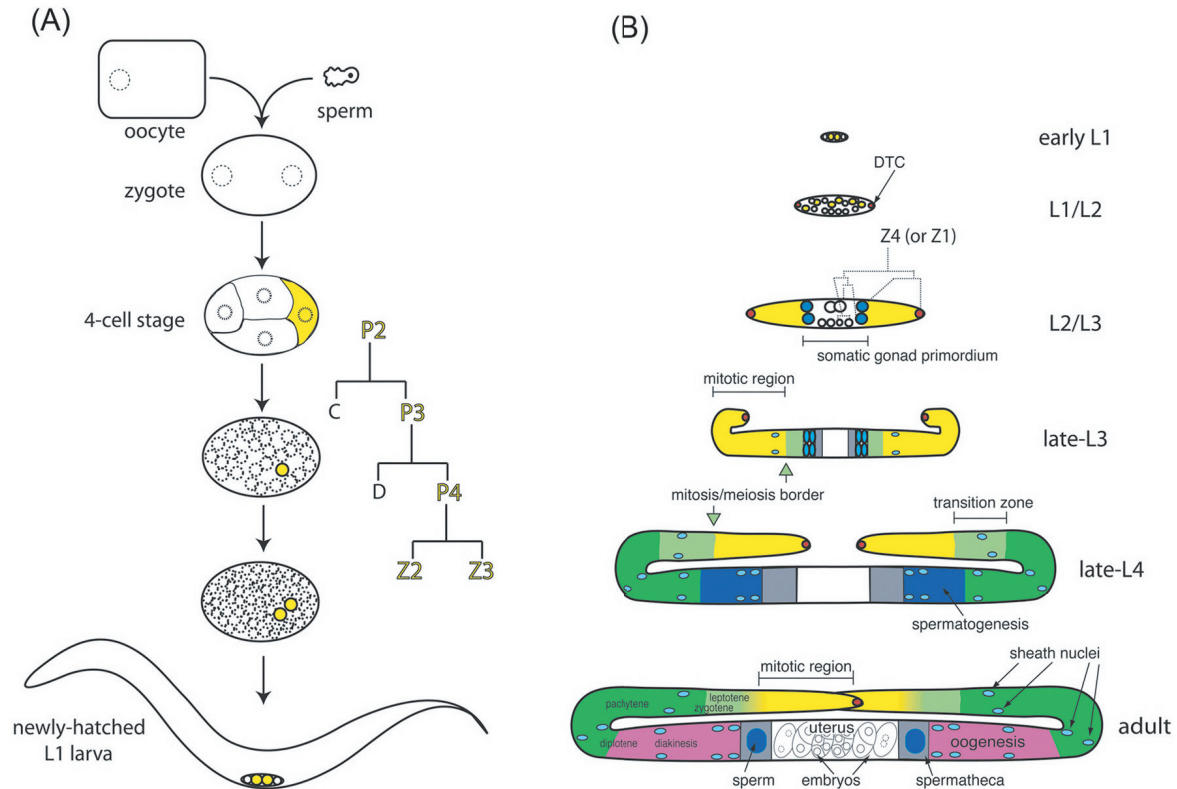


**Figure 2.1:** Formation of the germline: (A) Schematic of the germline lineage (yellow) segregation starting from single cell zygote. (B) Stages of development of the germline starting from L1 larval stage to young adults. *Adapted from* [43]

The development of the germline is crucially dependent on lineage segregation at the early embryo stage, where the single cell *C. elegans* zygote goes through an asymmetric division into A and P cells. The posterior cell P gives rise to eventually all germ cells and does not contribute to soma. At the stage of hatching, the gonad comprises of primordial germ cells (Z2 and Z3) connected to somatic gonad precursors (Z1 and Z4) and surrounded by basement membrane. These four cells stay mitotically quiescent until the mid-L1. Z1 and Z4 proliferate to 12 cells by the end of the L1 with two distal tip cells (DTCs) that are essential for growth of the germ line, and 10 proximal cells. The rapid extension of gonad arms is seen during early L3, provided by robust proliferation of the germline in response to proliferative signals from the distal tip cells [43].

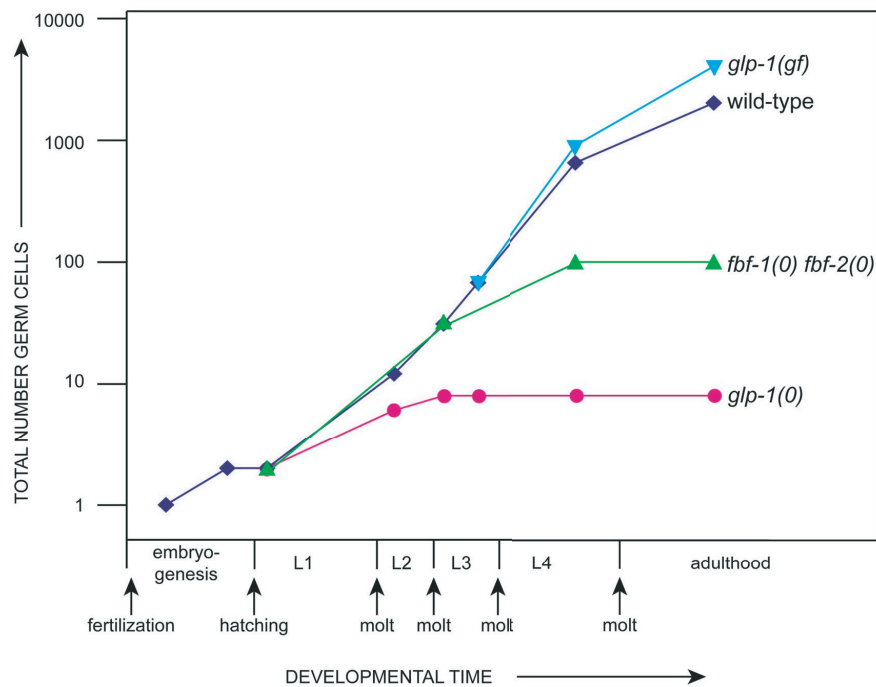


**Figure 2.2:** Germ cell numbers steadily increase in L4 and youngadults to roughly 2,000 germ cells [44]. The reduction of Notch receptor/GLP-1 inhibits germ cell proliferation and results in arrested growth up to only 4-8 germ cells [45]; in *glp-1* gain-of-function mutants, which have unregulated GLP-1/Notch receptors, they generate up to 4000 germ cells [46]. Adapted from *WormBook* [43].

Germ cell number goes through an approximately four-fold increase during the L4 and young adult stages (Fig.??). Germ cell proliferation is confined to the distal mitotic zone, a region that has been proposed to be a niche. Mitotic signals in the form of GLP-1 is known to suppress entry to meiosis. Hence modulation of GLP-1 affects the proliferation of germ cells and in turn the size and homeostasis of the germline. Gametogenesis spans the late L4 and adult stages: spermatogenesis occurs during the L4 stage and oogenesis during the adult stage. By the young adult stage the germline has achieved homeostasis of size that is maintained until aging (Fig.2.3). This homeostatic state closely configures to the physical idea of steady state and average macroscopic quantities e. g.size, length, number of cells remain unchanged over time.



## 2.1 Growth and motion of germ cells along the germline

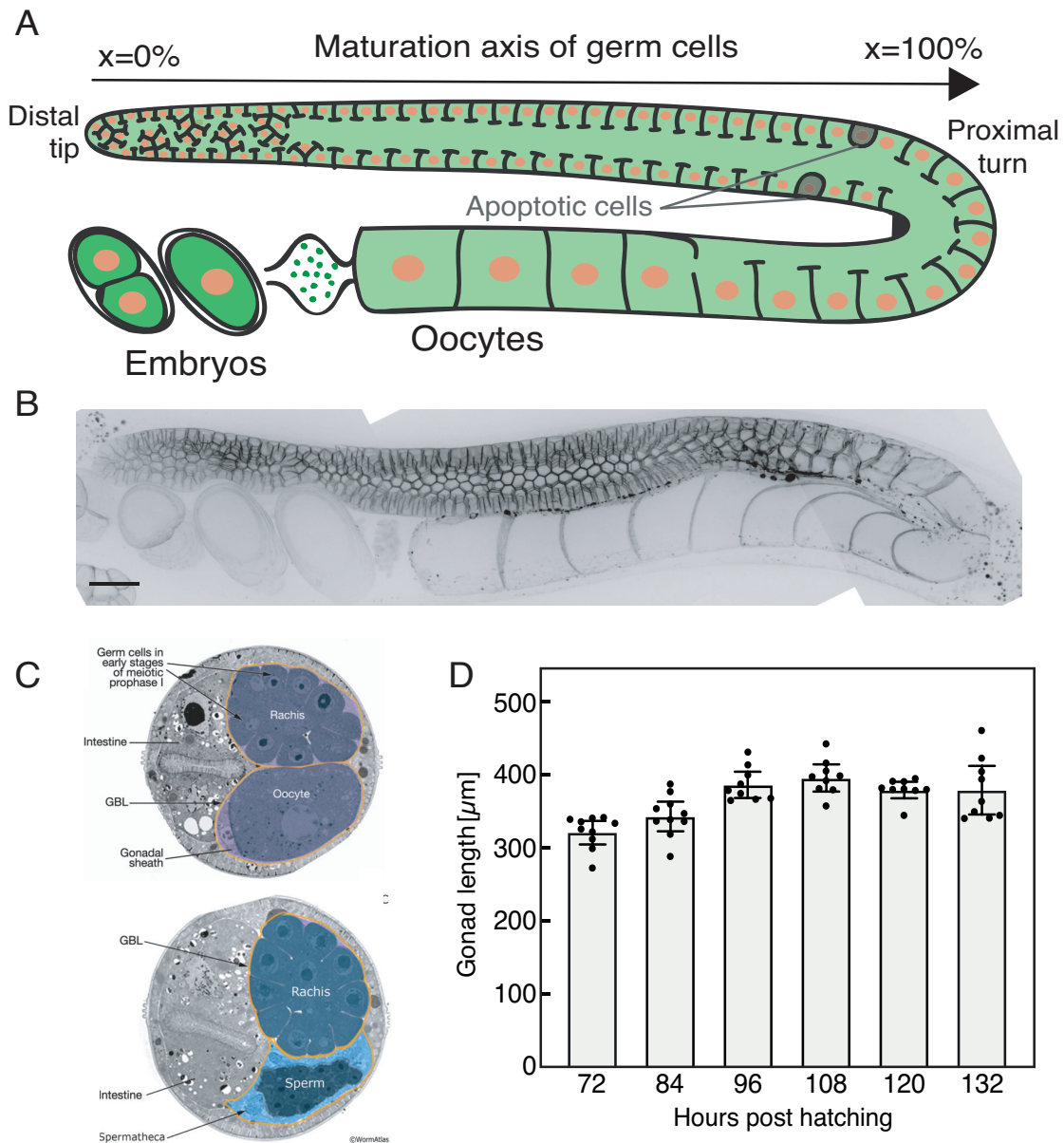


**Figure 2.3:** (A) Schematic of an adult germline representing a mid-sagittal section view. (B) Maximum intensity projection of an fluorescent micrograph of *C.elegans* adult germline; scale bar :20 $\mu\text{m}$  (C) Electron micrograph of the distal and proximal gonad representing different elements. GBL:gonadal basal lamina (Adapted from WormAtlas) (D) Measured length of the germline over time. Adapted from [47]

In this homeostatic state, the adult *C. elegans* germline constantly produces germ cells that goes through stages of growth and maturation as they move along the germline from the distal to proximal end all within one syncytial architecture where the cytoplasm is exchanged and streamed through the central cytoplasmic corridor called rachis [48]. The exchange of cytoplasmic between individual germ cells and the luminal rachis is mediated by rachis bridges, which are remnant of the cytokinetic ring formed a result of incomplete abscission [49]. Maintenance of such a dynamic steady

state at the adult stage poses interesting questions and consequences of physics, which span the later part of the thesis.

### 2.1.2 Motion and maturation of germ cells

The motion of germ cells is essential for the maturation and a quantitative understanding of this motion is crucial to develop a physical overview of the oogenesis as a whole. Direct approaches to access the velocities of germ cells pose the challenge of varying timescales. The germ cells move very slowly in the distal region of the germline and these velocities are statistically undetectable when compared to the twitching motion of the surrounding muscle, while they rapidly speed up as they approach the proximal turn. To extract steady and meaningful velocity profile of germ cells along the gonad we exploit the steady state of the germline and conservation of cell density. This can be expressed as,

$$\partial_t n + \nabla \cdot (n \vec{v}_c) = F(n) \quad (2.1)$$

Here  $n$  indicates the cell density,  $\vec{v}_c$  the cell velocity and  $F(n)$  indicates the local density changes due to birth and death events. For simplicity we choose  $F(n)$  to be a linear function of local cell density  $n$  [50–54] ,

$$F(n) = (k_d - k_a)n \quad (2.2)$$

where  $k_d$  and  $k_a$  are rates of cell division and cell apoptosis/extrusion. These quantities can be experimentally accessed by identifying densities of dividing cells (using mitotic spindles) along the gonad and cells going through characteristic apoptotic rounding [55] The spatial profile of the rate of change of effective cell density is shown in Fig.2.4. This is consistent with literature [43], where the mitotic zone ranges from 0%-30% length along the DP ( distal-proximal ) axis, while the apoptotic zone starts only beyond 60% gonad length.



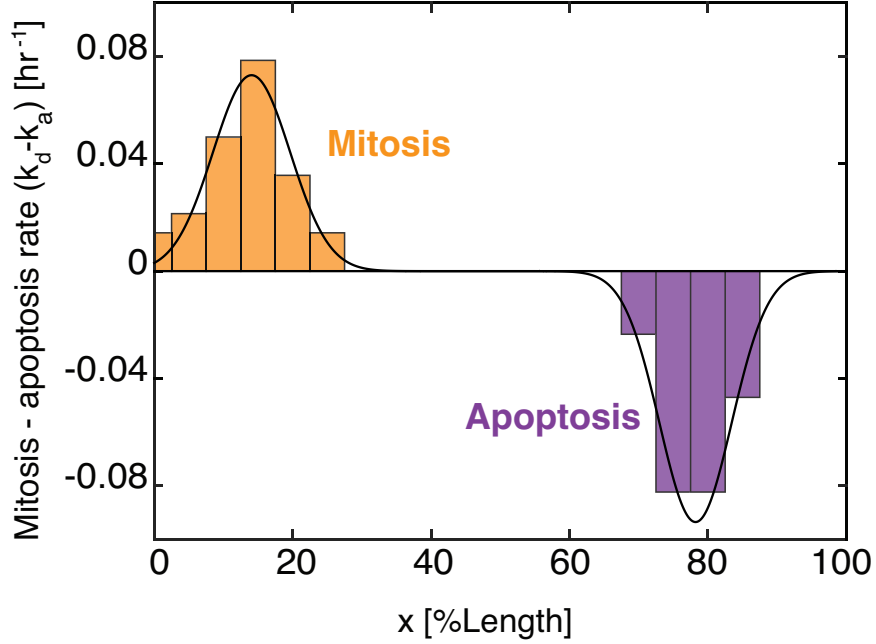


**Figure 2.4:** Spatial profile of effective rates of germ cell density change. Division rate ( $k_d$ ) is measured by counting mitotic spindles and apoptotic rate ( $k_a$ ) by counting apoptotic corpses.

In the steady state, the local cell densities do not evolve over time. Since the organ is primarily cylindrical we can assume axisymmetry around the DP axis, which is henceforth referred to as  $x$ -axis. The steady state cell density balance is simply given by,

$$\partial_x(nv_c) = (k_d - k_a)n \quad (2.3)$$

Here  $n$  is the linear density of cells along the DP/ $x$  axis and  $v_c$  is the  $x$ -axis velocity of germ cells. To infer the cell velocities we combine the measured birth and death rates (Fig.2.4) with measured linear density of cells (Fig.2.5). The solution is given by,

$$v_c(x) = v_c(0) + \frac{1}{n(x)} \int_0^x (k_d|_{x'} - k_a|_{x'})n(x')dx' \quad (2.4)$$

We choose  $v_c(0) = 0$  as boundary condition, which simply implies negligible motion at the distal tip.

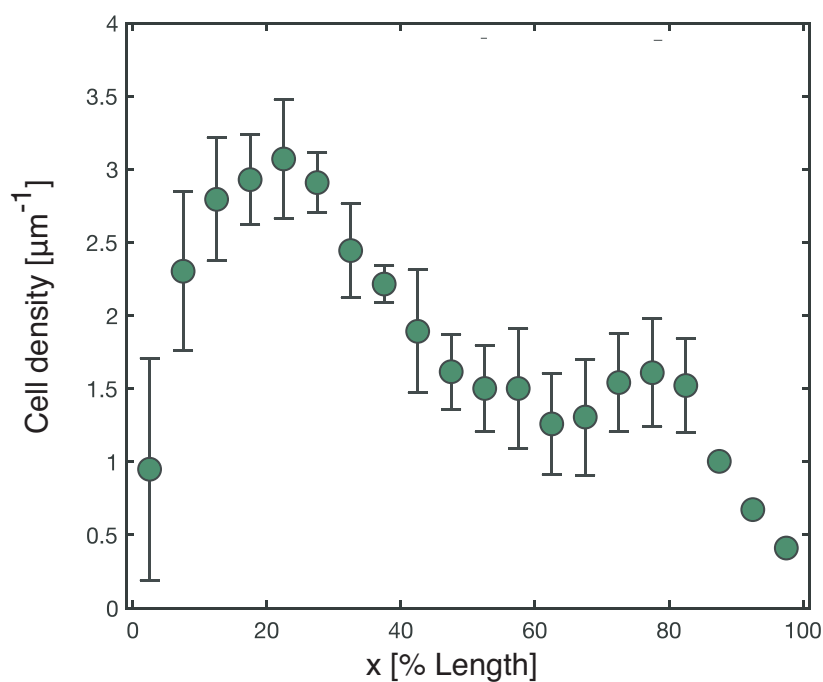


**Figure 2.5:** Profile of linear density of germ cells along the distal-proximal axis. All Error bars through out the thesis are 95% confidence interval of the mean.

The inferred cell velocity profile along the germline is depicted in Fig.2.6.

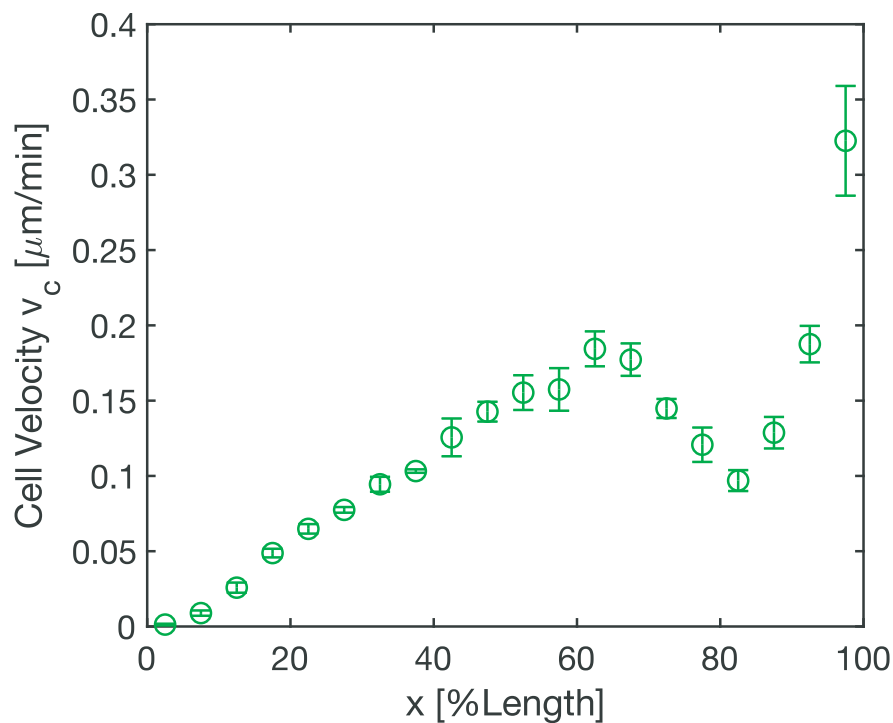


**Figure 2.6:** Inferred germ cell velocity field along the distal proximal axis.

We find that in the distal part of the germline the germ cell velocities steadily

increase upto  $\sim 60\%$  length of the germline, followed by a decrease and eventual increase. This non-monotonic behavior can be understood in simple terms by studying Eq.2.3, which only has two local terms  $k_d - k_a$  and linear density  $n(x)$ . The steady increase in the distal part of the germline is primarily due to cell division ( $k_d > k_a$ ) and incompressibility, where accumulation of new born cells drive cell flux, much like epiboly in Zebrafish [56] or cell motion in intestinal crypts [57]. The decrease can be associated with the concurrent apoptosis/extrusion ( $k_d < k_a$ ). The final increase of the germ cell velocity close to the proximal turn along with monotonic decrease of the linear density of cells  $n$  indicates a dilation or axial growth of germ cells, which can be seen in Fig.2.3B.

### 2.1.3 Growth of germ cells along the germline

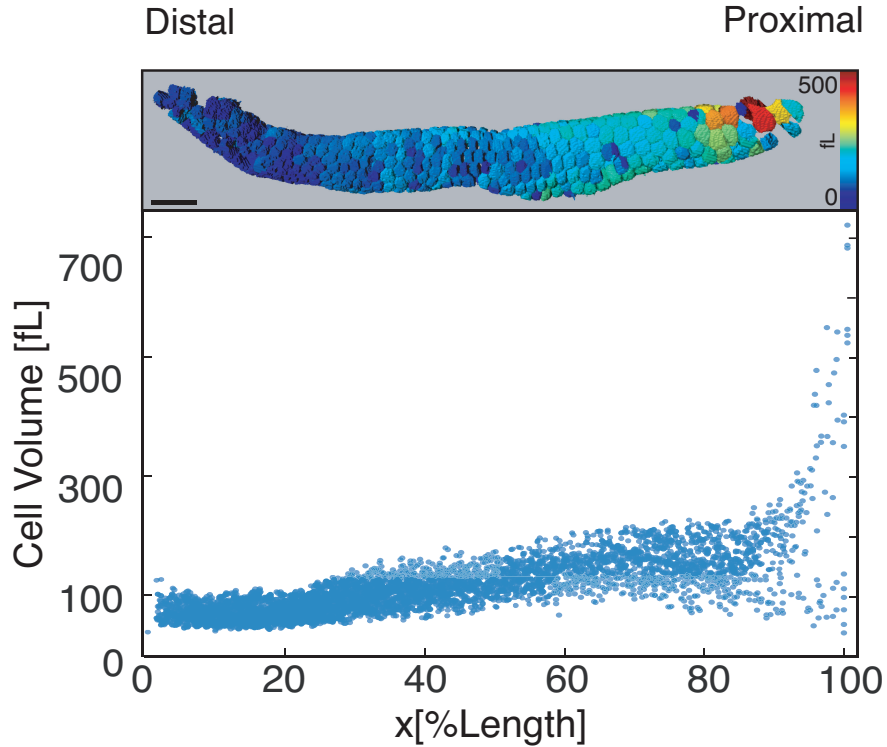


**Figure 2.7:** Spatial profile of germ cell volumes. Top: 3D rendering of segmented germcells color coded fro volume. Bottom: Cell volumes along the germline. Data from 5265 germ cells are shown taken from 18 gonad arms

To understand the growth of germ cells along the germline, we quantified the cell volumes using confocal microscopy and membrane based 3D segmentation (Fig.2.7). We find that the germ cell population is fairly homogeneous in size at the distal end and size of germ cells lie roughly  $\sim 60$  fL, the cells grow bigger in size along the germline DP axis and also the germ cell volumes become more dispersed. Close to the proximal turn the germ cells volumes are dispersed ranging from really large  $\sim 800$  fL to really small  $\sim 50$  fL cells. The growth of the germ cells can be captured in terms of

the average cell volumes along the germline, depicted in Fig.2.8 where spatial binning is employed to define statistical averages.

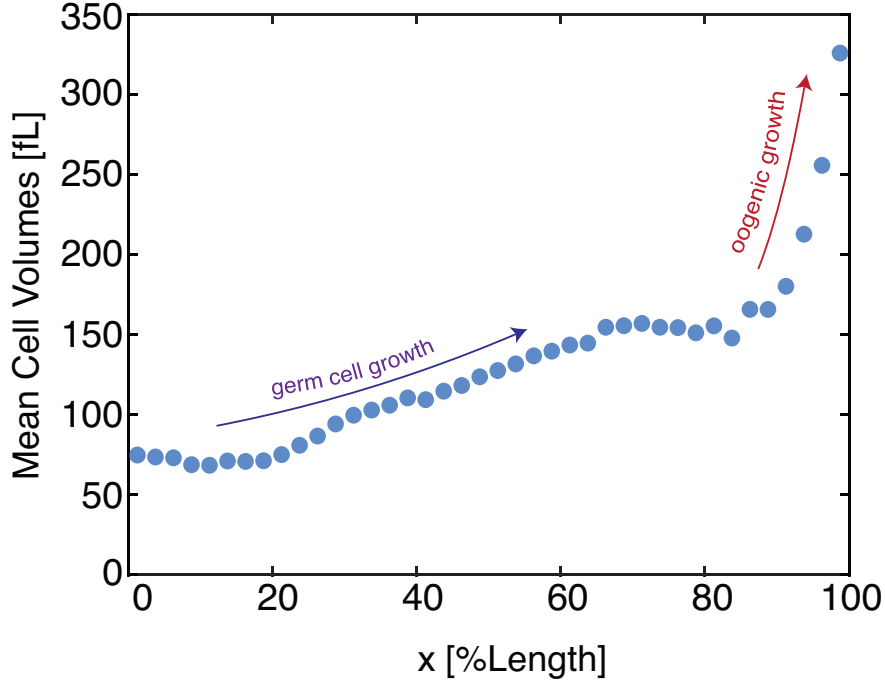


**Figure 2.8:** Average cell volumes along the distal-proximal axis. Two proposed growth phases are indicated with arrows.

The mean cell volume  $V_c$  shows a steady growth in the distal part of the germline, while it shows a steep increase in the more proximal part and indicates the onset of rapid growth prior to individualization of oocytes. Using the derived steady state quantities we next estimate an expected growth rate of the germ cells in the distal region. This is approximated as,

$$g_v = \left\langle \frac{dV_c}{dt} \right\rangle \simeq \frac{d\langle V_c \rangle}{dx} \left\langle \frac{dx}{dt} \right\rangle = g_v^{(x)} \langle v_c \rangle \quad (2.5)$$

where  $g_v^{(x)} = d\langle V_c \rangle/dx$  describes the spatial gradient of cell volumes along the gonad and  $v_c$  naturally indicates cell velocity. The above expression is exact when cell growth and cell motion are statistically independent, in this case however this is only a simplification. In the distal region we estimate  $g_v^{(x)}$  by fitting a linear curve to the average cell volumes along germline axis from 20% to 60% germline length and identifying its' slope. We find that the slope indicates  $g_v^{(x)} = 0.398(\pm 0.023)\mu m^2$  with 95% confidence intervals indicated in parentheses. Within this region, the inferred germ cell velocity  $v_c$  ranges from  $0.1\mu m/min$  to  $0.2\mu m/min$ . Hence the approximate growth rate of germ cell volumes in the distal region (20% to 60% length) range from  $g = 0.0398(\pm 0.0023)fL/min$  to  $g = 0.0796(\pm 0.0046)fL/min$ .

A similar analysis can also be performed along the Distal-Proximal axis of the germline and we can obtain local approximate growth rates of germ cells. Investi-

gating the potential relationship of mean growth rates with the mean cell volumes we find that in the distal region of the germline, the mean growth rate  $g$  is independent of local mean cell volume, while it shows a linear relationship with  $\langle V_c \rangle$  near proximal end, associated with the rapid growth of germ cells seen in Fig.2.8. This indicates a transition from a slow and constant growth regime, which we term as "germ cell growth" to a sharp and possibly exponential growth regime, which we term as "oogenic growth".

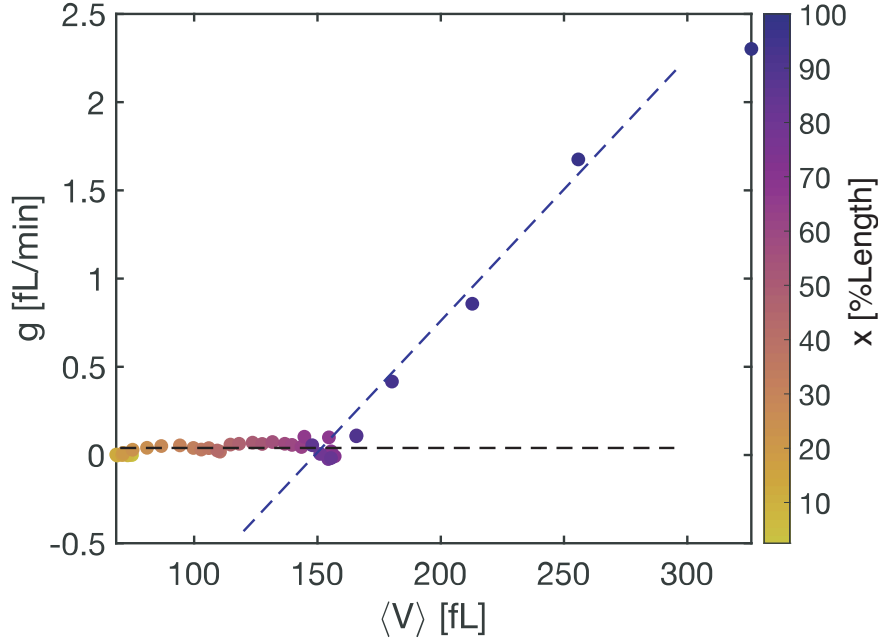


**Figure 2.9:** Local mean growth rates of cells is plotted against the local average cell volume, color coded for position along the germline. Black dashed line indicates the constant growth rate  $g = 0.039 \text{ fL/min}$ ; Blue dashed line is a linear fit to the most proximal data points.

### 2.1.4 Statistics of germ cell volumes along the germline

As evident from the growing spread of germ cell volumes in Fig.2.7, during maturation along the DP axis not only the underlying signature of germ cell growth changes but also the nature of variation. We observe a bimodal distribution of germ cell volumes emerging at the proximal end, starting from a unimodal structure at the distal regions. This might indicate a transition or instability somewhere along the DP axis. Taken together with the finding that average growth rate of germ cells behave distinctly between distal and proximal parts of germline, this lends credence to the idea of a transition between growth modes from distal to proximal. To identify such a transition, we shall discuss the statistical distinctions between volume distributions of the distal and proximal population of germ cells and theorize on possible underlying causes and consequences.

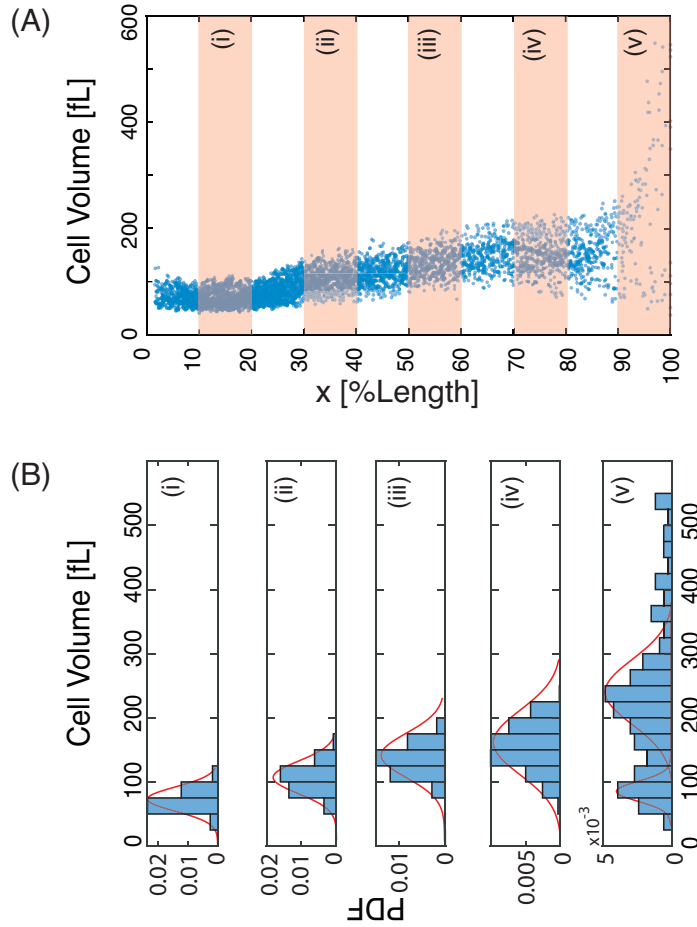


**Figure 2.10:** (A) Germ cell volumes transition from an unimodal to bimodal distribution along the DP axis. (B) Probability density is shown for 5 spatial bins indicated in (A). Red lines indicated Gaussian fits around each mode.

The growing variation can be captured in terms of the standard deviation of the volumes  $\sigma_V = \sqrt{\langle V^2 \rangle - \langle V \rangle^2}$ , which steadily increases (Fig. 2.11) along with the average volume of cells.

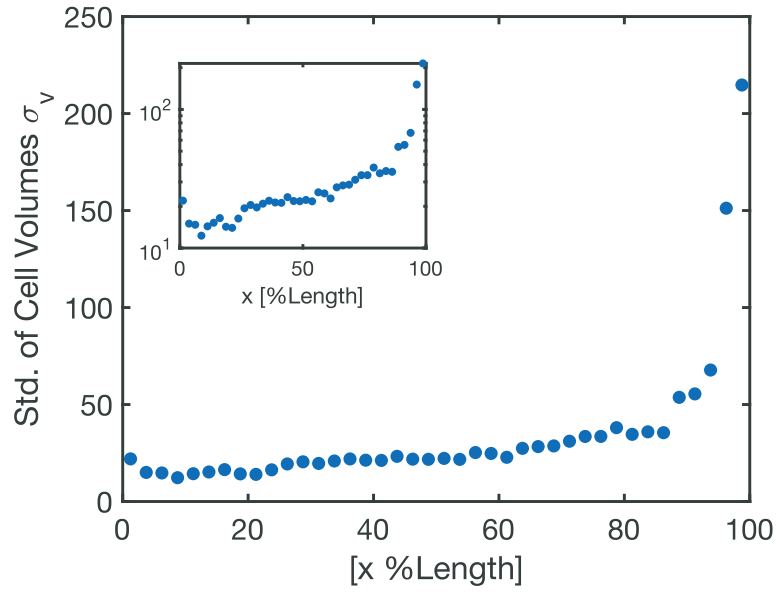


**Figure 2.11:** Local estimates of sample standard deviation of cell volumes plotted along position along the DP axis. Inset: Logarithmic scale

Next we investigate the relative variation of the cell volumes in term of the coefficient of variation (CV), defined as the ratio of standard deviation to the mean  $\mu_V$ , give by  $CV = \sigma_V/\mu_V$ .

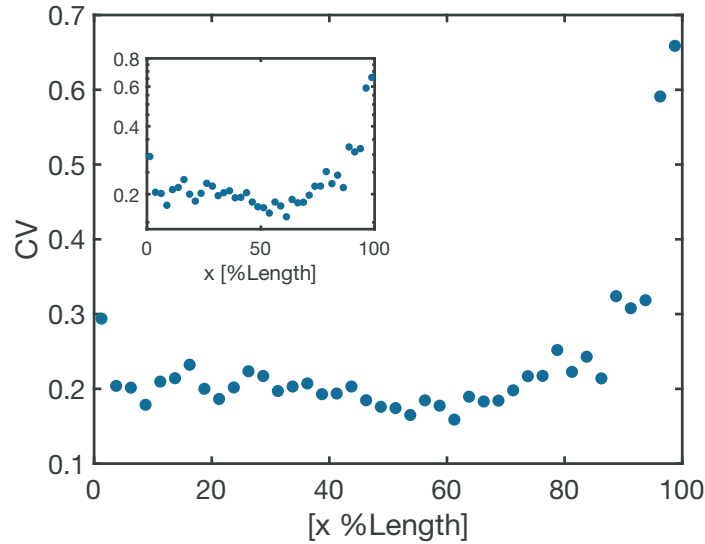


**Figure 2.12:** Coefficient of variation of germ cell volumes plotted along the DP axis. Inset: Logarithmic scale

Over the distal region of the gonad, the CV of cell volumes is fairly constant indicating a potential relationship between the  $\sigma_V$  and  $\mu_V$ . Such a relationship may allude to the possibility that the changes in mean and variation may originate from

same underlying processes. Similar relationships and implications have been studied extensively in the case of bacterial cell growth under different growth conditions [58].

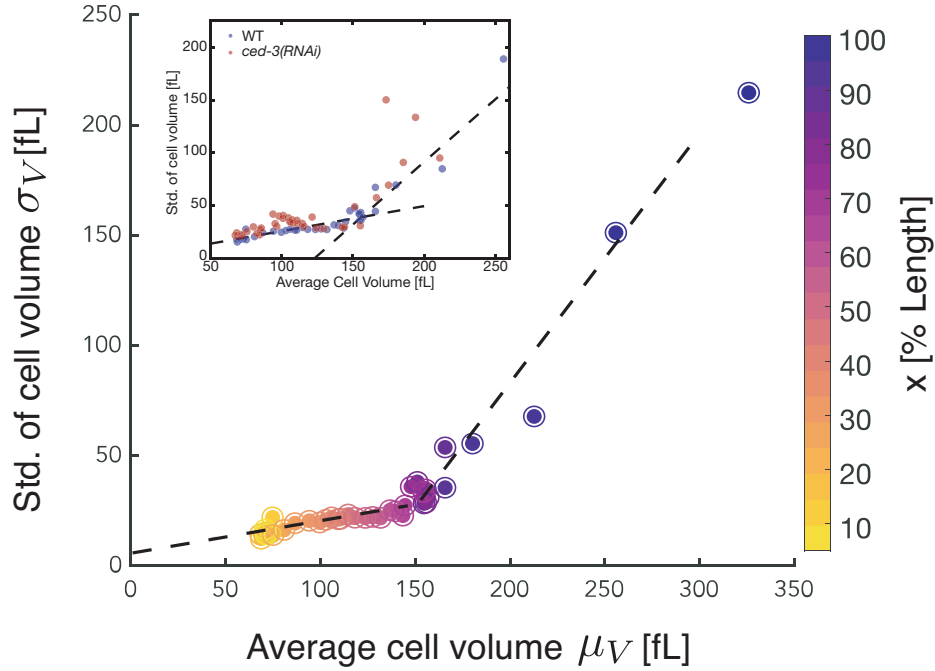


**Figure 2.13:** Relationship of standard deviation of volumes with mean cell volumes. Dashed lines indicates fitted linear relationship with the most distal and most proximal points (15,5 points in respective cases). Inset: overlay of two different genetic conditions show that the relationship between  $\mu_V, \sigma_V$  is robust.

The linear relationship of  $\sigma_V$  &  $\mu_V$  along with an equivalent CV, imply that the structure of the volume distributions in the distal region are similar. This can be seen in Fig.2.14 where the histograms of cell volumes of distal population rescaled by their respective mean is represented. To represent a regularized probability density function a kernel smoothing approach is employed with Kröneckers- $\delta$  function as the local kernel.



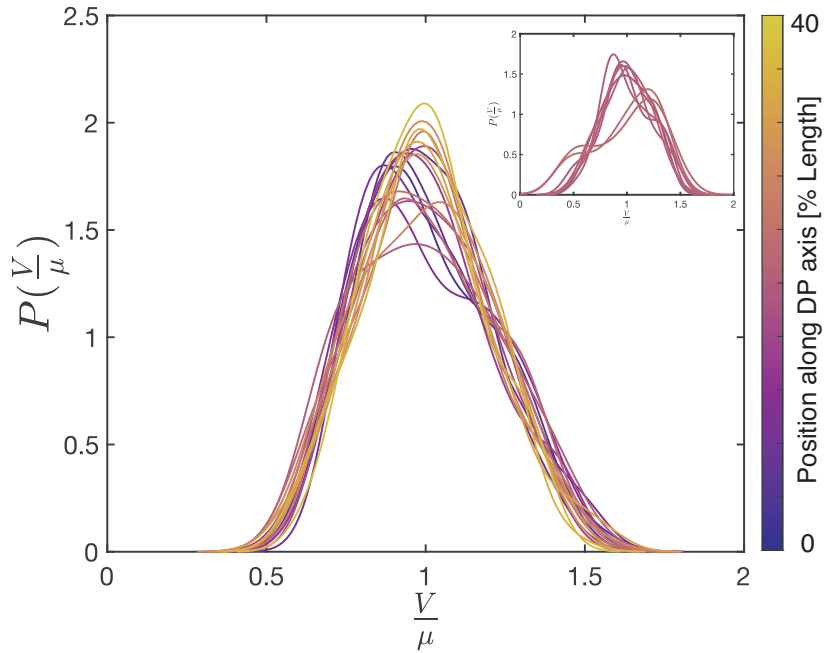


**Figure 2.14:** Probability density functions of normalized germ cells volumes (normalized by respective mean) from the distal part of the germline overlaid on top of each other. Color indicates spatial position along the germline in DP axis. Inset: PDF of normalized volumes of proximal germ cells

An equivalent representation is also found in Fig.2.14.

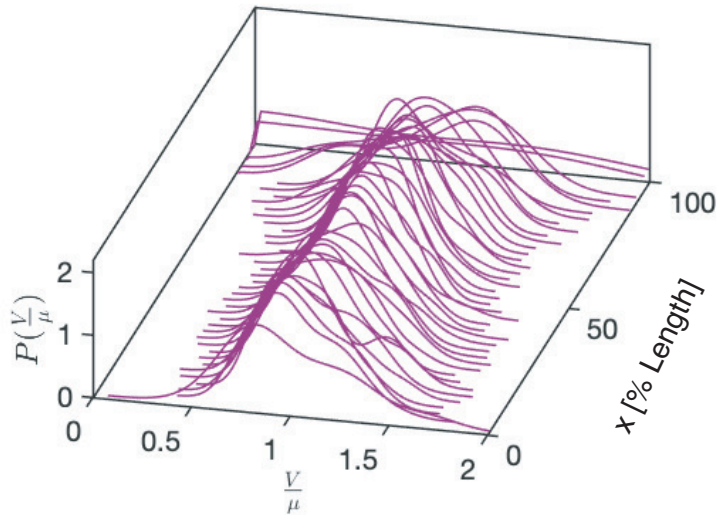


**Figure 2.15:** Probability density functions of normalized germ cells volumes (normalized by respective mean) from the distal part of the germline overlaid on top of each other. Color indicates spatial position along the germline in DP axis. Inset: PDF of normalized volumes of proximal germ cells

To further discuss the nature of the volume variations and how a relationship of  $\sigma_V$  and  $\mu_V$  might arise, we shall propose statistical models for the volume distributions. Naturally the cell volumes are limited to positive definite numbers, hence a regular Gaussian model would fail to capture the data. Moreover, the distributions are not symmetric and can be seen in the skewness of the cell volumes in Fig.2.16. We find that distal cell volumes are positively skewed indicating rare event of cells larger than mean, while proximal germ cell population shows negative skew indicating the opposite.

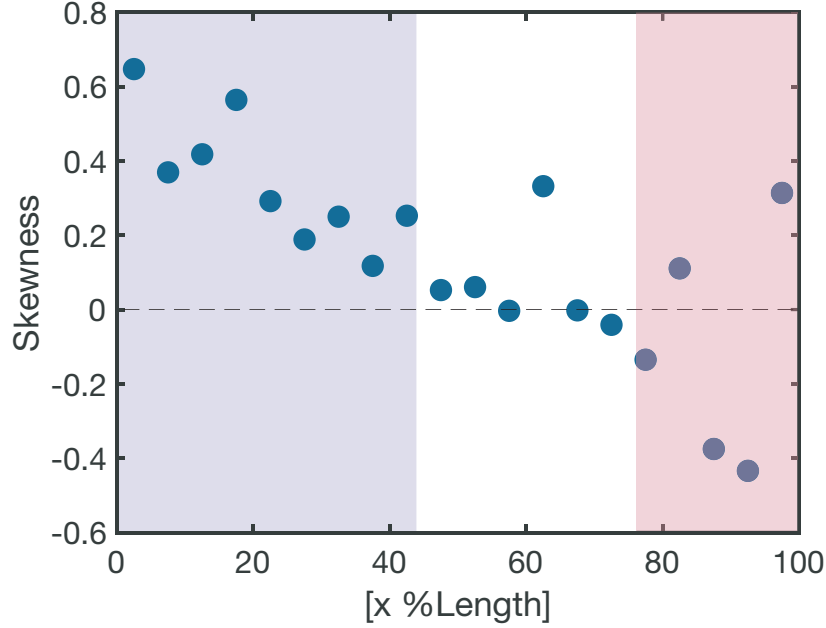


**Figure 2.16:** Skewness of the germ cell volumes along the DP axis. The distal zone shows positive skew, while the proximal zone shows negative skew.

A suitable statistical model that can capture both the positive definite aspect of the data as well as account for the shape asymmetry/skewness is the log-Normal distribution

$$P(x) = \frac{1}{x\sigma_x\sqrt{2\pi}} \exp\left(-\frac{(\ln x - \mu_x)^2}{2\sigma_x^2}\right) \quad (2.6)$$

Equivalently  $\ln x \sim \mathcal{N}(\mu_x, \sigma_x^2)$ . We find that the Log-Normal distribution represents the cumulative distribution function associated with the data well (Fig.2.17). Here we have rescaled the volumes of the cells by the maximum volume locally at the spatial bins. In the Fig.2.17 the solid line indicates the function,

$$\Phi(x) = \frac{1}{2} \operatorname{erfc}\left(-\frac{\ln x - \mu_x}{\sigma_x\sqrt{2}}\right)$$

where  $\operatorname{erfc}$  is the complementary error function. It is interesting to note that changes in  $\mu_x$  affect the mean and the sample variance of a log-normally distributed data however the coefficient of variation remains unchanged as it solely depends on  $\sigma_x$  and is given

by,

$$CV = \sqrt{\exp(\sigma_x^2) - 1}$$

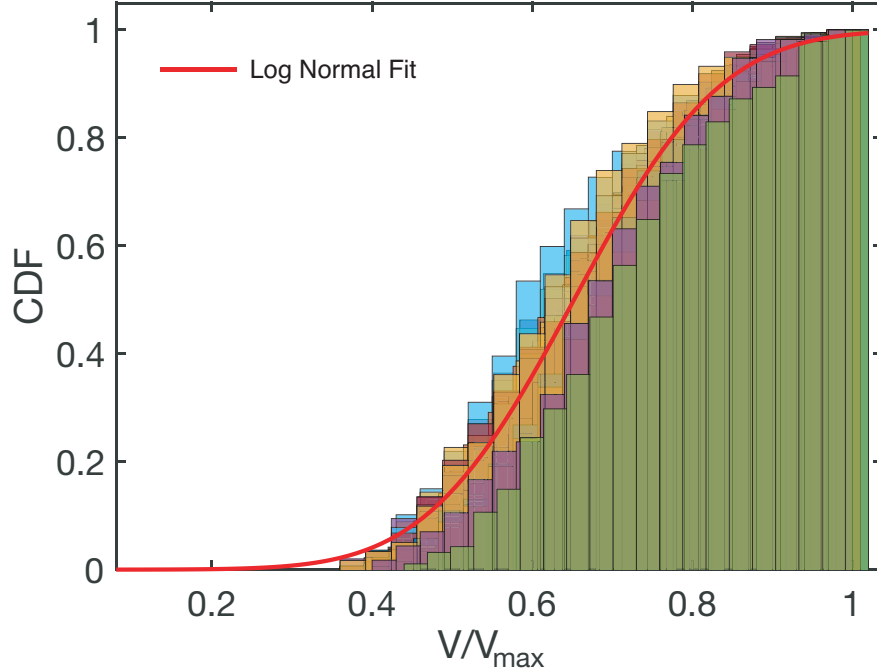


**Figure 2.17:** Cumulative distribution functions of normalized cell volumes ( 20 spatial bins of the 0%-40% germline length) overlaid. Solid red line indicates a single parameter fit of a log-normal distribution .

We propose the following explanation how a log-normal distribution might arise for cells that are growing. Consider a cell with volume  $V_t$  at time step  $t$  and it goes through geometric growth by a random variable  $r_t \in [0, \infty)$  and the volume at the next time step is give by,

$$V_{t+1} = r_t V_t \quad (2.7)$$

Hence the growth of cell volumes can be seen as a sequence of random multiplicative processes,

$$V_N = V_0 \prod_{i=1}^N r_i \quad (2.8)$$

$$\implies \ln \left( \frac{V_N}{V_0} \right) = \sum_{i=1}^N \ln r_i = \sum_{i=1}^N \chi_i \quad (2.9)$$

where  $r_i$  and hence  $\chi_i = \ln r_i \in (-\infty, \infty)$  may arise from different unknown distributions. Since  $r_i$  is a random variable,  $\chi_i$  also is a random variable and for increasingly many  $N$  we can invoke the central limit theorem. This is justified since any finite growth can be partitioned into infinitely many steps of infinitesimal change. The central limit theorem implies that the sum of infinitely many random variables

i. e.  $\chi_i = \ln r_i$  is a random variable with a Gaussian/Normal distribution. This would directly imply that the volume variable  $V_N$  is distributed log-normally. In the continuous limit this growth simply maps to a Geometric Brownian motion described by the stochastic differential equation,

$$dV_t = \mu V_t dt + \sigma V_t dW_t \quad (2.10)$$

where  $\mu$  is the deterministic relative growth rate and the second term describes a fluctuating growth where  $W_t$  is a Wiener process. This leads to a temporal growth of volume given by,

$$V_t = V_0 \exp \left( \left( \mu - \frac{\sigma^2}{2} \right) t + \sigma W_t \right) \quad (2.11)$$

This line of argumentation is interesting from a biological perspective as it would indicate that germ cell volumes grow geometrically. A contrasting scenario is found in microbial systems. While heavily debated, recent advances have suggested that in various forms of microbial life e. g. *E.coli*, *S.cerevesiae* etc. the growth is additive and challenges ideas of proportionate growth (for a review see [59]) , surface growth etc. that lie at the heart of allometry in biology [60].

### 2.1.5 Homogeneous and heterogeneous growth modes of germ cells

Taken together we find that the effective growth of germ cells transition from a slow constant phase in the distal germline to a more geometric one in the proximal. Along with the effective mean growth of cells, the nature of variation of volumes along the gonad also transitions, maintaining a low relative dispersion ( $CV \sim 0.2$ ) in the distal part while high heterogeneity and bimodality arises in the proximal part. This separates the germ cell growth into a homogeneous phase in the distal part and heterogeneous one in the proximal part. We also find that, due to a linearity of the mean and std. deviation of the cell volumes in the distal part, the distribution of cell volumes normalized by their respective means collapse on top of each-other. This underlying feature of the cell size distribution disappears in the proximal part, as the distributions become more negatively skewed and heterogeneous. To further investigate the heterogeneity of volumes we borrow well established inequality quantifiers from economic theory, namely the Gini index and the Hoover index [61]. The Gini index  $G$  and Hoover index for a population of  $n$  values  $x_i$  where  $i = 1, \dots, n$  with sample mean  $\mu_x = \sum_{i=1}^n x_i/n$  are given by,

$$G = \frac{1}{2n^2\mu_x} \sum_{i=1}^n \sum_{j=1}^n |x_i - x_j| \quad , \quad H = \frac{1}{2n\mu_x} \sum_{i=1}^n |x_i - \mu_x| \quad (2.12)$$

We find that both inequality indices show a steady growth beyond  $\sim 60\%$  germline length [Fig.2.18], marking the onset of heterogeneous growth.

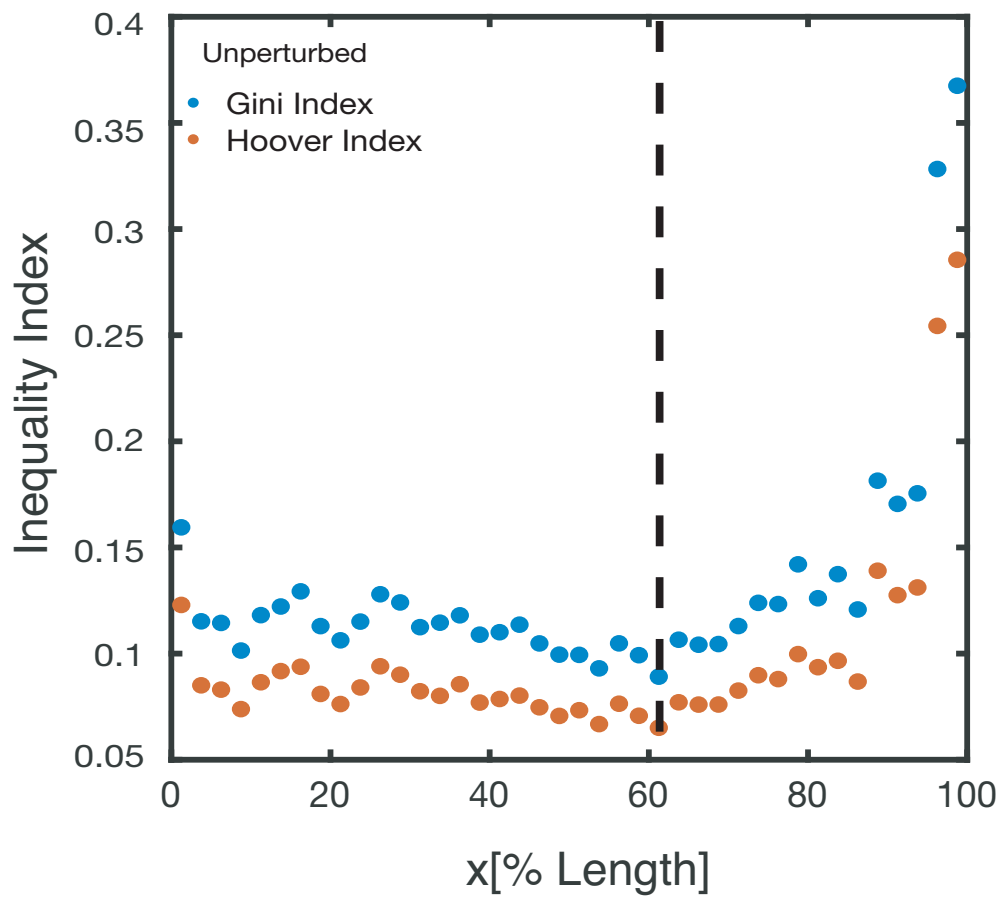


**Figure 2.18:** Inequality indices show steady growth beyond  $\sim 65\%$  germline length

## 2.2 Flow fields within the germline

In the previous section we have established the nature of two distinct growth modes of germ cells that are spatially segregated along the DP axis and this transition lies around  $\sim 65\%$  germline length. These findings pose the following question,

**Q:** What is the underlying basis of these two growth modes i.e. what sets the distinct rate of average growth and the origin of volume heterogeneity?

In this section borrowing principles of fluid dynamics, we investigate the underlying basis of these indicated growth modes and postulate the associated transition. In the spirit of the previous section, we again rely on fundamental conservation laws and physically motivated approximations to identify and extract variables necessary to discuss the origin of volume growth of germ cells. Before considering the intricacies of the underlying growth dynamics, we clarify certain geometric constraints under which the germ cells must grow and interestingly that limit the consideration of possibilities.

Like many other species, nematode germ cells grow within a syncytial structure and are connected to a central luminal corridor called rachis. This allows for exchange of cytoplasm from germ cell to rachis via rachis bridges and indirectly to other germ cells of the syncytia. As a result the germ cells can either grow/shrink by exchanging volume with the outside environment surrounding the germline or via cytoplasmic exchange with the rachis [Fig.2.19].

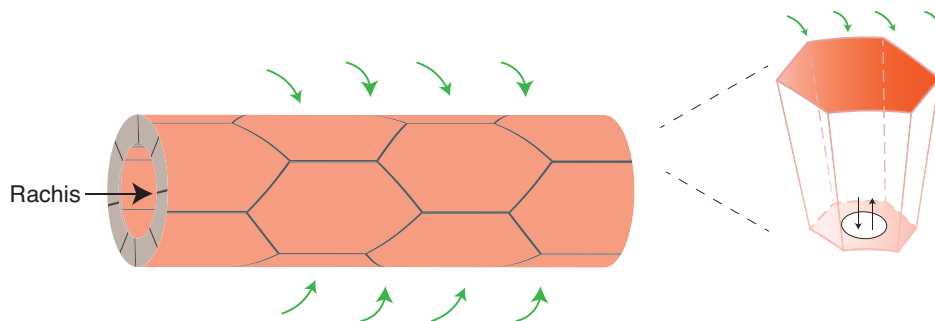


**Figure 2.19:** A schematic of the germline is shown emphasizing how exchange of volume could either be from outside or with the rachis.

Within rachis, the shared cytoplasm is distributed via long range flows from the distal to proximal end. These flows are known to drive the final steps of growth of the oocyte. As the germ cells are connected to the germline via holes and exchange cytoplasm, it is reasonable to assume that these flows might mediate cytoplasmic exchange with germ cells hence affect growth of cells, however very little is understood about germline hydrodynamics. In the following section we shall investigate the relationship of the germ cells with the flows within the rachis with the goal to understand the growth dynamics of the germ cells and the germline tissue as a whole.

### 2.2.1 Volume flux through the rachis

To discuss the cytoplasmic streaming in the DP axis, we perform fluorescence microscopy on the mid-sagittal plane of the rachis and employ a Particle Image Velocimetry [62–64] originally developed by PIVLab [65], to map the velocity field of the cytoplasmic flow through the rachis. The general algorithm of velocity determination of PIVLab is based on optimizing cross-correlations. A brief overview of the idea follows. Let  $I_n(x, y)$  denote the intensity value of the pixel at point  $(x, y)$  in the  $n^{\text{th}}$  frame of a movie. After defining a coarsegraining template of  $d \times d$  pixels, we can optimize the following cross-correlation,

$$X_n(x, y, \Delta x, \Delta y) = \frac{\sum_{x'=x-d}^{x+d} \sum_{y'=y-d}^{y+d} [I_n(x', y') - \bar{I}_n(x, y)] [I_n(x' + \Delta x, y' + \Delta y) - \bar{I}_n(x + \Delta x, y + \Delta y)]}{\sqrt{\sigma_n^2(x, y) \sigma_{n+1}^2(x + \Delta x, y + \Delta y)}}$$

where

$$\bar{I}_n(x, y) = \left(\frac{1}{2d+1}\right)^2 \sum_{x'=x-d}^{x+d} \sum_{y'=y-d}^{y+d} I_n(x', y') \quad (2.13)$$

$$\sigma_n^2(x, y) = \left(\frac{1}{2d+1}\right)^2 \sum_{x'=x-d}^{x+d} \sum_{y'=y-d}^{y+d} [I_n(x', y')^2 - \bar{I}_n(x, y)^2] \quad (2.14)$$

The solution to this optimization problem yields the  $(\Delta x^0, \Delta y^0)$  for a given set of  $(x, y)$  at the  $n^{\text{th}}$  time frame that maximizes the cross-correlation. From this estimate one can define the instantaneous velocities related to the coarsegraining box as,

$$v_x = \frac{s}{\tau} \Delta x^0 \quad (2.15)$$

$$v_y = \frac{s}{\tau} \Delta y^0 \quad (2.16)$$

This provides two dimensional velocity fields within the germline [Fig.2.20 A]. The total three dimensional volume flux is defined as,

$$Q = \int \vec{v} \cdot \hat{n} dA \quad (2.17)$$

where  $\vec{v}$  is the velocity vector and  $\hat{n}$  is the unit normal vector of the area element  $dA$ . We assume axisymmetry to estimate this quantity from two-dimensional fields. We further find that the velocity along the DP axis peaks at the center of the rachis and decays similar to a parabola towards the boundary of the rachis tube [Fig.2.20 B]. This is similar to a flow profile of a viscous fluid in a pipe [66]. The paraboloid flow profile in a tube is simply an outcome of no-slip boundary condition and azimuthal symmetry.

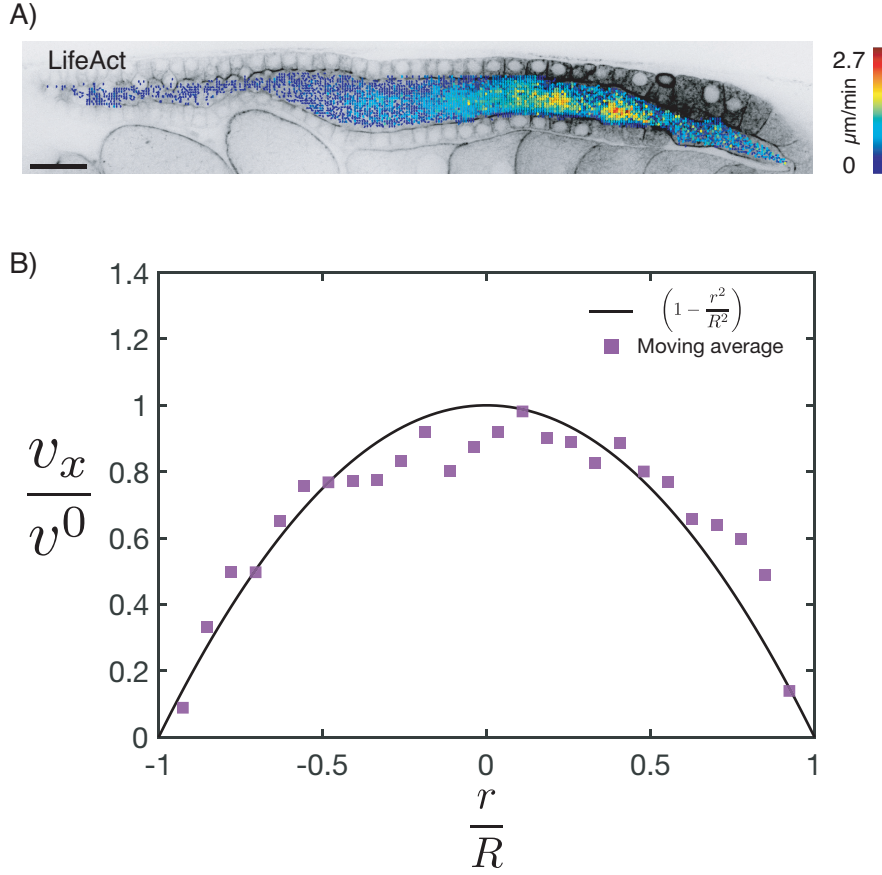


**Figure 2.20:** A) An overlay of the germline image with an inferred velocity field from PIV is presented. Color codes indicate speed. B) The normalized DP axis velocity of the flowing cytoplasm decays symmetrically from the center. Solid black line is a parabolic profile for comparison; exact form is indicated in legend.

We use the centerline of the rachis to identify the orthogonal cross-section and from it the related  $\hat{n}$ . The dot product of the local velocity field  $\vec{v}$  with  $\hat{n}$  yields the DP-axis velocity  $v_x$ , which is the velocity component parallel to the centerline. At each position of the centerline we extract how  $v_x$  as a function of distance  $r$  from the center to towards the edge [Fig. 2.20 B]. To this radial profile of DP-axis velocity we fit the following parabolic profile,

$$v_x(r) = v^0 \left( 1 - \frac{r^2}{R^2} \right) \quad (2.18)$$

where  $v^0$  &  $R$  are fit parameters that respectively indicate the peak velocity at the center and radius of the tube. The volume flux then is given by,

$$Q_r = \int d\phi \int_0^R v_x(r) r dr \quad (2.19)$$



which for the parabolic form reduces to,

$$Q_r = \pi R^2 \frac{v^0}{2} = \pi R^2 \bar{v} \quad (2.20)$$

Hence estimation of  $v^0$  &  $R$  completely determines the volume flux. It is noteworthy that the average velocity is simply given by  $\bar{v} = v^0/2$ . This is due to the symmetry of the flow profile around the center of the tube. We use this relationship between the average velocity and maximum velocity to identify deviations from pipe flow and define a consistent dataset. For a discussion on viscous flows through a pipe see Appendix B.

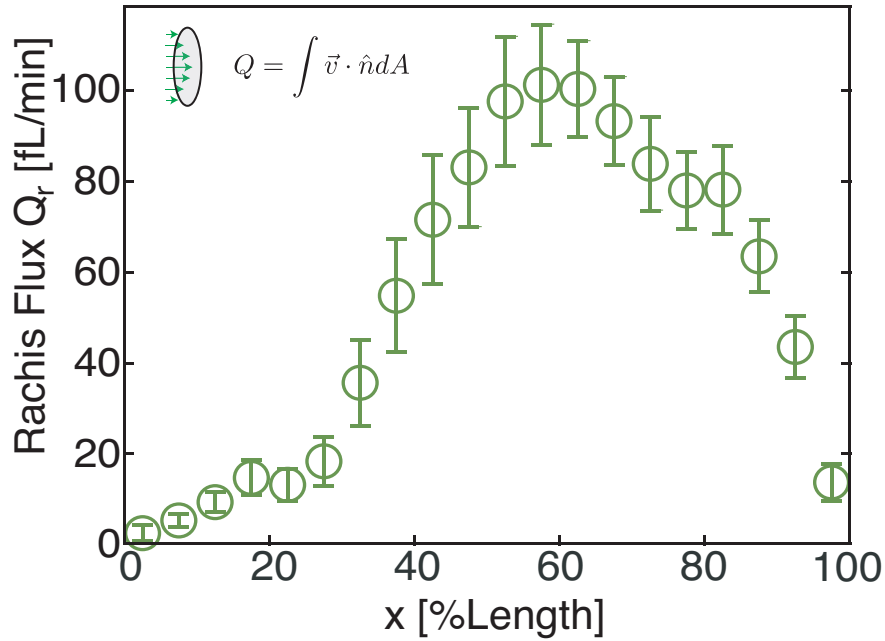


**Figure 2.21:** Volumetric flux through rachis is represented along the DP axis. The rachis flux peaks at about  $\sim 60\%$  germline length. Spatial gradient of the rachis flux indicates exchange with the surrounding germ cells.

We find that the volume flux through rachis/discharge rate  $Q_r$  shows monotonic growth until  $60\%$  of the germline length, beyond which it steadily decreases. To understand the implications of this spatial profile of the volume flux, we appeal to the fundamental principle of volume conservation, which is ensured in an incompressible fluid [66–69]. Given that cytoplasm is incompressible we can further deduce that the spatial gradient of this volume must identify the local information of sources and sinks which account for the changes of the volume flux. Let us formulate this with the following conservation law,

$$\partial_t A_r + \partial_x Q_r = J \quad (2.21)$$

where  $A_r$  represents the cross-sectional area of the rachis and  $J$  represents the current

of material in the direction of germ cell to rachis i.e. when the exchange of cytoplasm driven by this current is in the direction of germ cell to rachis  $J > 0$ . At steady state the current  $J$  is simply given by the spatial gradient of  $Q_r$ . As noted before,  $Q_r$  steadily increases along the DP axis in the distal region upto  $\sim 60\%$  germline length and decays thereafter. This indicates that  $J > 0$  in the distal region and switches sign in the proximal germline. We therefore calculate  $J$  from the spatial gradient of  $Q_r$  using a central difference method.

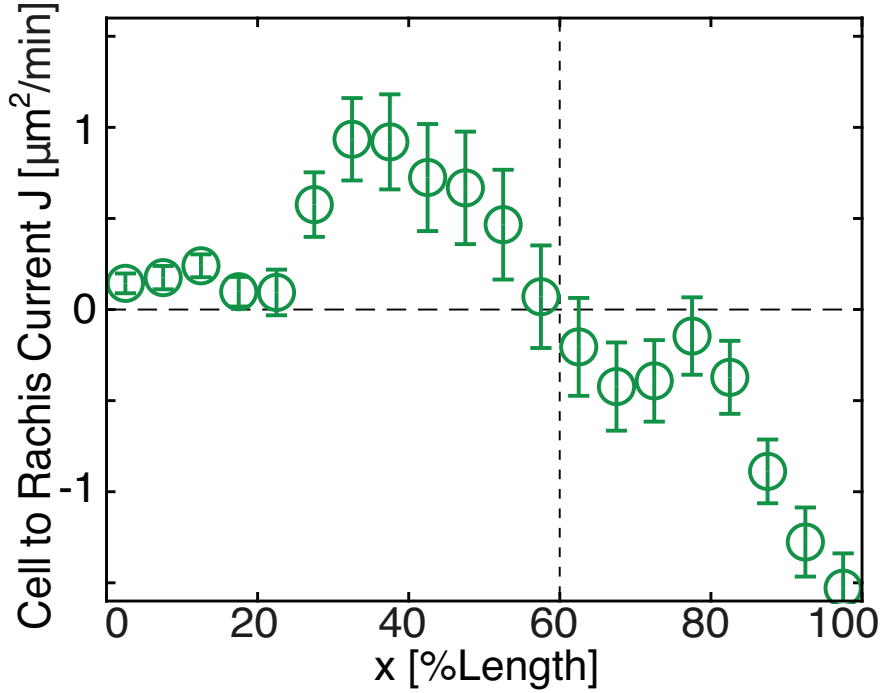


**Figure 2.22:** Spatial profile of germ cell to rachis current  $J$  is shown. In the distal region  $J > 0$  and beyond  $\sim 60\%$  germline length  $J < 0$

The nonzero current profile implies exchange with the surrounding germ cells. In the distal region  $J > 0$ , which implies that germ cells donate cytoplasm to the rachis and drive the cytoplasmic streaming, while in the proximal gonad  $J < 0$  indicating that germ cells take up material from the rachis to grow in volume. It is interesting to note that in the distal region despite losing material to the rachis distal germ cells grow from  $\sim 50fL$  to  $\sim 150fL$  in size. As a mere consequence of volume conservation, this extra material for growth in the distal region then must arise from an external source surrounding the germline and the gonadal basal lamina. To calculate this external source we must account for flux balance of the entire germline tissue including the transport flux due to cell motion.

## 2.2.2 Cell volume flux

In the same spirit we define the flux balance of cellular part of the germline as,

$$\partial_t A_c + \partial_x Q_c = S - J \quad (2.22)$$

where  $Q_c = v_c A_c$  is the total cellular material flux, defined as the product of average cell velocity and the cellular fraction of the germline cross-sectional area.  $S$  is the source current which quantifies material uptake from the surrounding.

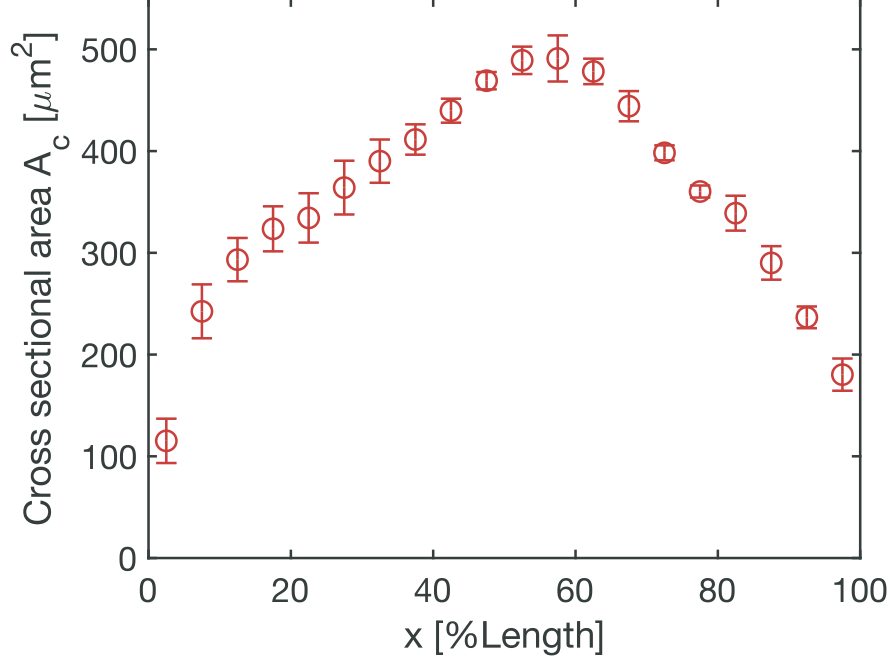


**Figure 2.23:** Spatial profile of cellular part of the germline cross-section  $A_c$

Combining with previously estimated cell velocities (Fig.2.6) with the estimate of  $A_c$  we identify the spatial profile of cell material flux  $Q_c$ . Both the conservation laws are,

$$\partial_t A_c + \partial_x Q_c = S - J \quad (2.23)$$

$$\partial_t A_r + \partial_x Q_r = J \quad (2.24)$$

which taken together provides the total conservation of volume flux,

$$\partial_t (A_c + A_r) + \partial_x (Q_c + Q_r) = S \quad (2.25)$$

$$\implies \partial_t A_{tot} + \partial_x Q_{tot} = S \quad (2.26)$$

where  $A_{tot} = A_c + A_r$  and  $Q_{tot} = Q_c + Q_r$ .

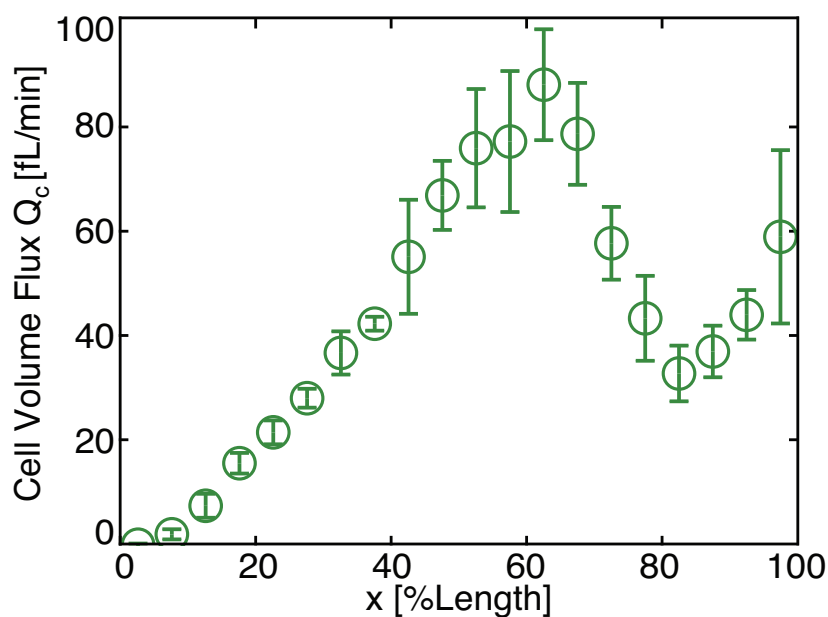


**Figure 2.24:** Spatial profile of cell volume flux  $Q_c$ . Steady growth upto  $\sim 60\%$  germline is observed beyond which non-monotonic behavior sets in.

### 2.2.3 External source current

Invoking the steady-state argument we identify the source current  $S$  as the spatial gradient of total volume flux  $Q_{tot} = Q_c + Q_r$ . A central difference method is used to evaluate the numerical gradient.

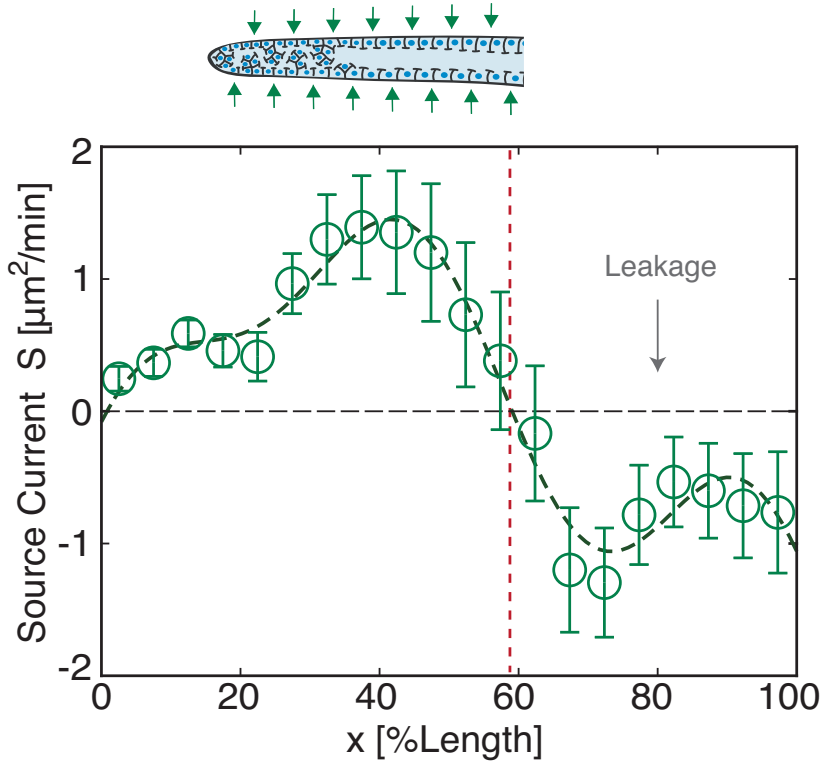


**Figure 2.25:** Source Current along the DP axis. Black dashed line shows a smooth representation of  $S$ ; red dashed line marks the region where  $S$  changes sign from positive to negative.

We find that, consistent with our argumentation source current is positive in distal region accounting for growth of distal germ cells despite losing material to the rachis and driving cytoplasmic streaming. Interestingly, the effective source current is negative in the proximal region, indicating loss/leakage from the germline tissue. We hypothesize that this leakage in the proximal gonad, is due to extrusion of apoptotic cells. It is noteworthy that this spatial information is unknown in literature, likely due to the inability to visualize and quantify take up of cytosolic matter. This physics motivated analysis provides a novel way of accessing this spatial information and hence the first quantitative insights on how germ cells grow by taking up material from surrounding.

Moreover, this also implies that the distal germline primarily transports material from outside to rachis, driving long range cytoplasmic flows which leads to growth of proximal cells as well as future oocytes. It is noteworthy that in the distal region  $S > J$  and one can define the ratio as the pumping/filtration efficiency,  $\eta_\pi = J/S$ . We find that  $\eta_\pi = 0.46(\pm 0.08)$ .

## 2.3 Conclusion

In this chapter we set out to investigate the underlying basis of germ cell growth as well as how within this syncytial architecture some germ cells grow to become oocytes

and some shrink and are apoptosed.

We found that in the distal part of the gonad, the germ cell population starts out homogeneous and grows with a constant rate while maintaining low relative variation. A strict relationship between sample mean and sample standard deviation of volumes indicates regulated structure of the variation of cell volumes. This regulation of cell size variation disappears in the proximal part, as the germ cell population becomes increasingly heterogeneous and eventually bimodal. A transition is indicated by the crossover of sample mean and sample standard deviation of volumes, from one linear relationship to another with steeper slope. This implies incommensurate increase of variation with respect to overall growth. Concurrently the mean growth rate sharply increases in a volume dependent manner. We proposed and utilized two probabilistic models to understand how variation of cell sizes may arise in this context. Taken together, we found that germ cells populations show distinct modes of growth in distal and proximal germline; the distal population grows slow and "homogeneously" while the proximal one is "heterogeneous" and rapid, possibly marking the onset of eventual oogenic growth.

We next set out to identify the hydrodynamic basis of germ cell growth to investigate and explain the transition from one growth mode to the other in the distal-proximal axis. Using concepts of fluid dynamics of viscous incompressible fluids and conservation laws, we ascertain volume fluxes due to cytoplasmic streaming and cell movements. A nonzero spatial gradient of the cytoplasmic flux in the rachis informed us about the spatial profile of volume exchange between germ cells and rachis. This current  $J$  shows a clear transition around  $\sim 60\%$  germline length, where it changes sign from positive to negative. This marks the transition from a phase where germ cells lose cytoplasm to rachis to a phase where they take up volume from the cytoplasmic stream down the distal proximal line. The puzzling growth of germ cells in the distal part despite losing material to rachis, led us to find the spatial profile external source current that must exist to account for distal germ cell growth. Here as well, we find a transition of source current at about  $60\%$  germline length. Both lateral fluxes that drive the flow of cytoplasmic stream and the cell volume flux, invert in the same region, revealing a transition of underlying tissue hydraulics.

The spatial proximity of the transition in tissue hydraulics and the statistical instability of cell volumes begs the question whether the hydraulic transition not only underlies the change in growth rate but also drives the growing heterogeneity. The proximal germ cells are inflated by the cytoplasmic streaming and alludes to the possibility that such inflation mechanisms are inherently unstable. In simile, it is impossible to inflate two connected soap bubbles together via a channel, as due to curvature driven forces small variation of sizes amplify making the configuration increasingly heterogeneous and eventually one bubble engulfs the other. Similar instability also occurs for two connected balloons [70, 71]. To address whether the transition in tissue hydraulics could trigger such an instability and henceforth underlie the essential decision of life and death in germ cells, a theoretical framework is necessary that addresses questions of structural stability of the germline. Towards this end, we derive a physical framework in the next chapter.

# Chapter 3

## Biophysical theories of the germline dynamics

In the previous chapter, we have uncovered the intricate interplay of long range flows of cytoplasm as well as cells with the emergent and quiet essential phenomena of growth and shrinkage of germ cells within the *C. elegans* oogenic germline. Unlike other cells that constitute tissues, the germ cells are not individual as they are connected to each other via the luminal corridor "rachis", which itself mediates long range cytoplasmic flows. Hence these cells lack fundamental mechanisms of volume control or volume elasticity and rapid changes and redistribution of volume is permitted by geometry and the underlying mechanics. While various aspects of tissue mechanics and hydrodynamics is extensively studied, this unique system and phenomena pose novel and fascinating questions about dynamics of tissue that pump and grow, hence presenting an opportunity of new ideas and concepts.

In this chapter we will derive a framework to discuss the tissue hydraulics of germline, with a particular focus on understanding effects of source and sink of material from outside in the development of long range flow fields of cytoplasm as well as cells. Using this framework, we will investigate how steady pressure gradients may develop within an organ "at rest", and how these pressure gradients drive volume exchanges locally. Furthermore, we will explore how such volume exchanges and fluxes influence the stability of a cellular doublet as well as a cellular collective.

### 3.1 Hydrodynamics of the germline

The germline is a syncytial tube that consists of a monolayer of cells. Within this monolayer the cells divide and extrude, which introduces local changes in density as well force dipoles, which leads to a coarse-grained effect of local stresses and gradient of such stresses can drive rearrangement and flow of cells [50]. Within the inner cylinder rachis, there exists steady long range flows of cytoplasm, which indicates gradients of stress along the axis of symmetry of the germline. The cells are connected to the inner cylinder called rachis via circular openings/holes ranging microns in radii. Gradients or differences of stress across the boundary of cellular layer and the fluid-filled inner cylinder would drive flows of cytoplasm. Together, this forms a description of a hydrodynamic system that capture the essential features of the real and albeit more complicated germline organ.

Before delving into considerations of geometry and formalism, we must identify the hydrodynamics fields and their corresponding forces. Due to azimuthal symmetry around DP/x-axis, we shall only limit ourselves to fluxes along the axis of symmetry. Due to conservation of volume within the cellular layer as well as fluid within rachis, we should have the following hydrodynamic fluxes: cell volume flux  $Q_c$ , rachis flux  $Q_r$  that must satisfy the corresponding conservation laws. These fluxes develop in terms of velocity fields within the respective layers. Cell density also can only change via local birth and death events or as a result the cell density flux  $J_c = nv_c$  and must satisfies a conservation of law, as result we should obtain another hydrodynamic field  $J_c$ . However this is not an independent field of its' own but rather transpires through the cell velocity field. We identify the conjugate forces  $f_c$  &  $f_r$  respectively to be the axial gradient of cell pressure  $P_c$  and rachis pressure  $P_r$ ,

$$f_c = -\partial_x P_c \quad \& \quad f_r = -\partial_x P_r$$

To derive the constitute relationship between the fluxes and forces we appeal to linear irreversible thermodynamics. One can write the isothermal (at temperature  $T$ ) entropy production ( $\dot{S}$ ) to be,

$$T\dot{S} = \int [f_c Q_c + f_r Q_r] dx = \int [(-\partial_x P_c) Q_c + (-\partial_x P_r) Q_r] dx \quad (3.1)$$

Using linear Onsager relations one can obtain,

$$-\partial_x P_c = \lambda_c Q_c + \lambda_{cr} Q_r \quad (3.2)$$

$$-\partial_x P_r = \lambda_{rc} Q_c + \lambda_r Q_r \quad (3.3)$$

where  $\lambda_c, \lambda_r$  are straight coupling terms, while  $\lambda_{cr}$  &  $\lambda_{rc}$  represent cross coupling terms. Because of time asymmetry in this system,  $\lambda_{rc} = -\lambda_{cr}$ . We later derive a similar relationship from arguments based on fluid flows and develop a more intuitive interpretation of the couplings and compare this general form.



## 3.1.1 1 D hydraulic description

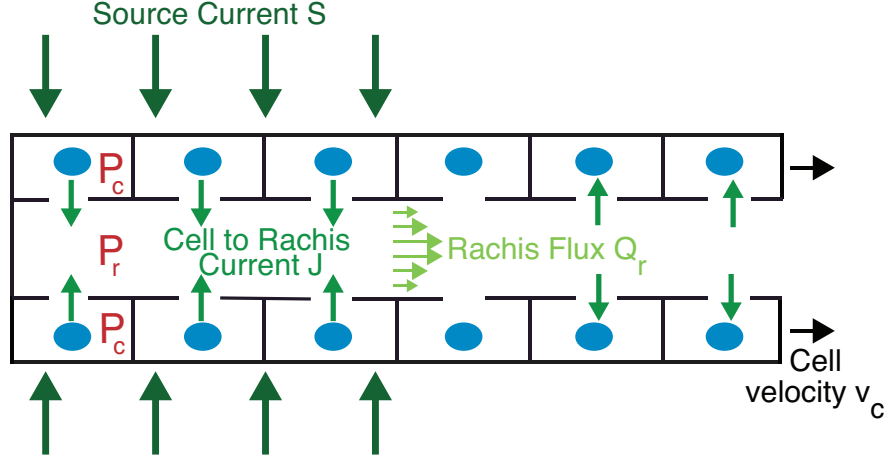


**Figure 3.1:** Schematic of hydrodynamic fluxes in the germline and corresponding physical variables.

We consider a one-dimensional representation of the gonad with positions  $x \in [0, L]$  along the distal-proximal axis, where  $L$  is the gonad-length (Fig. 3.1). We first consider the conservation of volume in terms of the flux balances,

$$\partial_t A_c + \partial_x (v_c A_c) = S - J \quad (3.4)$$

$$\partial_t A_r + \partial_x (v_r A_r) = J \quad (3.5)$$

Here  $A_c$  and  $A_r$  denote the cross-sectional areas of the germline that correspond to the germ cell layer and the rachis, respectively. The average velocities of rachis cytoplasm and cells are denoted  $v_r$  and  $v_c$ , respectively and are defined as,

$$v_r = \frac{Q_r}{A_r} \quad \& \quad v_c = \frac{Q_c}{A_c} \quad .$$

Source current due to material uptake from outside into cell layer is denoted  $S$ , and  $J$  signifies the germ cell to rachis current. This current  $J$  is driven by the difference in cell pressure  $P_c$  and rachis pressure  $P_r$ , and given by

$$J = \alpha(P_c - P_r) \quad . \quad (3.6)$$

Here,  $\alpha$  is a dissipative coefficient that captures the permittivity of the tissue-fluid interface that mediate such exchanges. Without a specific model in mind, some general considerations of the system can inform us about this dissipative coefficient. An interpretation  $\alpha$  is simply that it is the current generated for a unit pressure difference at the interface of tissue and fluid. Since this current originates due to hydrodynamic exchanges through holes, it should depend on the density of holes. Naturally,  $\alpha \sim n$ , with  $n$  being the linear density of cells as well as holes, hence  $\alpha \sim l_c^{-1}$ . Also,  $\alpha$  should

decrease with viscosity of the cytoplasm  $\eta$ , while it should diverge if  $\eta \rightarrow 0^+$ , hence another relationship is  $\alpha \sim \eta^{-1}$ . We will discuss the specific form of  $\alpha$  in the next section in detail.

The force balance in germ cells and rachis can be expressed according to

$$-\partial_x P_c = \gamma_o v_c + \gamma_r (v_c - v_r) \quad (3.7)$$

$$-\partial_x P_r = \gamma_r (v_r - v_c) \quad , \quad (3.8)$$

where  $\gamma_o$  is a coefficient of friction between germ cells and the outside, and  $\gamma_r$  is an effective friction coefficient that describes frictional interactions between germ cell layer and the fluid within the rachis.

In the steady state, where the cross-sectional areas  $A_c$  &  $A_r$  does not change over time, the conservation laws Eqs.(3.4-3.5) reduce to,

$$\partial_x Q_c = S - J \quad (3.9)$$

$$\partial_x Q_r = J \quad . \quad (3.10)$$

These equations must be supplemented by boundary conditions. From the point of view of viscous flow within a pipe it is natural to choose pressure boundary conditions and prescribe them at both ends of the gonad, however due to the presence of exchange and leakage (see Appendix B.) it is non-trivial to identify the appropriate pressure condition at the inlet and outlet. Hence we motivate the boundary conditions from our knowledge of the real system and choose to prescribe boundary conditions in terms of the fluxes instead.

The germline tube is closed at the distal tip hence we propose that both fluxes of both germ cells as well as rachis fluid at the distal tip ( $x = 0$ ) vanish:  $Q_c(0) = 0$  and  $Q_r(0) = 0$ . At the proximal end ( $x = L$ ) we also see that the inner-tube closes and, we have  $Q_r(L) = 0$ . Note that volume conservation implies  $Q_c(L) = \int S dx$ , i.e. the volume flux leaving the system at the proximal end  $A_c v_c(L)$  equals the total material uptake  $\int S dx$  from the outside.

### 3.1.2 Hydrodynamic flows through rachis bridges

Before engaging in particular solutions of the tissue hydraulics, it is convenient to build a hydrodynamic view of how open cells such as the germ cells here may drive flows to reservoirs. This will help us understand the material basis of the current  $J$  and the nature of local pressure differences that drive such exchanges. As a zeroth order approximation, one can take a perfectly cell with radius  $R_c$  and opening of radius  $r$ . If  $r \ll R_c$ , then the flow field around the hole/pore is hardly affected by the boundaries of the cell and effectively maps to a problem of flow through a circular orifice [66]. With the convenient choice of oblate coordinate system, this problem can be exactly solved. This result is originally due to Sampson [72] and is often termed as Sampson's

flow.

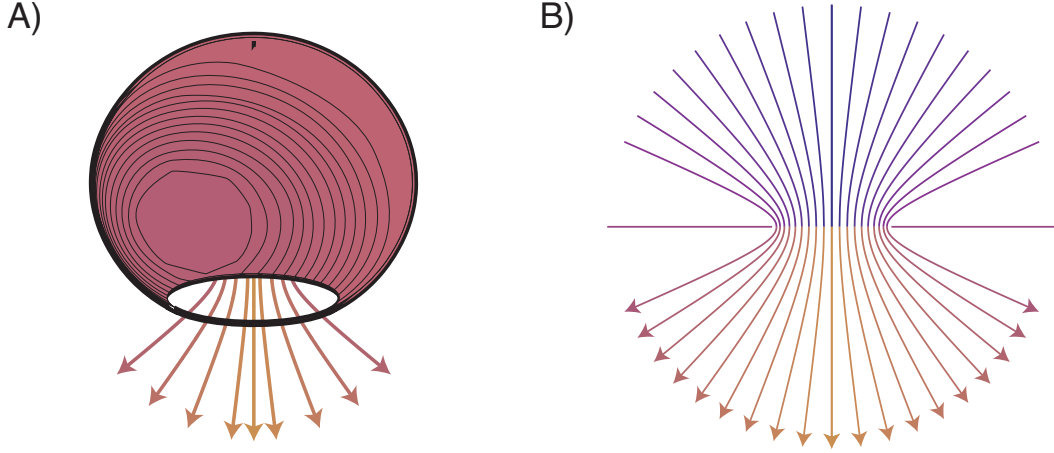


**Figure 3.2:** A) Schematic depiction of cell with a hole. B) Streamlines are shown for Sampson's flow

In this case one can assume that the pressure deep within the cell is steady and is given by  $P_c$  and  $P_r$  for the reservoir. The relationship between  $\Delta p = P_c - P_r$  and volume flux  $q$  is given by,

$$q = \frac{r^3}{3\eta} \Delta p \quad . \quad (3.11)$$

An equivalent result is also derived by Roscoe employing an electrostatic analogy [73]. The scaling relationship can also be observed by the starting from a generalized pipe flow where,

$$q \sim \frac{r^4}{\eta} \left( -\frac{\partial p}{\partial z} \right) \quad (3.12)$$

The limiting length-scale here is the radius of the hole which sets the length-scale for pressure drop, hence

$$q \sim \frac{r^4}{\eta} \left( \frac{\Delta p}{r} \right) = \frac{r^3}{\eta} \Delta p \quad . \quad (3.13)$$

One might wish to take the explicit geometry of the germ cells into account and extend from an infinite pool to a more realistic geometry of spherical cap. If the diameter of the hole makes an angle of  $2\omega$  at the center of the spherical cap, a correction is found [74]. For small  $\omega$  around  $\pi$  we find,

$$q \simeq \frac{r^3}{3\eta} \Delta p \left[ 1 - \frac{1}{4}(\omega - \pi)^2 \right] \quad . \quad (3.14)$$

Note that the scaling is unaffected. The current is given by  $J = q/l_c$ , hence we obtain the explicit relationship,

$$J = \alpha \Delta p = \frac{r^3}{3\eta l_c} \Delta p \quad . \quad (3.15)$$

The nonlinear dependence on  $r$  implies significant influence on current for even small changes of hole radii, e. g. if  $r \rightarrow r(1 + \epsilon)$  then the corresponding  $J \rightarrow J(1 + \epsilon)^3 \sim J(1 + 3\epsilon)$ . Hence for an overall 5% change of hole radius a 15% effect can be found in the current.

### 3.1.3 Solutions to simplified geometries

For simplicity we consider the case where the areas  $A_c$  and  $A_r$  are constant along the gonad. In this case volume balance in steady state reads

$$\partial_x Q_c = S - \alpha(P_c - P_r) \quad (3.16)$$

$$\partial_x Q_r = \alpha(P_c - P_r) \quad , \quad (3.17)$$

where  $Q_c = A_c v_c$  and  $Q_r = A_r v_r$  are the cell and rachis volume fluxes, respectively. Combining these equations with the force-balance equations (Eqs. 3.7, 3.8) we obtain the velocity profiles which read

$$\partial_x^2 Q_c = \partial_x S + \frac{\alpha(\gamma_o + 2\gamma_r)}{A_c} Q_c - \frac{2\alpha\gamma_r}{A_r} Q_r \quad (3.18)$$

$$\partial_x^2 Q_r = -\frac{\alpha(\gamma_o + 2\gamma_r)}{A_c} Q_c + \frac{2\alpha\gamma_r}{A_r} Q_r \quad . \quad (3.19)$$

In redefined nondimensional units we obtain

$$\partial_x^2 Q_c = \partial_x S + \beta_c Q_c - \beta_r Q_r \quad (3.20)$$

$$\partial_x^2 Q_r = -\beta_c Q_c + \beta_r Q_r \quad . \quad (3.21)$$

Here  $\beta_c = \alpha(\gamma_o + 2\gamma_r)/A_c$  and  $\beta_r = 2\alpha\gamma_r/A_r$  are nondimensional coefficients. This constitutes a linear system of second order differential equations with the nonhomogeneous term  $\partial_x S$  and an analytic solution can be obtained but a closed form is difficult to represent. We shall however discuss the analytical solutions in the case of a simple piecewise linear source profile.

#### Step function Source:

We choose the source profile to be,

$$S(x) = s_0 \Theta(0.6 - x) \quad x \in [0, 1]$$

where  $\Theta$  represents the Heaviside theta function. As a result there is constant source current of  $s_0$  until 0.6 fraction of the tube, beyond which the source disappears. This implies that  $\partial_x S(x) = -s_0 \delta(x - 0.6)$ . We shall solve the Eq.3.20-3.21 by employing a

### 3.1 Hydrodynamics of the germline

---

jump condition at  $x = 0.6$ ,

$$\partial_x S(x = 0.6) = -s_0 \quad . \quad (3.22)$$

Hence both prior and beyond  $x = 0.6$ , the set of equation reduces to the homogeneous form and can be expressed as,

$$\partial_x^2 \begin{pmatrix} Q_c \\ Q_r \end{pmatrix} = \begin{pmatrix} \beta_c & -\beta_r \\ -\beta_c & \beta_r \end{pmatrix} \begin{pmatrix} Q_c \\ Q_r \end{pmatrix} \quad (3.23)$$

$$= \boldsymbol{\beta} \begin{pmatrix} Q_c \\ Q_r \end{pmatrix} \quad . \quad (3.24)$$

The eigensystem of the linear matrix  $\boldsymbol{\beta}$  determines the solutions to this linear equation. Note that  $Tr(\boldsymbol{\beta}) = \beta_c + \beta_r$  but the determinant  $Det(\boldsymbol{\beta}) = 0$ , indicating that eigenvalues must  $Eig = 0, \beta_c + \beta_r$ . To evaluate this system we implement the following ansatz within Eq.3.23,

$$\begin{pmatrix} Q_c \\ Q_r \end{pmatrix} = \begin{pmatrix} Q_c^0 \\ Q_r^0 \end{pmatrix} e^{\pm \lambda x} \quad (3.25)$$

and obtain,

$$\lambda_{(1)}^2 = 0 \quad \& \quad \lambda_{(2)}^2 = \beta_c + \beta_r \quad (3.26)$$

and the respective eigenvectors ,

$$\begin{pmatrix} Q_c^{(1)} \\ Q_r^{(1)} \end{pmatrix} = \begin{pmatrix} \frac{\beta_c}{\beta_r} \\ 1 \end{pmatrix} \quad \& \quad \begin{pmatrix} Q_c^{(2)} \\ Q_r^{(2)} \end{pmatrix} = \begin{pmatrix} -1 \\ 1 \end{pmatrix} \quad . \quad (3.27)$$

Hence the general solution is give by,

$$\begin{pmatrix} Q_c(x) \\ Q_r(x) \end{pmatrix} = (c_1 + c_2 x) \begin{pmatrix} \frac{\beta_c}{\beta_r} \\ 1 \end{pmatrix} + (c_3 e^{-\lambda(2)x} + c_4 e^{\lambda(2)x}) \begin{pmatrix} -1 \\ 1 \end{pmatrix} \quad . \quad (3.28)$$

The constant factors can be evaluated using boundary conditions. Note that,

$$\partial_x Q_c + \partial_x Q_r = c_2 \left( \frac{\beta_c}{\beta_r} + 1 \right) = S(x) \quad (3.29)$$

which determines the value of  $c_2$ .

Evaluating at  $x = 0$  using the boundary condition,

$$\begin{pmatrix} Q_c(0) \\ Q_r(0) \end{pmatrix} = c_1 \begin{pmatrix} \frac{\beta_c}{\beta_r} \\ 1 \end{pmatrix} + (c_3 + c_4) \begin{pmatrix} -1 \\ 1 \end{pmatrix} = \begin{pmatrix} 0 \\ 0 \end{pmatrix} \quad (3.30)$$

$$\implies \tag{3.31}$$

$$c_1 \frac{\beta_c}{\beta_r} - (c_3 + c_4) = 0 \tag{3.32}$$

$$c_1 + c_3 + c_4 = 0 \tag{3.33}$$

which yields,  $c_1 = 0$  and  $c_3 = -c_4 = c$  and  $c_2 = s_0/(\beta_c/\beta_r + 1)$ . Hence the solution for  $x \in [0, 0.6]$  reduces to,

$$\begin{pmatrix} Q_c(x) \\ Q_r(x) \end{pmatrix} = \frac{s_0}{\frac{\beta_c}{\beta_r} + 1} x \begin{pmatrix} \frac{\beta_c}{\beta_r} \\ 1 \end{pmatrix} + c \left( e^{-\lambda(2)x} - e^{\lambda(2)x} \right) \begin{pmatrix} -1 \\ 1 \end{pmatrix} . \tag{3.34}$$

Evaluating at  $x = 1$  using the boundary condition,

$$Q_r(1) = 0 = \bar{c}_1 + \bar{c}_2 + (\bar{c}_3 e^{-\lambda(2)} + \bar{c}_4 e^{\lambda(2)}) \tag{3.35}$$

and  $S(1) = 0$  we find,

$$\bar{c}_1 = -(\bar{c}_3 e^{-\lambda(2)} + \bar{c}_4 e^{\lambda(2)}) \tag{3.36}$$

which gives the following solution for  $x \in [0.6, 1]$ ,

$$\begin{pmatrix} Q_c(x) \\ Q_r(x) \end{pmatrix} = -(\bar{c}_3 e^{-\lambda(2)} + \bar{c}_4 e^{\lambda(2)}) \begin{pmatrix} \frac{\beta_c}{\beta_r} \\ 1 \end{pmatrix} + (\bar{c}_3 e^{-\lambda(2)x} + \bar{c}_4 e^{\lambda(2)x}) \begin{pmatrix} -1 \\ 1 \end{pmatrix} . \tag{3.37}$$

Moreover due to steady state condition  $Q_c(1) = \int S(x) dx = 0.6s_0$  which gives the condition,

$$-(\bar{c}_3 e^{-\lambda(2)} + \bar{c}_4 e^{\lambda(2)}) = \frac{0.6s_0}{\frac{\beta_c}{\beta_r} + 1} \tag{3.38}$$

The Eq.3.34,3.37 must match at the boundary at  $x = 0.6$  and yields the following condition,

$$c = \frac{\bar{c}_3 e^{-\lambda(2)0.6} + \bar{c}_4 e^{\lambda(2)0.6}}{e^{-\lambda(2)0.6} - e^{\lambda(2)0.6}} . \tag{3.39}$$

It is interesting to note that in the beginning due to the presence of source the linear part of the  $Q_c$  is non-zero and may dominate for high values of  $\beta_c/\beta_r$ . We present the numerically obtained solutions( [75, 76]) in Fig.3.3.

### 3.1 Hydrodynamics of the germline

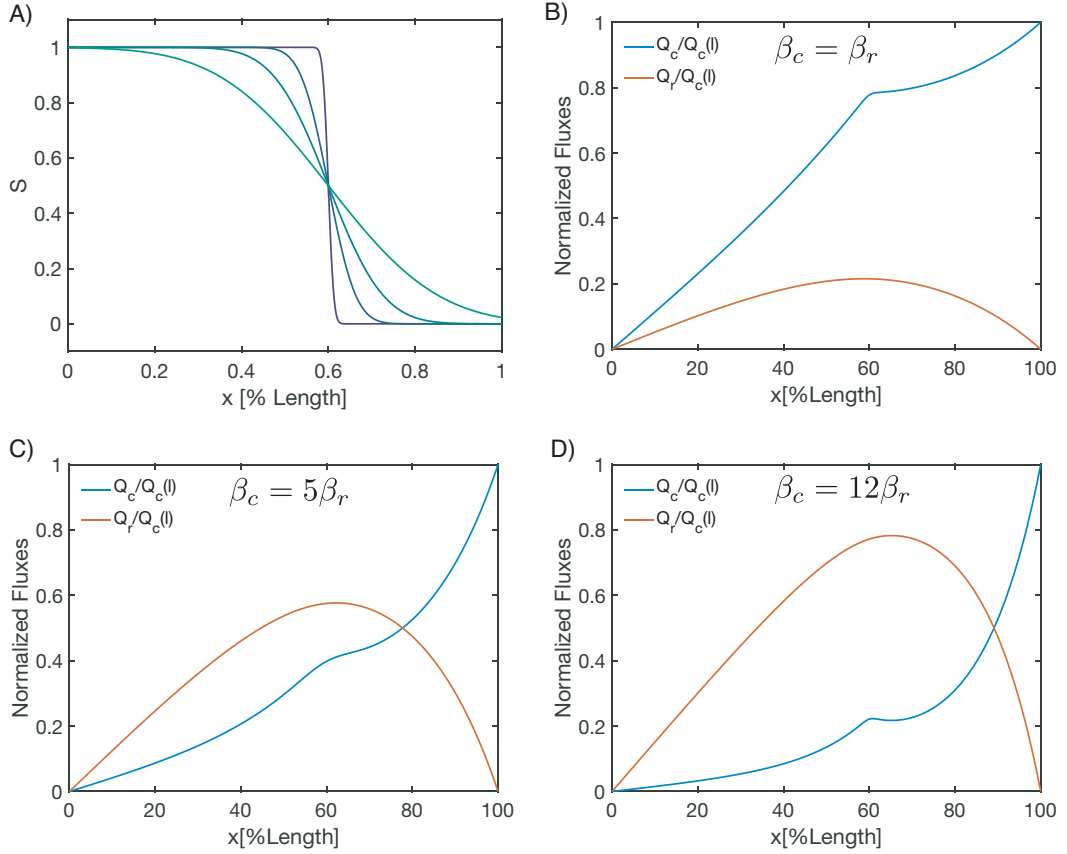


**Figure 3.3:** A) A source profile is presented ,approximated by the complimentary error function; for solutions the the steepest erfc is chosen. B)-D) Normalized fluxes are presented for various  $\beta_c/\beta_r$

We find that the effective magnitude is purely a function of  $\int S dx = Q_c(1)$ , hence we presented fluxes normalized by  $Q_c(1)$ . The relative difference of  $\beta_c$  and  $\beta_r$  drive the partitioning of fluxes between the cell volume and rachis flux. We also note that upon increase of  $\beta_c/\beta_r$  the peak rachis flux increases, however the maximum value of  $Q_r$  asymptotically approaches  $Q_c(1)$  (see Fig.3.5) . To understand the effect of leakage on the system we modify the source profile to be,

$$S(x) = s_0 (2\Theta(0.6 - x) - 1) \quad x \in [0, 1]$$

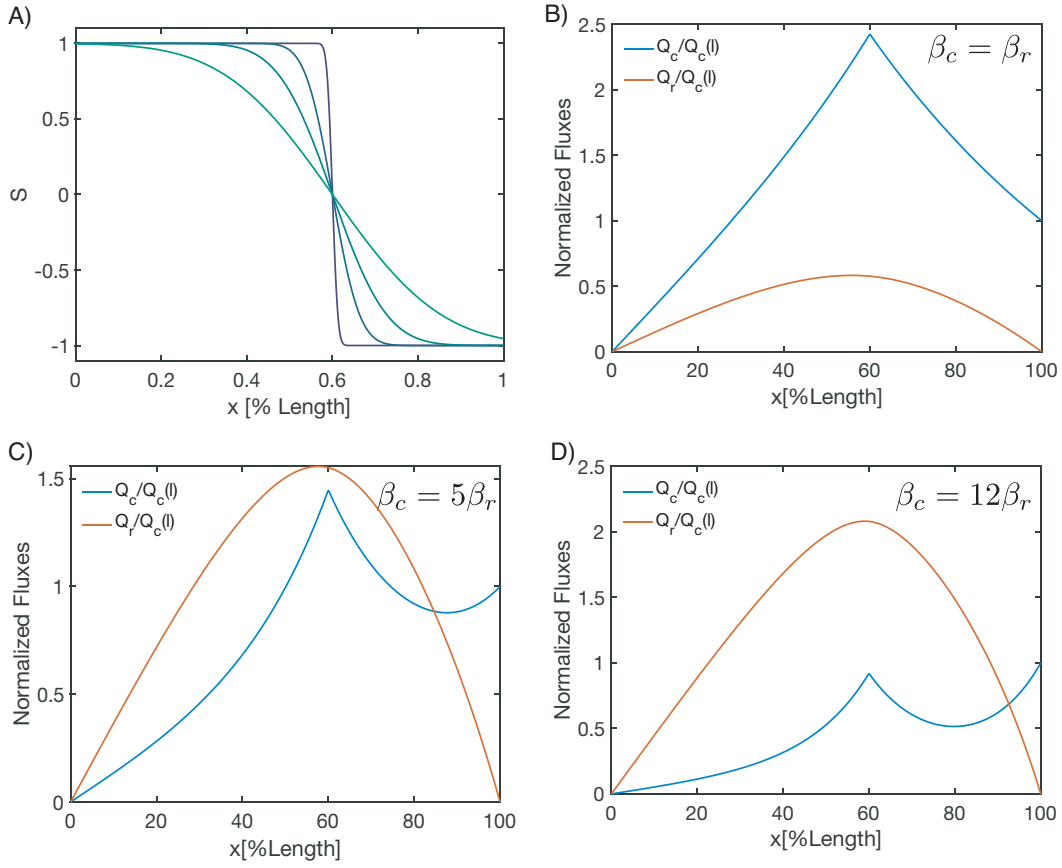


**Figure 3.4:** A) A source profile with proximal leakage is presented, approximated by the complimentary error function; for solutions the the steepest erfc is chosen. B)-D) Normalized fluxes are presented for various  $\beta_c/\beta_r$

We find a similar qualitative behavior in terms of the spatial profile of the fluxes, however the asymptotic values of peak  $Q_r$  with tuning  $\beta_c/\beta_r$  exceed  $Q_c(1)$  (see Fig.3.5)

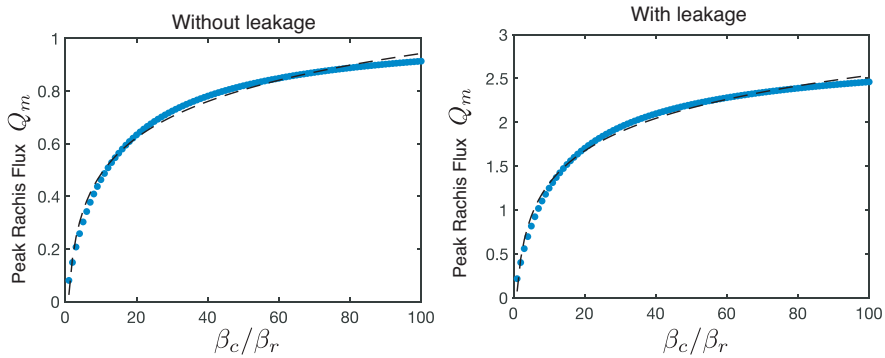


**Figure 3.5:** A) Maxima of normalized rachis flux as a function of relative frictions for source profile without leakage. B) Maxima of normalized rachis flux as a function of relative frictions for source profile with leakage.

**Comparison to experiments:**



We next approximate the experimentally obtained source current profile with a function given by  $S(x) = a_0 + \sum_{n=1}^3 (a_n \cos(nx/L) + b_n \sin(nx/L))$ . This provides us with a smooth and continuous representation  $S(x)$  of the data (Fig.2.25 dashed line). We then fit numerically determined solutions of Eqs. 3.20 and 3.21 to the profile of experimentally obtained cell volume flux and rachis flux  $Q_c$  and  $Q_r$  using  $\beta_c$  and  $\beta_r$  as fit parameters (Fig.3.6).

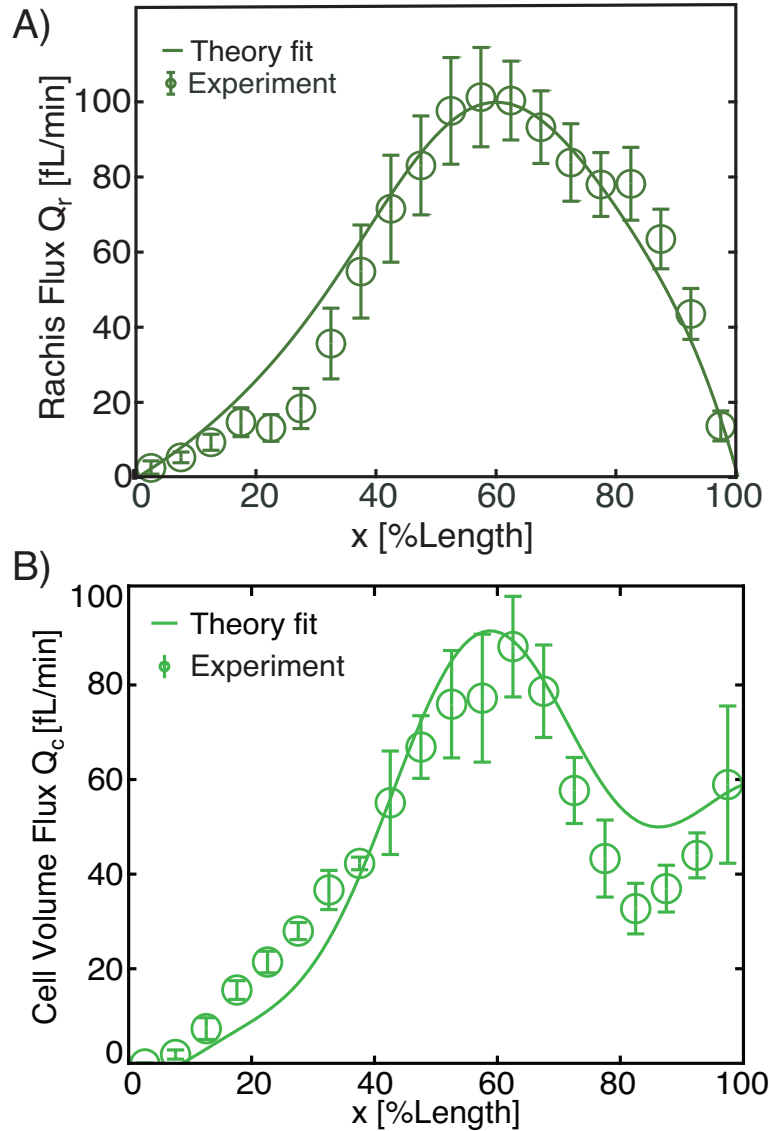


**Figure 3.6:** A) Cytoplasmic flux  $Q_r$  through the rachis as a function of position along the gonad. Open circles,  $Q_r$  determined experimentally from 10 gonad arms. Solid line, best parameter theory fit. B) Inferred cell volume flux  $Q_c$  as a function of position along the gonad. Open circles, Solid line, best parameter theory fit.

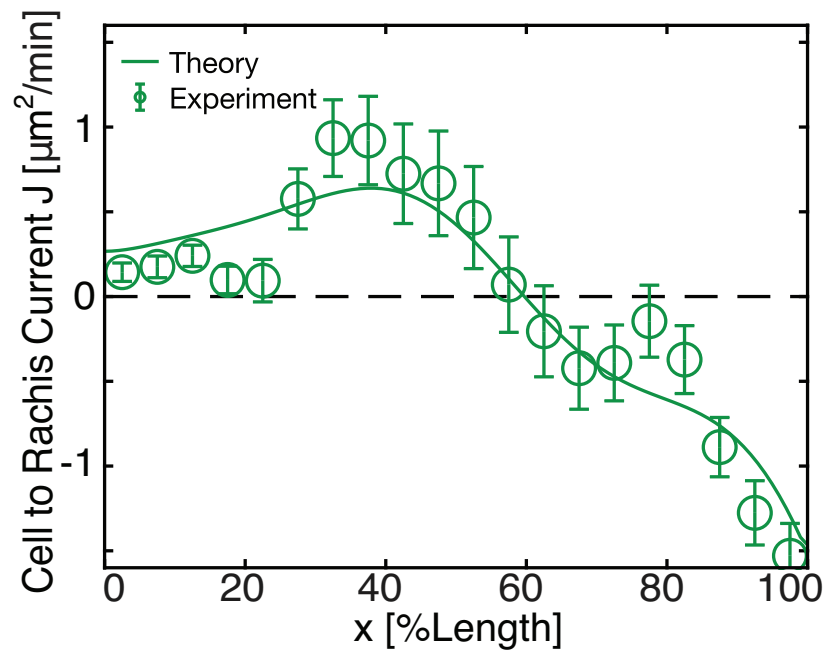


**Figure 3.7:** Germ cell to rachis current is represented as a function of the position along the DP-axis of the gonad. Open circles indicate experimentally inferred data, solid lines are derived from fit solutions in Fig.3.6

## 3.2 Germline Mechanics and Stability of Symmetric States

To investigate whether the inversion of cell to rachis current and the associated pressure difference could lead to an inflation related instability we investigate the stability of the germline at a given cross-section. Two aspects of the germline mechanics play important role here: 1) the stability of the rachis structure i.e. the radial mechanics, 2) the azimuthal stability of coupled homogeneous germ cells. Without loss of generality we shall restrict the discussion here to idealized geometries of the germline, where the rachis tube and the tissue tube are concentric. We shall first discuss the radial mechanics, as it is non-trivial how a tissue structure with openings could attain stability despite effects of cortical tension.

### 3.2.1 Radial mechanics of the germline tissue

In the standard pictures of tissue mechanics, it is inherently assumed that the cell volumes are enclosed and as a result the incompressibility criterion leads to local volume elasticity [16, 77–79]. Unlike such regular tissues, the germline consists of open germ cells with rachis bridges that allow volume exchange. These rachis bridges are cytokinetic remnants consisting of various proteins such as the long and short isoform of the anilin protein *ani-1* & *ani-2* [49, 80], which have been argued to be a key molecular player in the stability of these cytokinetic bridges. In this section we shall entertain the idea that the influence of ring packings can affect the stability of the germline. Similar to the approaches discussed in [16, 77], we shall adopt a discrete idealized mechanical model and try to deduce a work function/pseudo-potential in terms of geometric variables.

We consider a cross-section of the germline and a column of germ cells that are radially distributed. This column consists of a single layer of cells and width  $l_c$ . The number of cells are denoted by  $N_c = \rho l_c$ , where  $\rho$  is the linear density of cells as defined before. The outer and inner radii of the germline is noted as  $R_e$  &  $R_i$  (See Fig.3.8). We propose the following work function,

$$W = \sum_{k=1}^{N_c} \left( \sum_{s \in \{a,b,l\}} T_s^{(k)} A_s^{(n)} + \sum_e \lambda_e l_e + K_r^{(k)} (r^{(k)} - r_0)^2 \right) \quad (3.40)$$

where index  $k$  indicates the cell identity and index  $s$  denotes the surfaces within the cell of  $(a, b, l)$  kind, indicating apical, basal and lateral locations.  $T_s^{(n)}$  is the tension of the surface  $s$  within cell  $k$ . The terms  $\lambda_e l_e$  captures line tension of interface edges. The last term captures the elasticity of rachis bridges where  $K_r$  is the the elastic modulus and the  $r_0$  is the rest length of the rachis bridges. Note that there no explicit volume control/elasticity terms have been introduced .

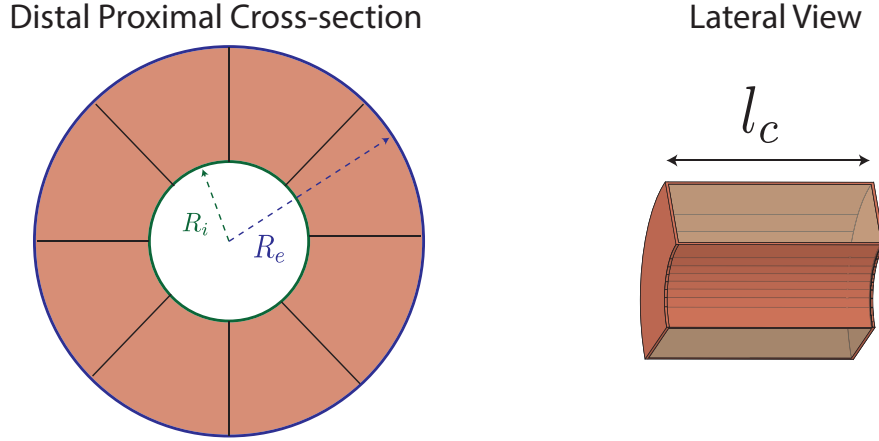


**Figure 3.8:** Schematic of a germline cross-section showing the sagittal and lateral view.

We shall argue that the effects of the edge tensions can be absorbed within the lateral cortical tensions and hence we can ignore. Next we shall discuss the case where all cells are identical and seek solutions of the homogeneous kind. For the idealized geometry depicted in Fig.3.8 expressing all the contributions explicitly in terms of  $R_e$ ,  $R_i$ ,  $n$  we obtain,

$$W[R_e, R_i, n] = T_l \left( \pi(R_e^2 - R_i^2) + (n-1)l_c(R_e - R_i) \right) + T_b 2\pi R_e l_c + T_b 2\pi R_i l_c + nK_r (r - r_0)^2 .$$

Furthermore we shall argue that  $T_l = T_b = T_c$ , implying no sharp distinction within the germ cell cortex except the rachis cortex with  $T_a = T_r$ . We also propose  $r_n = mR_i n$ , indicating that the rings stretch/adjust if the underlying rachis surface stretches. The outer boundary is constrained by the extracellular matrix and neighboring organs and we shall impose  $R_e$  to be fixed. This reduces the ensemble to  $[R_i, n]$  and allows us to nondimensionalize all the lengthscales. We redefine,

$$R = \frac{R_i}{R_e}, \quad \tilde{l}_c = \frac{l_c}{R_e}, \quad t_r = \frac{T_r}{T_c}, \quad k_r = \frac{K_r}{\pi T_c}, \quad \omega = \frac{W}{\pi R_e^2 T_c}$$

and after a little bit of algebra we obtain,

$$\omega[R, n] = \left( N_c k_r (m - m_0)^2 - 1 \right) R^2 - \left( \frac{N_c - 1}{\pi} - t_r \right) \tilde{l}_c R + \left( 2 + \frac{N_c - 1}{\pi} \right) \tilde{l}_c . \quad (3.41)$$

Here the reaction coordinate  $R \in [0, 1]$ , where the extrema presents the physical case of a closed ( $R = 0$ ) or a completely open ( $R = 1$ ) rachis.

Note that in the absence of the ring elasticity ( $k_r = 0$ ), the work function resembles a nucleation profile, only yielding boundary stable states  $R = 0$  or  $R = 1$ .

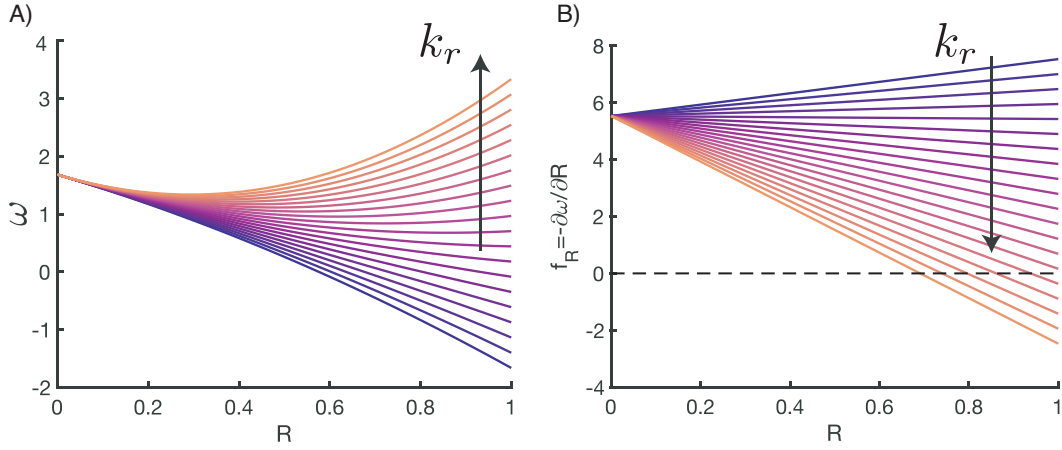


**Figure 3.9:** A) Work function  $\omega[R]$  depicted for various choices of  $k_r$ , B) Corresponding force associated with the work function

To obtain the extrema of the work-function, we seek zeros of the force balance law,

$$f_R = -\frac{\partial\omega}{\partial R} = -2 \left( N_c k_r (m - m_0)^2 - 1 \right) R + \left( \frac{N_c - 1}{\pi} - t_r \right) \tilde{l}_c \quad (3.42)$$

and find the steady state  $R_{ss}$  to be,

$$R_{ss} = \frac{N_c - 1 - \pi t_r}{2\pi (N_c k_r (m - m_0)^2 - 1)} \tilde{l}_c \quad (3.43)$$

$R_{ss}$  presents a stable solution if and only if,

$$\frac{\partial^2\omega}{\partial R^2} = 2 \left( N_c k_r (m - m_0)^2 - 1 \right) > 0 \quad (3.44)$$

which yields a stability criteria on the number of cells,

$$N_c > N_0 = \frac{1}{k_r (m - m_0)^2} \quad (3.45)$$

Furthermore  $R > 0$  implies that,

$$\frac{N_c - 1}{\pi} > t_r \quad (3.46)$$

and for

$$\frac{N_c - 1}{\pi} \leq t_r \quad (3.47)$$

the boundary minima  $R = 0$  is the stable solution. This allows us to obtain the phase diagram for the radial stability of the germline.

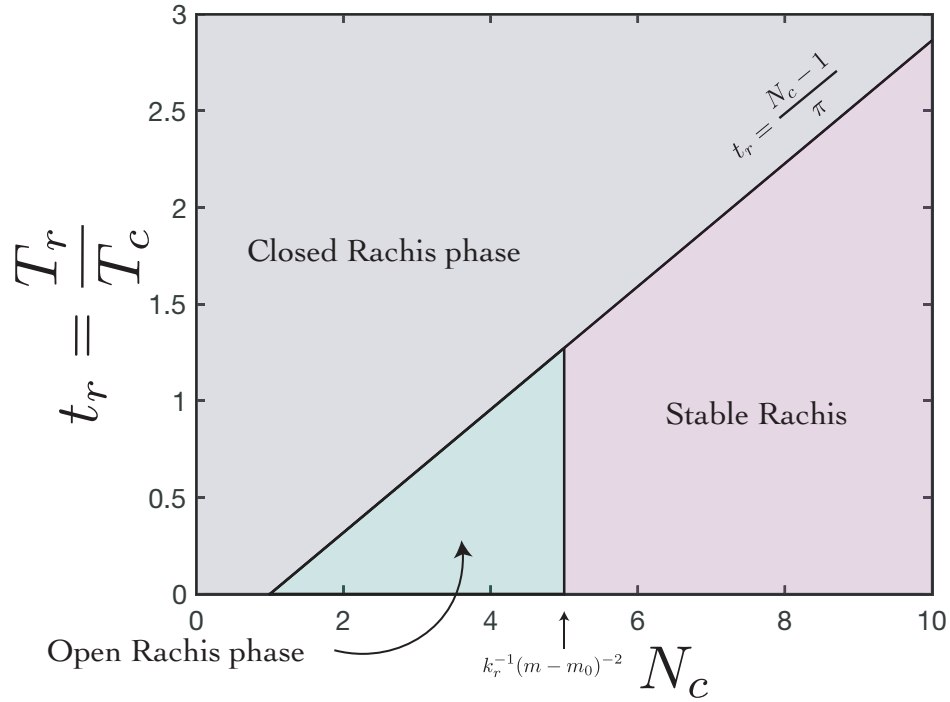


**Figure 3.10:** Phase diagram of the germline structure is obtained for high elasticity regime.

For high values of rachis tension  $t_r$ , we obtain a closed rachis phase. Stable finite values of  $R$  is only obtained for  $N_c > N_0 = 1/k_r(m - m_0)^2$ , which is easily satisfied for high elastic modulus  $k_r$ . Hence elastic effects of the rachis bridges can effectively stabilize the radial mechanics of the germline, even in the absence of explicit volume control. For low ring elasticity the open rachis phase dominates and only the boundary solutions are found. In this section we establish the basis for radial stability of the germline and rachis, in the following section we shall ascertain how cells around the rachis maintain azimuthal symmetry. For this purpose we shall simply assume that the radii are at equilibrium.

### 3.2.2 Azimuthal stability of a germ-cell doublet

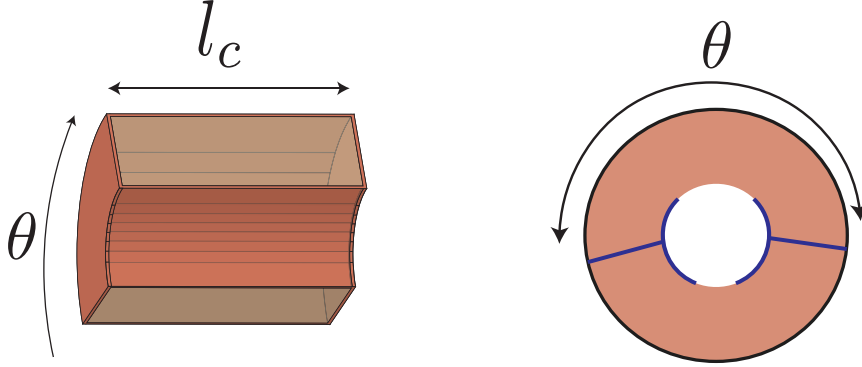


**Figure 3.11:** Schematic of a germ cell doublet with azimuthal splay of  $\theta$  and distal-proximal depth of  $l_c$ .

The change in sign of the germ cell to rachis current  $J$  at  $x \simeq 0.6 L$  implies an inversion of the pressure difference  $P_c - P_r$ . We now discuss how the stability of a pair of cells located along the gonad at position  $x$  depends on the pressure profiles in the gonad.

We consider two cells with total cross-section area  $A_c$  covering the azimuthal angles  $\theta_1$  and  $\theta_2$ , respectively, with the constraint that  $\theta_1 + \theta_2 = 2\pi$ .

The volumes of the two cells are given by  $V_i = A_c \theta_i l_c / (2\pi)$ , where  $l_c$  is the distal-proximal cell length. Because of material exchange the cell volume obeys,

$$\frac{dV_i}{dt} = S_i l_c - J_i l_c \quad , \quad (3.48)$$

where  $S_i l_c$  is the rate of volume uptake of cells  $i = 1, 2$  from outside due to source current  $S_i$  and  $J_i l_c$  denotes the rate of volume loss from cell to rachis due to exchange via holes.

We propose the following model,

$$S_i = S_0 \theta_i / (2\pi) \quad \& \quad J_i = \alpha_i (P_c - P_r) \quad (3.49)$$

which simply implies that cells with larger basal area will take up more material. We have introduced  $S_0 = S(x)$  and  $\alpha_i \simeq r_i^3 / (3l_c \eta)$ , where the radii  $r_i$  of rachis bridges can differ from cell to cell. The rate of change of cell volume can be written as,

$$\frac{dV_i}{dt} = \frac{A_c \theta_i}{2\pi} \frac{dl_c}{dt} + \frac{l_c A_c}{2\pi} \frac{d\theta_i}{dt} = S_0 l_c \frac{\theta_i}{2\pi} - \alpha_i l_c (P_c - P_r) \quad . \quad (3.50)$$

The total volume change is,

$$\frac{dV_1}{dt} + \frac{dV_2}{dt} = A_c \frac{dl_c}{dt} = S_0 l_c - (\alpha_1 + \alpha_2) l_c (P_c - P_r) \quad . \quad (3.51)$$

We define the relative volume difference  $\nu = (V_1 - V_2) / (V_1 + V_2)$ , which obeys  $\nu =$

$(\theta_1 - \theta_2)/(2\pi)$ . We therefore consider the dynamics of  $\nu$  as given by

$$\frac{d\nu}{dt} = \frac{P_c - P_r}{A_c} ((\alpha_1 + \alpha_2)\nu - \alpha_1 + \alpha_2) \quad . \quad (3.52)$$

In general,  $\alpha_i$  may depend on cell volume. We choose that  $r_i \simeq r_0\theta_i/(2\pi)$ , implying a correlation between the rachis bridge radius and cell size . We then have  $\alpha_i = \alpha_0(\theta_i/(2\pi))^3$ , where  $\alpha_0 = r_0^3/(3\eta l_c)$ . We find

$$\frac{d\nu}{dt} = -\frac{\alpha_0(P_c - P_r)}{2A_c}(1 - \nu)(1 + \nu)\nu \quad . \quad (3.53)$$

This equation has three steady-state solutions given by  $\nu = 0$  and  $\nu = \pm 1$ , corresponding to the solution of two cells of equal size, and two solutions where in each case one of the two cells fills the entire cross-section.

The stability of all three fixed points is shown in Fig.3.12, where the rate of change of relative volume difference  $d\nu/dt$  is plotted as a function of  $\nu$ . For  $P_c > P_r$  the symmetric steady-state with  $\nu = 0$  is stable, while the two asymmetric steady-states are unstable. As soon as the pressure difference changes sign , the symmetric steady-state becomes unstable and the system reaches one of the two asymmetric steady-states by spontaneous symmetry breaking. We term this spontaneous symmetry breaking phenomena driven by pressure inversion "hydraulic instability"

A linear stability analysis can be performed around the fixed point  $\nu^*$  by introducing a perturbation of  $\delta\nu$ ,

$$\frac{\delta\nu}{dt} = -\frac{\alpha_0(P_c - P_r)}{2A_c} (1 - 3(\nu^*)^2) \delta\nu \quad (3.54)$$

which implies,

$$\left. \frac{\delta\nu}{dt} \right|_0 = -\frac{\alpha_0(P_c - P_r)}{2A_c} \delta\nu \quad \& \quad \left. \frac{\delta\nu}{dt} \right|_{\pm 1} = 2\frac{\alpha_0(P_c - P_r)}{2A_c} \delta\nu \quad (3.55)$$

which shows stability switch when the sign of  $P_c - P_r$  changes.



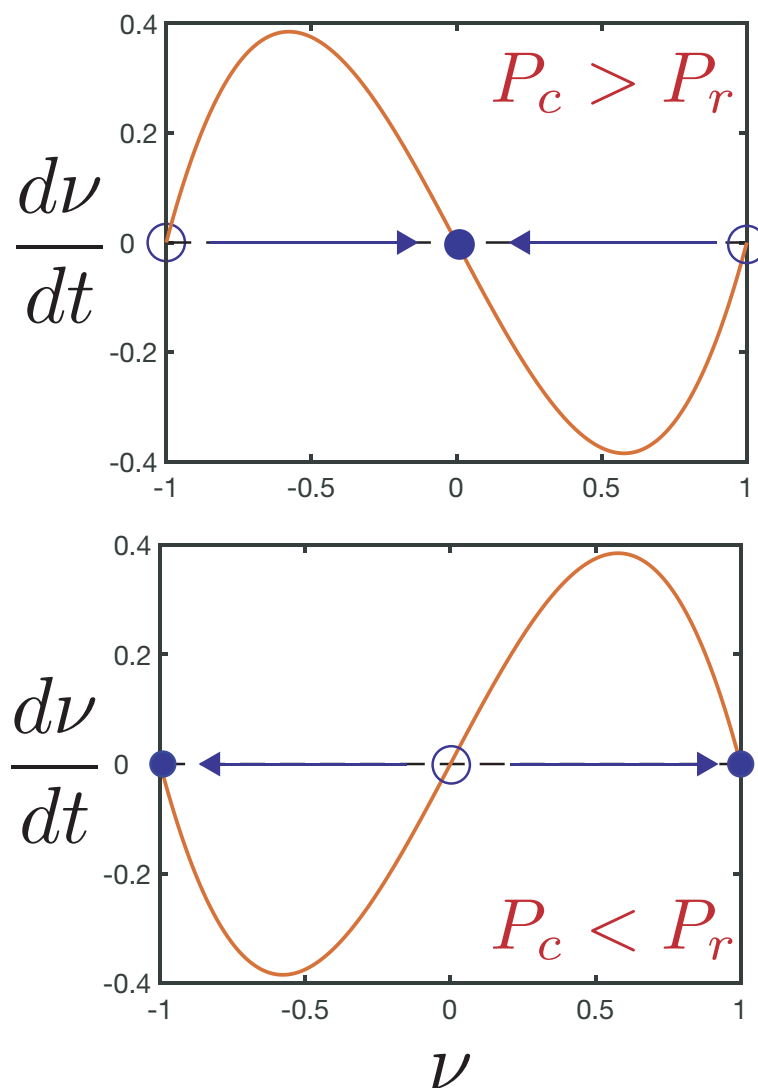


**Figure 3.12:** Rate of change of relative volume difference ( $\nu$ ) is shown as function of  $\nu$ . Solid circles indicate stable steady-states while empty ones correspond to unstable ones. For  $P_c > P_r$  the symmetric steady-state  $\nu = 0$  is stable and for  $P_c < P_r$  the asymmetric states  $\nu \pm 1$  are stable.

One can evaluate the kinetics of symmetry breaking restorations more methodically by introducing large perturbations numerically and simply solving Eq.3.52 for various initial conditions of  $\nu$ .

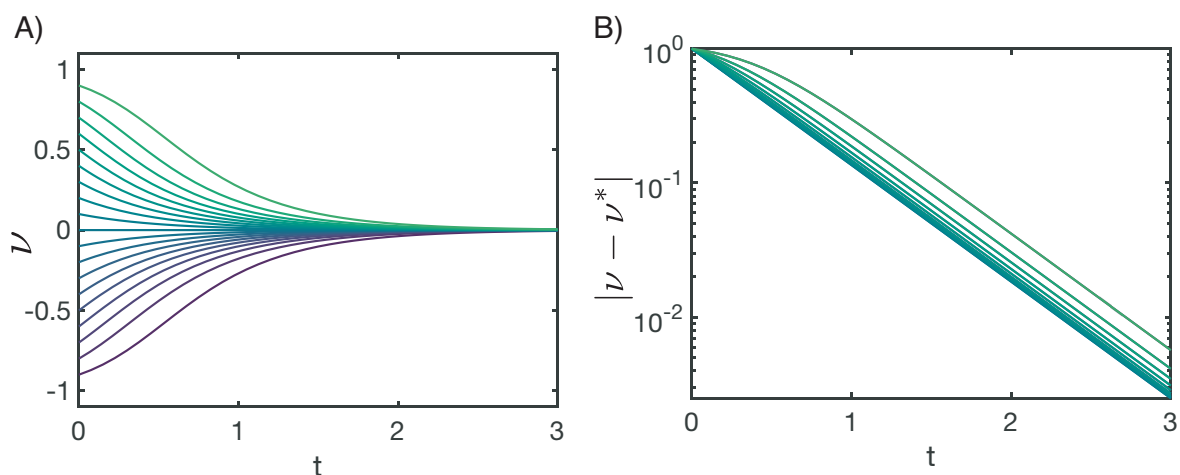


**Figure 3.13:** A) For various initial conditions  $\nu$  decays to 0 and restore symmetry when  $P_c > P_r$ . B) Semilogarithmic plot of A), emphasizing exponential decay as  $\nu \rightarrow 0$

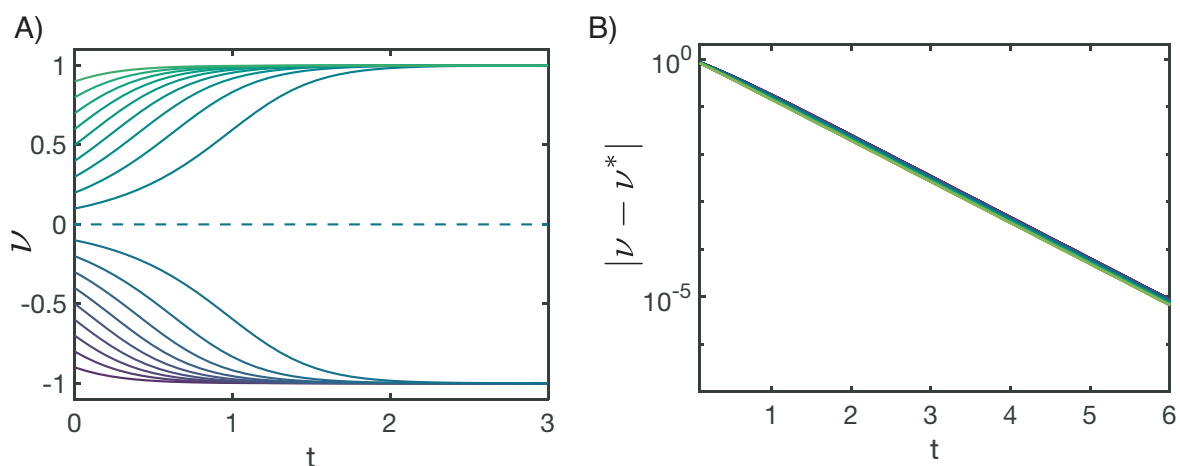


**Figure 3.14:** A) For various initial conditions  $\nu$  grows to the nearest broken-symmetry state  $\nu = \pm 1$  when  $P_c < P_r$ . B) Semilogarithmic plot of A), emphasizing exponential convergence as  $\nu \rightarrow \pm 1$

This stability can also be discussed in terms of identifying the minima of a potential function

$$W(\nu) = -\frac{\alpha_0(P_c - P_r)}{2A_c} \left( \frac{\nu^4}{4} - \frac{\nu^2}{2} \right) , \quad (3.56)$$

for which

$$\frac{d\nu}{dt} = -\frac{dW}{d\nu} . \quad (3.57)$$

This potential has a familiar structure to the Landau-Ginzburg potential.

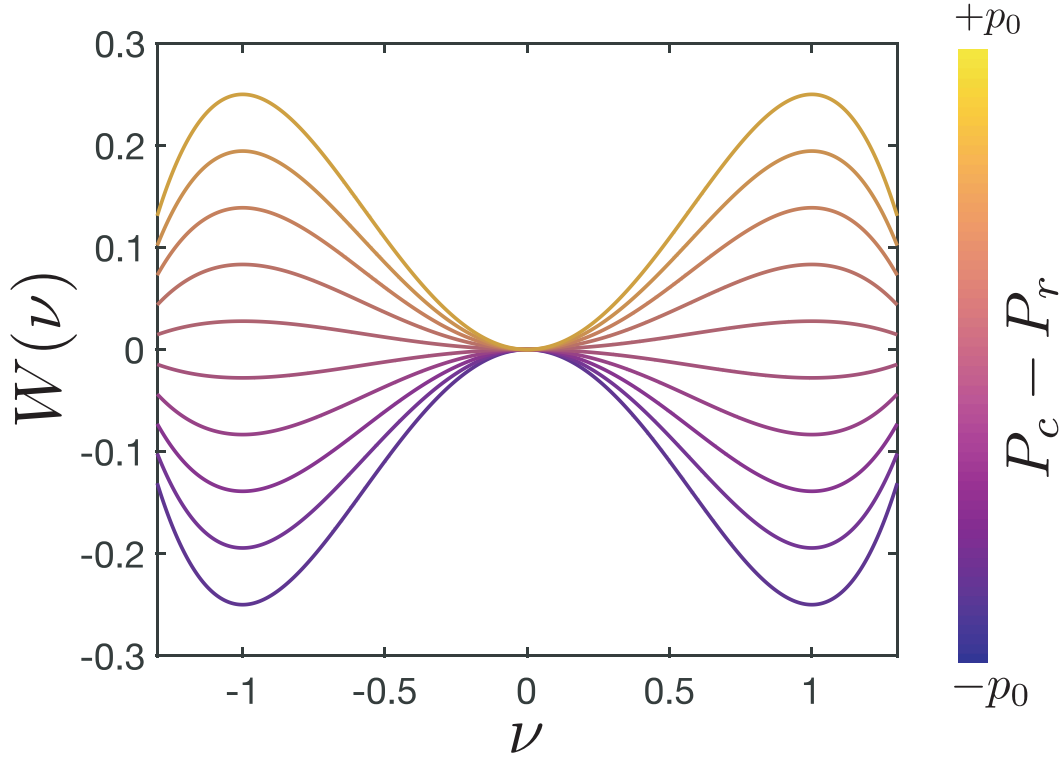


**Figure 3.15:** Pseudopotential is shown for various values of pressure-difference  $P_c - P_r$ . The extrema of the potential change curvature upon changes of pressure difference  $P_c - P_r$ .

### Generalized case:

We further evaluate the generalized case where the radius of the rachis bridges have a minimum size, which effectively introduces an offset in the proposed relationship of  $r_i$  and  $\theta_i$ . This can be represented as,

$$r_i = r_0 \left( \frac{\theta}{2\pi} + b \right) \quad (3.58)$$

Under this generalization the expression for the phenomenological coefficient  $\alpha_i$  modifies to,

$$\alpha_i = \alpha_0 \left( \frac{\theta_i}{2\pi} + b \right)^3 \quad (3.59)$$

This implies that,

$$\alpha_1 = \alpha_0 \left( \frac{1 + \nu}{2} + b \right)^3 \quad (3.60)$$

$$\alpha_2 = \alpha_0 \left( \frac{1 - \nu}{2} + b \right)^3 \quad (3.61)$$

$$(3.62)$$

Inserting these expression in Eq.3.52 and rearranging we obtain,

$$\frac{d\nu}{dt} = -\frac{\alpha_0(P_c - P_r)}{A_c} \left[ \left( \frac{1}{2} + \frac{3}{2}b \right) \nu^3 + 2 \left( b^3 - \frac{3}{4}b - \frac{1}{4} \right) \nu \right] \quad (3.63)$$

$$= -\frac{\alpha_0(P_c - P_r)}{A_c} \left[ \left( \frac{1}{2} + \frac{3}{2}b \right) \nu^2 + 2 \left( b^3 - \frac{3}{4}b - \frac{1}{4} \right) \right] \nu \quad (3.64)$$

The fixed points of this equation lie at,

$$\nu^* = 0 \quad , \quad \pm \left( 1 - \frac{4b^3}{1+3b} \right)^{\frac{1}{2}} . \quad (3.65)$$

Note that only symmetry-broken states are influenced by the offset and for  $b = 0$  we recover the original result.

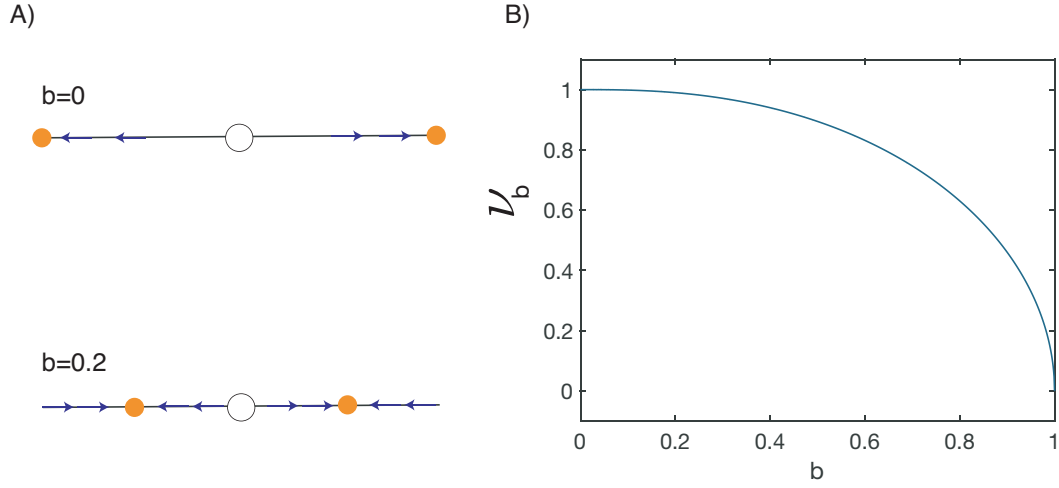


**Figure 3.16:** A) Position of symmetry broken state changes with  $b$ , B) Position of the non-trivial fixed points is shows as a function of offset  $b$ . For high values of  $b$ , non-trivial fixed points approach the trivial fixed point  $\nu = 0$ .

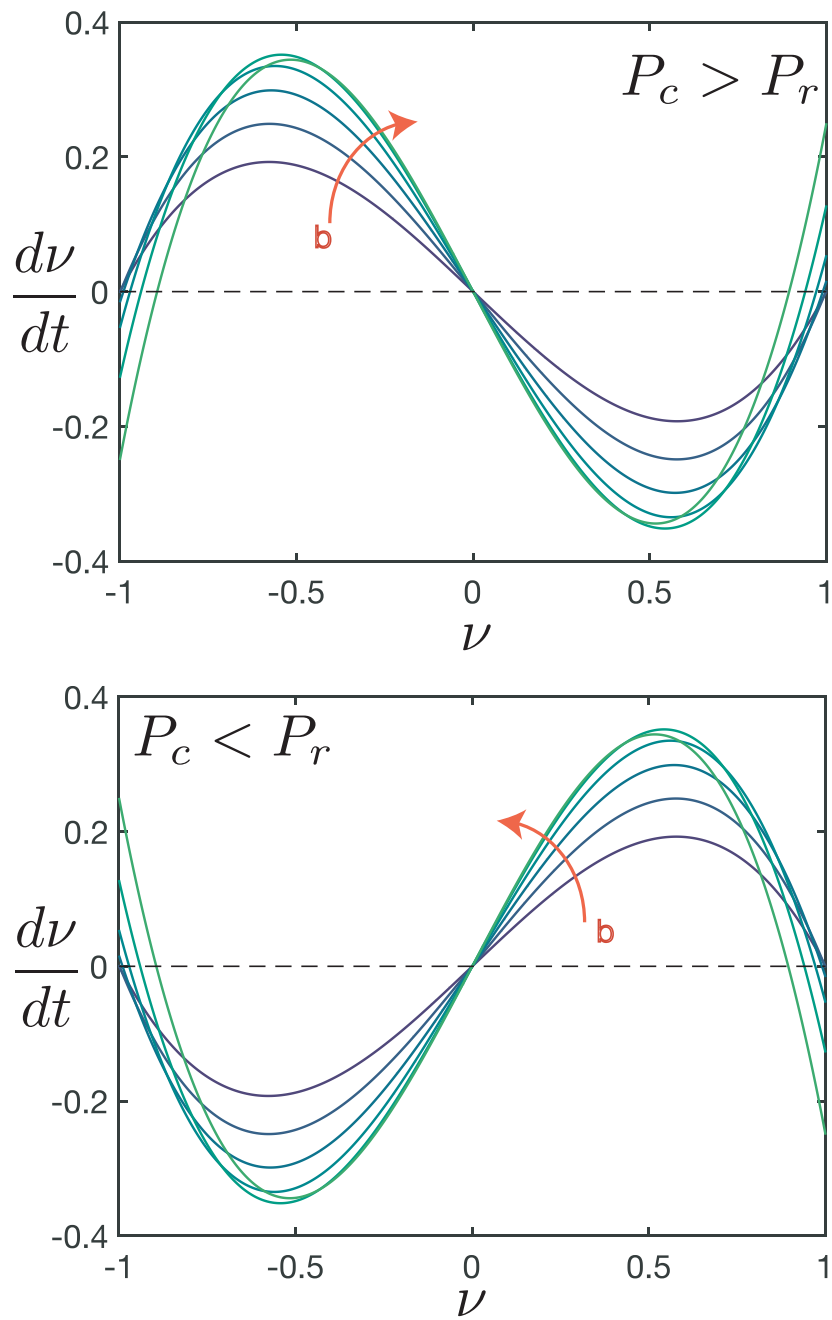


**Figure 3.17:** Rate of change of relative volume difference( $\nu$ ) is shown as function of  $\nu$  for various values of  $b$ , orange arrow indicates increasing  $b$ . Top: $P_c > P_r$ ,bottom: $P_c < P_r$

### 3.2.3 Axial stability of germ cells

In this section we will discuss the stability of germ cells in the axial direction. It is note that the azimuthal stability of the germ cell doublet does not depend on  $l_c$ , however the converse is not true. As a result as the azimuthal symmetry is broken, it may influence stability axially as well. Equation of motion for  $l_c$  is given by,

$$\frac{dl_c}{dt} = \left( \frac{S_0}{A_c} - \frac{\alpha_0(P_c - P_r)}{A_c}(\nu^3 + (1 - \nu)^3) \right) l_c \quad (3.66)$$

We find that there is no unique fixed point hence we must define a reference point to evaluate stability. If the homeostatic linear density of cells is given by  $n_0$ , then we choose the reference point  $l_c^* = 1/n_0$ . Redefining  $l_c = l_c^* + \delta l_c$ ,  $\tilde{s}_0 = S_0/A_c$  and  $\tilde{p} = \alpha_0(P_c - P_r)/A_c$  we find,

$$\frac{d}{dt}\delta l_c = \left( \tilde{s}_0 - \tilde{p}(\nu^3 + (1 - \nu)^3) \right) \delta l_c \quad (3.67)$$

which evaluated at different fixed point sof  $\nu$  yield,

$$\left. \frac{d}{dt}\delta l_c \right|_{\nu=0,+1} = (\tilde{s}_0 - \tilde{p}) \delta l_c \quad \& \quad \left. \frac{d}{dt}\delta l_c \right|_{\nu=-1} = (\tilde{s}_0 - 7\tilde{p}) \delta l_c \quad (3.68)$$

Both  $\tilde{s}_0, \tilde{p}$  are essentially time-scales and the relative balance of the two determines the stability of  $\delta l_c$ . It is interesting to note that the growth rates are identical around  $\nu = 0, +1$  however disparate from  $\nu = -1$ . We explore the phase-space of  $(\nu, \delta l_c)$  as a function of  $\tilde{s}_0$  &  $\tilde{p}$ . Note that here we only discuss the simplified case in which a constant hydraulic conductivity  $\alpha_0$  is maintained. This approximation only holds in the vicinity of  $l_c^*$ . Since  $\alpha_0 = r_0^3/(3\eta l_c) \simeq r_0^3/(3\eta l_c^*)(1 - \delta l_c/l_c^*)$ , this correction does not affect the stability analysis in linear order. Generically  $\alpha_0$  as well as  $(P_c - P_r)$  are dependent on  $l_c$ . For a discussion please see Supplementary note of [1].

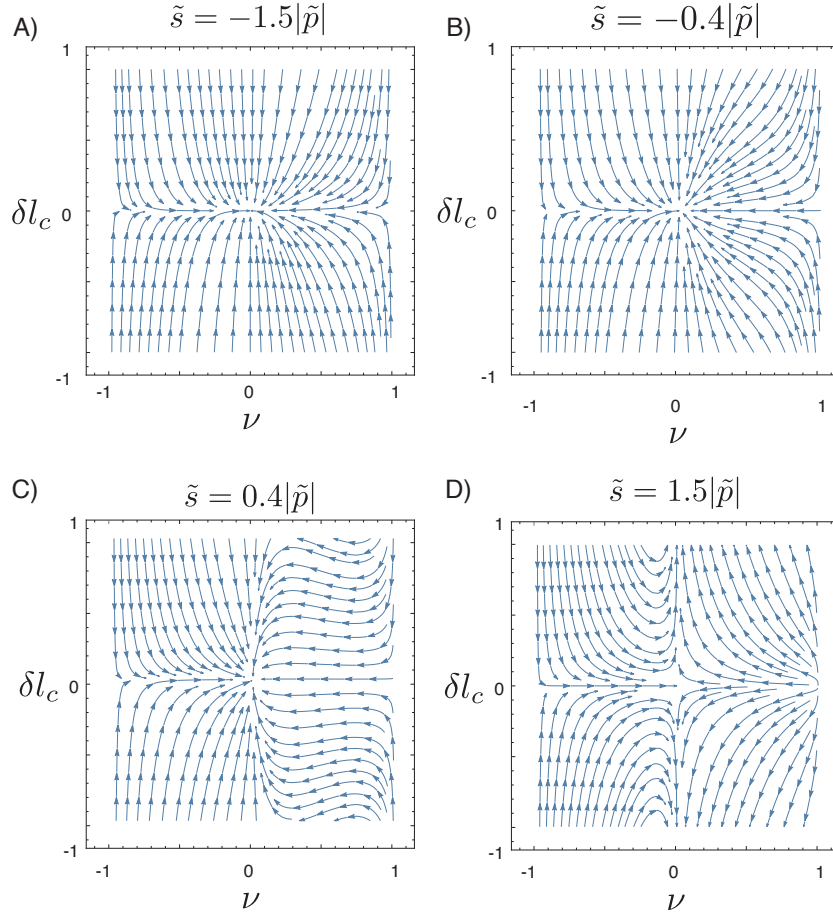


**Figure 3.18:** Phase portrait is shown for various values of  $\tilde{s}_0$  for  $\tilde{p} > 0$ . (A-C) shows a stable fixed point at  $(0,0)$  and saddle points at  $(\pm 1,0)$  D)  $(0,0)$  is also a saddle point.

For  $P_c > P_r$ : We find that the symmetric configuration ( $\nu = 0$ ) is stable axially as long as  $\tilde{s}_0 \leq \tilde{p}$ , beyond which both cells of the doublet axially grow with same rates, hence maintaining their homogeneity.

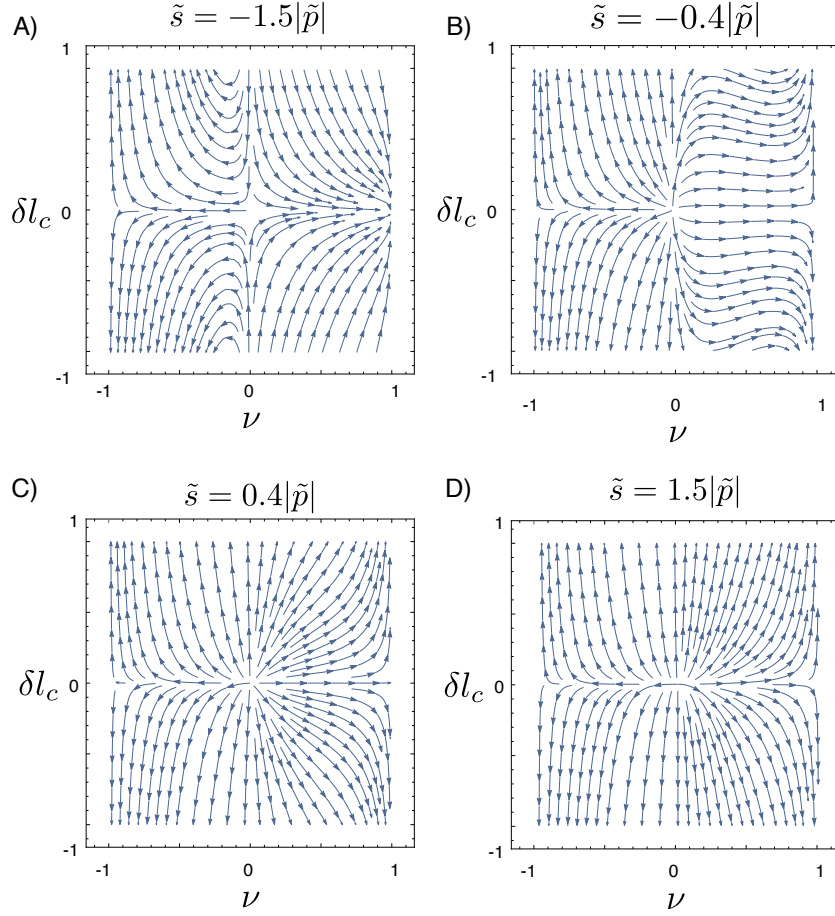


**Figure 3.19:** Phase portrait is shown for various values of  $\tilde{s}_0$  for  $\tilde{p} < 0$ . (A) shows a stable fixed point at  $(1,0)$  and saddle points at  $(-1,0), (0,0)$  (B-D)  $(\pm 1,0)$  are saddle points and  $(0,0)$  is a source.

For  $P_c < P_r$ : We find no stable state in the intermediate values of source. When the leakage dominates in the regime  $7\tilde{p} < \tilde{s}_0 < \tilde{p} < 0$ , only the  $\nu = +1$  state is axially stable and when  $\tilde{s}_0 < 7\tilde{p} < 0$  both asymmetric states are axially stable.



### 3.3 Hydraulic symmetry breaking and theory of oogenic growth

We find that upon inversion of the pressure difference  $P_c - P_r$  the current from germ cell to rachis switches sign and as a result germ cell are inflated. We derived a framework that investigates the stability of a germ cell doublet considering geometric arguments. We find such pressure inversion indeed can trigger a change of stability between states and upon inflation the symmetric configuration of the germ cell doublet becomes unstable and small variation of volumes amplify leading to a complete asymmetric state.

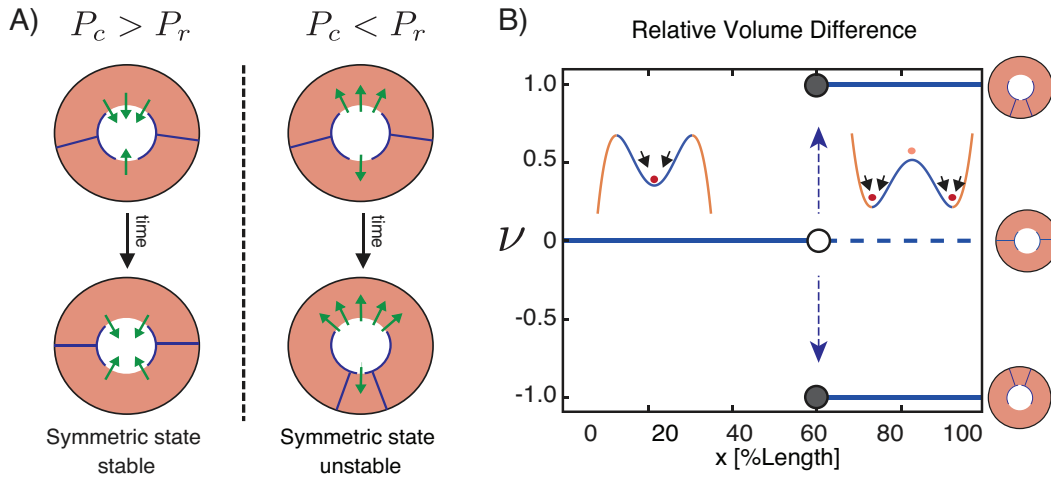


**Figure 3.20:** Proposed mechanism of spontaneous symmetry breaking in the germline upon pressure inversion. A) Schematic representation of the mechanism is depicted. B) Bifurcation diagram for symmetry variable  $\nu$  depicted spatially as a parametric function of current  $J$ .

This mechanism confirms the conjecture of chapter 2, where we raise the possibility that the transition of tissue hydraulics may underlie the growth-shrinkage symmetry breaking within the syncytia. This theoretical idea makes certain simple predictions. To test if indeed the transition of tissue hydraulics and henceforth the associated hydraulic instability indeed underlies the eventual matter of life and death for a germ cell, we inhibited the chemical pathway responsible for apoptosis in the germline. In this case, no germ cell are expected to be extruded/eliminated from germline and should exit proximally. However, hydraulic instability triggered by pressure inversion should persist despite this biochemical manipulation and should lead to same transition of volume heterogeneity. Moreover it is predicted that the inversion of  $J$  and hence the maxima of  $Q_r$  shall precede this onset of this volume heterogeneity.

To extend our analysis of tissue hydraulics of the unaltered germline to the non-apoptotic case, we postulate that the source current profile is modified due to the lack of extrusion/leakage and is given by  $S_n(x)$ ,

$$S_n(x) = \begin{cases} S(x), & \text{if } S(x) > 0 \\ 0, & \text{otherwise} \end{cases} \quad (3.69)$$

where  $S(x)$  is the experimentally inferred source current profile for unaltered germlines Fig.2.25. Using the best fit parameters  $\beta_c, \beta_r$  obtained for the unaltered germline (Fig.??) along with the leakage-less source profile  $S_n(x)$ , we predict the rachis volume flux  $Q_r$  and compare with experimental data (Fig.??).

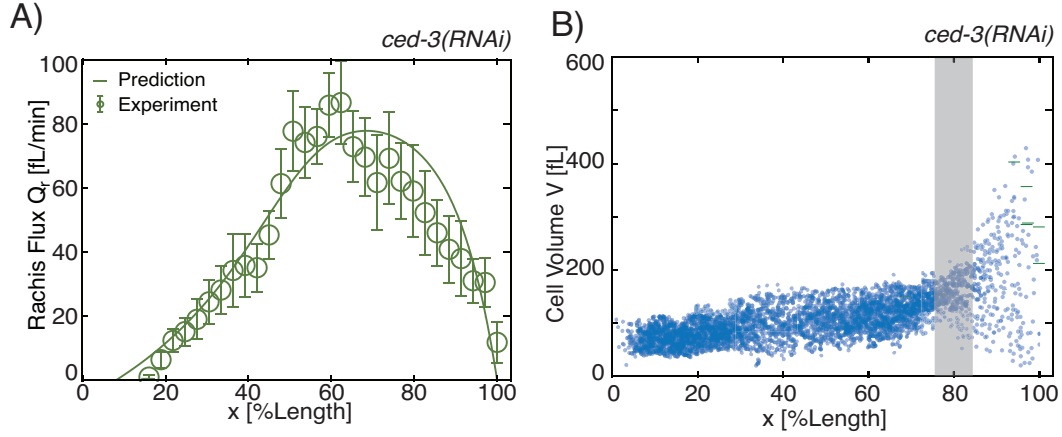


**Figure 3.21:** A) Rachis flux  $Q_r$  is presented for non-apoptotic germline treated with  $ced-3(RNAi)$ . Solid line indicates theoretical prediction. B) Germ cell volumes are presented along the DP position for non-apoptotic germlines. Shaded region indicate region of volume instability evaluated using metrics described in chapter 2.

As predicted we find that the volume heterogeneity persists even in the absence of apoptosis and extrusion and onset of the statistical instability is preceded by peak of the rachis flux  $Q_r$ .

Similar phenomena of oocyte growth has also been reported to depend on pressure driven flows within the *Drosophila* germline cyst [81]. All though fundamental similarities remain in terms of emergent altruistic behavior in both systems, the geometry of the *Drosophila* germline cyst is a network 16 germ cells connected via small ring canals and shows distinct mechanics.

### 3.4 Cooperation, conflict and altruism

In this section, we extend the analysis of the azimuthal mechanical stability from a germ-cell doublet to a radially distributed cellular collective of  $N$  cells. Extending the framework described above, we discuss questions of how a physical instability mediates a cooperative/competitive transition within a connected cell population and effectively gives rise to altruistic behavior. The dynamics of these cells are limited by the following constraint  $\sum_k \theta_k = 2\pi$  which translates to,

$$\sum_k \frac{dV_k}{dt} = A_c \frac{dl_c}{dt} = S_0 l_c - \left( \sum_k \alpha_k \right) l_c (P_c - P_r) \quad . \quad (3.70)$$

The individual cell volumes obey,

$$\frac{dV_i}{dt} = A_c \frac{\theta_i}{2\pi} \frac{dl_c}{dt} + l_c A_c \frac{1}{2\pi} \frac{d\theta_i}{dt} \quad (3.71)$$

$$= S_0 l_c \frac{\theta_i}{2\pi} - l_c (P_c - P_r) \alpha_i \quad (3.72)$$

For convenience we define  $\phi_i = \theta_i/2\pi, \in [0, 1]$ , which is the angular fraction made by the  $i^{th}$  cell, which is also the volume fraction. Combining Eq.[3.70-3.71] we obtain for  $\phi_i$ ,

$$\frac{d\phi_i}{dt} = -\frac{P_c - P_r}{A_c} \left( \alpha_i - \phi_i \sum_j \alpha_j \right) \quad (3.73)$$

Inserting the relationship  $\alpha_i = \alpha_0 \phi_i^3$  into Eq.[3.73] we obtain,

$$\frac{d\phi_i}{dt} = -\alpha_0 \frac{P_c - P_r}{A_c} \left( \phi_i^3 - \phi_i \sum_j \phi_j^3 \right) \quad . \quad (3.74)$$

Note that since  $\sum \phi_k = 1$ , the mean value of  $\phi = N^{-1}$ . In the homogeneous state  $\phi_k = N^{-1} \forall k$ , we shall investigate the stability criteria of the homogeneous state. Extending our concept of stability inversion upon pressure inversion we investigate numerically the case of positive and negative  $P_c - P_r$ . For this we define  $\epsilon_p = \text{Sign}(P_c - P_r)$ .

Case  $\epsilon_p = +ve$ :

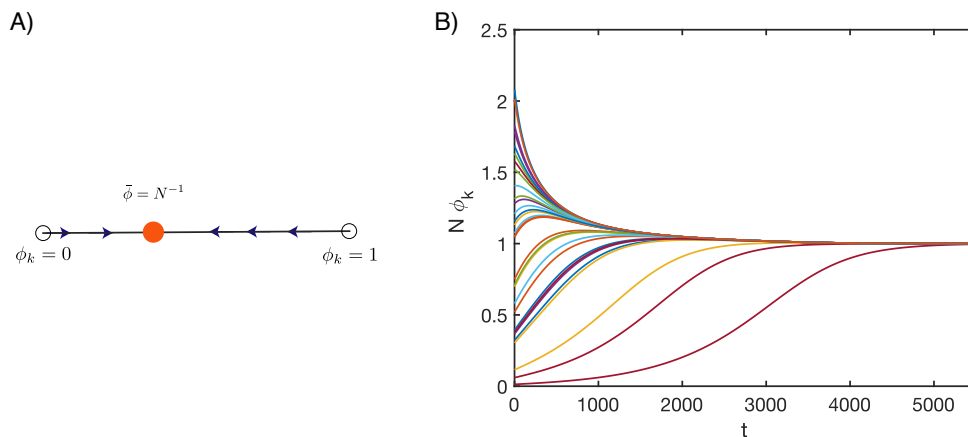


**Figure 3.22:** A) Stability diagram of homogeneous state. B) Initial variations of  $\phi$  decay and approach stable homogeneous state. ( $N=30$ )

We find that similar to the cell-doublet when  $P_c > P_r$ , the homogeneous state is stable and any deviation around it decays monotonically.

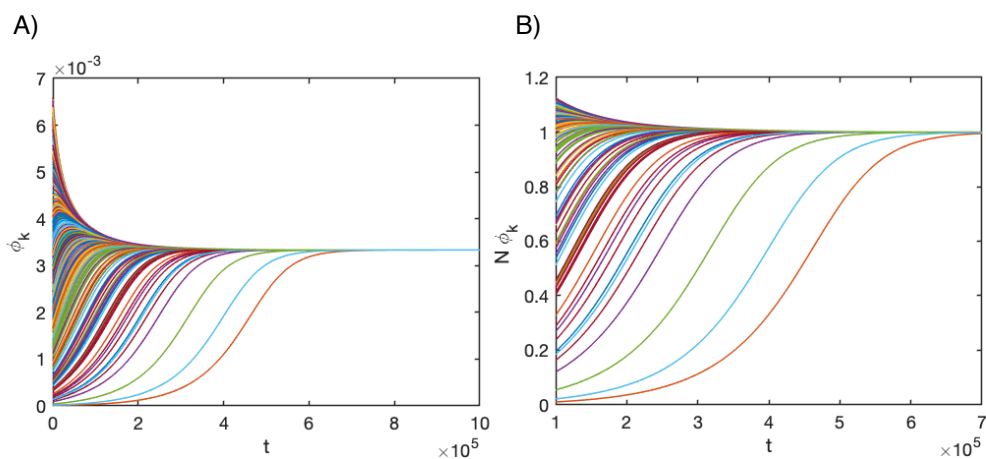


**Figure 3.23:** Stability of the homogeneous state is evaluated for  $N=300$ .

Case  $\epsilon_p = -ve$ :

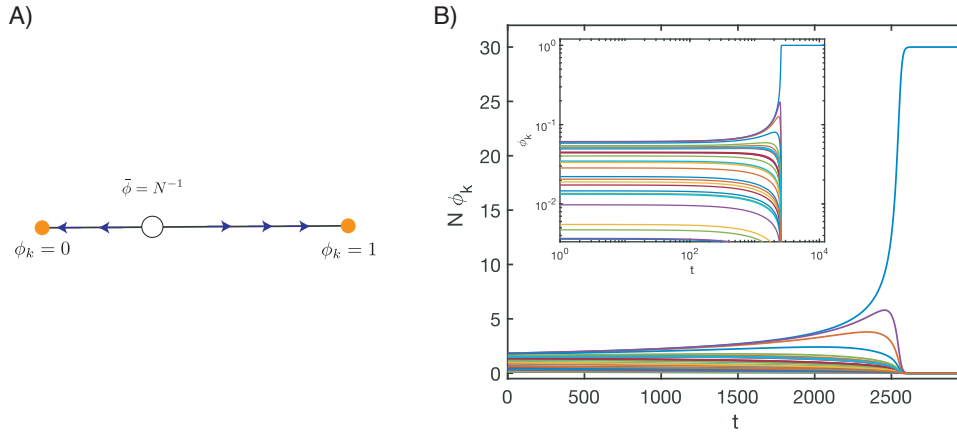


**Figure 3.24:** A) Stability diagram of homogeneous state. B) Initial variations of  $\phi$  diverge and homogeneous state is unstable. One cell grows to  $\phi = 1$ , while all other cells decay to  $\phi = 0$ . Inset: logarithmic scale is shown. ( $N=30$ )

We find that similar to the cell-doublet when  $P_c < P_r$ , the homogeneous state is unstable and small variations diverge proportionally. At long timescale all but one cell has  $\phi_k = 0$  and the "condensate" cell encompasses the entire angular fraction as well the volume. This can be thought of as a coarsening phenomena.

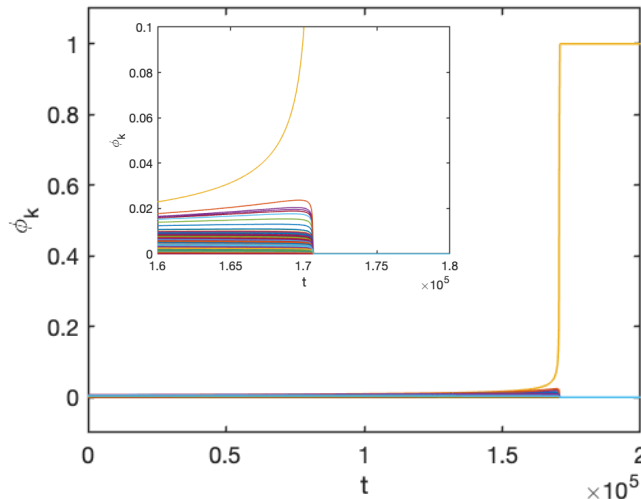


**Figure 3.25:** Stability of the homogeneous state is evaluated for  $N=300$ . Again revealing a coarsening phenomena.

This extends our analysis of the hydraulic instability and the related volume coars-

ening to a multicellular system. It shares certain commonalities with scenarios of evolutionary dynamics(continuum game theory) where total resources are constrained and species compete with each-other and underlying dynamics dictate emergence of cooperation/survival of all or competition/survival of the fittest. In the rest of this section, we shall take this analogy further and investigate a potential connection between these approaches. We start with,

$$\frac{d\phi_i}{dt} = -\alpha_0 \frac{P_c - P_r}{A_c} \left( \phi_i^3 - \phi_i \sum_j \phi_j^3 \right) \quad (3.75)$$

$$= -\alpha_0 \frac{P_c - P_r}{A_c} \left( \phi_i^2 - \sum_j \phi_j^3 \right) \phi_i \quad (3.76)$$

We now define a fitness function for the  $i^{th}$  cell to be,

$$f_i = \alpha_0 \frac{|P_c - P_r|}{A_c} \phi_i^2 \quad (3.77)$$

Representing Eq.[3.76] in terms of  $f_i$  yields,

$$\frac{d\phi_i}{dt} = -\epsilon_p \left( \alpha_0 \frac{|P_c - P_r|}{A_c} \phi_i^2 - \sum_j \alpha_0 \frac{|P_c - P_r|}{A_c} \phi_j^2 \phi_j \right) \phi_i \quad (3.78)$$

$$= -\epsilon_p \left( f_i - \sum_j f_j \phi_j \right) \phi_i \quad (3.79)$$

$$= -\epsilon_p (f_i - \bar{f}) \phi_i \quad (3.80)$$

where we have considered linear statistics and defined  $\bar{f} = \sum_k f_k \phi_k$ . Here  $\epsilon_p = (P_c - P_r)/|P_c - P_r| \in \{-ve, +ve\}$  denotes the sign of the pressure difference between cell and rachis/reservoir and hence determines the direction of cytoplasmic flow between germ cell and rachis. Eq.[3.80] has the classic form of a replicator equation [82, 83] with a sign prefactor of  $\epsilon_p$ . For  $\epsilon_p = -1$  we recover the famous equation for Darwinian selection where cells grow ( $\epsilon_p = -ve$ ) or shrink ( $\epsilon_p = +ve$ ) as the corresponding fitness function deviates from the average fitness given by  $\bar{f}$ .

This is essentially an optimization problem of  $\bar{f}$  and we can derive the equation of motion of  $\bar{f}$  in terms of  $\phi_k(t)$ ,

$$\frac{d\bar{f}}{dt} = \frac{d}{dt} \left( \sum_k f_k \phi_k \right) \quad (3.81)$$

$$= \sum_k \left( f_k \frac{d\phi_k}{dt} + \phi_k \frac{df_k}{d\phi_k} \frac{d\phi_k}{dt} \right) \quad (3.82)$$

$$= \sum_k \left( f_k \frac{d\phi_k}{dt} + 2\phi_k \frac{f_k}{\phi_k} \frac{d\phi_k}{dt} \right) \quad (3.83)$$

$$= \sum_k 3f_k \frac{d\phi_k}{dt} \quad (3.84)$$

$$= -3\epsilon_p \sum_k f_k (f_k - \bar{f}) \phi_k \quad (3.85)$$

$$= -3\epsilon_p \left( \sum_k f_k^2 \phi_k - \bar{f} \sum_k f_k \phi_k \right) \quad (3.86)$$

$$= -3\epsilon_p \sigma_f^2 \quad (3.87)$$

where using linear statistics we define  $\sigma_f^2 = \sum_k f_k^2 \phi_k - \bar{f}^2$  as the variance of the fitness  $f$ . Due to Jensen's inequality  $\sigma_f^2 \geq 0$ , indicating when  $\epsilon_p = -ve$ , the average fitness  $\bar{f}$  decreases monotonically and when  $\epsilon_p = +ve$   $\bar{f}$  increases monotonically. For  $\epsilon_p = -ve$  it is equivalent to the Fisher's fundamental theorem of natural selection [82, 83], with an additional prefactor of 3.

In specific to study how relative proportions of two cells may evolve over time we can derive,

$$\frac{d}{dt} \left( \frac{\phi_j}{\phi_k} \right) = \frac{1}{\phi_k} \frac{d\phi_j}{dt} - \left( \frac{\phi_j}{\phi_k} \right) \frac{1}{\phi_k} \frac{d\phi_k}{dt} \quad (3.88)$$

$$= -\epsilon_p \left( \frac{\phi_j}{\phi_k} (f_j - \bar{f}) - \frac{\phi_j}{\phi_k} (f_j - \bar{f}) \right) \quad (3.89)$$

$$= -\epsilon_p \frac{\phi_j}{\phi_k} (f_j - f_k) \quad (3.90)$$

indicating that growth of relative ratios is purely a function of difference in fitness, a result akin to evolutionary dynamics of competing species.

This constitutes an elegant mapping between hydrodynamics and evolutionary dynamics. To elucidate the physical consequences let us evaluate and interpret the hydraulic fitness function  $f_k$ ,

$$f_k = \frac{|\alpha_0(P_c - P_r)|}{A_c} \phi_k^2 = \left| \frac{\alpha_0(P_c - P_r) \phi_k^3 l_c}{A_c \phi_k l_c} \right| = \left| \frac{J_k l_c}{V_k} \right| \quad (3.91)$$

where we multiply the numerator and denominator with  $\phi_k l_c$  and identify  $\alpha_0(P_c - P_r) \phi_k^3 = J_k$  and  $A_c \phi_k l_c = V_k$ . In resource limited conditions i.e. in the absence of the source current the entire rate of change of volume is determined by the current  $J$  and

hence we find,

$$f_k = \left| \frac{1}{V_k} \frac{dV_k}{dt} \right| \sim \frac{1}{\tau} \left| \frac{\Delta V_k}{V_k} \right| \quad (3.92)$$

and is interpreted as the relative growth/shrinkage rate. Since both growth and shrinkage would imply the same result here, it can be interpreted as an adaptive sensor in line with concepts of control theory and controls relative changes to the volume. Furthermore this alludes to the idea that out of the population of cells the fittest (maximum  $f_k$ ) is neither the largest nor the fastest growing but rather the most "adaptive".

In a more general case the volume exchange could be driven by mechanisms other than pressure driven flows, such as diffusive, osmotic etc. We briefly discuss the generality of this result in such context. The majority of the calculation remains the same and we discuss the general case of  $\alpha \sim r^\beta$  and obtain,

$$\frac{d\phi_i}{dt} = -\alpha_0 \frac{P_c - P_r}{A_c} \left( \phi_i^\beta - \phi_i \sum_j \phi_j^\beta \right) \quad (3.93)$$

where the generalized fitness term  $f_k = |\alpha_0(P_c - P_r)|\phi_k^{\beta-1}/A_c$ . Retracing the steps of Eq.3.81-87, we find for equation for the average fitness  $\bar{f}$ ,

$$\frac{d\bar{f}}{dt} = -\beta \epsilon_p \sigma_f^2 \quad (3.94)$$

where we can only obtain these solutions for  $\beta > 1$ , otherwise the assertions of Eq.3.83 breaks down. We provide brief overview of the general results in a schematic form below. We find that the general questions of structural stability as well as conclusions regarding cooperative/competitive state remains unchanged for exponent  $\beta > 1$ , while lower exponents are possible for passive and active transport through channels that maintain constant surface density.

Exponent	$P_c > P_r$	$P_c < P_r$	Example / Interpretation
$\beta = 3$	Stable	Unstable	Sampson flow through pores
$\beta = 2$	Stable	Unstable	Mechanosensitive channels
$\beta = 1$	Marginal	Marginal	Active/Passive transport via pumps of constant density



## 3.5 Conclusion

Motivated by experimental result, in this chapter we develop a hydraulic theory of the germline at rest. This theory elucidates on the development of steady flow fields across the germline, development of pressure field as well as their inversion spatially. Using only 2 parameters, this minimal theory captures experimental result and makes predictions with great accuracy. We derived a novel framework of stability of the germline that revealed a tissue hydraulics induced spontaneous symmetry breaking and also informed us of the necessary criteria for the stability of the symmetric state. We tested rudimentary predictions of the theory experimentally with excellent agreement, providing a novel conceptual advance on growth and shrinkage of germ cells as symmetry breaking. This provides a quintessential example of mechanics and hydrodynamics underlying a fundamental decision making in biology.

We extended the framework of symmetry breaking originally derived from hydrodynamic considerations to a multicellular system to ask questions of stability. We found again a hydraulics induced coarsening phenomena. Starting from this model we found an elegant derivation to game theory/evolutionary dynamics and developed ideas of hydraulic fitness as an adaptive volume sensor and recovered conditions of cooperative/ competitive transition. Here the effective equations of evolutionary dynamics are not heuristic but rather emergent as they are derived from first principles of volume conservation and hydrodynamic theory.

This weaves various concepts from different disciplines together, starting from biological fluids, tissue mechanics, game theory/evolutionary dynamics and presents a unique interdisciplinary perspective to understand the growth and selection of a particular cell over others in a seemingly homogeneous and hydrodynamically connected multicellular structures. These concepts developed here are indeed much more general and should apply to various geometries and conditions.

# Chapter 4

## Summary

*Nothing in biology makes sense except in the light of evolution.*  
- Theodosius Dobzhansky

In this thesis, we strive to address a fundamental question of biology with concepts and tools of physics. We started out with posing the question of life and death as a cellular decision in the life of a germ cell, a decision that is fundamental to the fate of progeny and hence to all of morphogenesis. We identified that this general mystery persists across species in various geometries and time-scales. Using a physical reductionist approach we identified that this decision making essentially is a transition of growth and shrinkage in the life of a germ cell, a physical fate that appears in the arrow of time and creates disparity in a seemingly homogeneous population of cells that prior to this transition share their cytoplasmic pool and hence chemical identity. We take the example of germ cells of adult hermaphrodite nematode *C.elegans* to investigate this transition as well understand the basis of growth.

Using statistical models and elements of fluid dynamics, we characterize the growth and shrinkage of germ cells. We find that the germ cells grow along their maturation axis in two different phases, one that is slow and homogeneous hence regulating variation of cell sizes within the distal germ cell population, this phase is succeeded by a phase of rapid and heterogeneous growth of germ cells leading to increasing disparity of sizes within the proximal population. Concurrently we find that distal germ cells pump cytoplasm into luminal core called rachis and drive long range cytoplasmic flows, while the proximal cells take up material from this cytoplasmic stream. Albeit slow, the growth of distal germ cells despite pumping volume into the rachis led us to identify the external source that accounts for this growth and maintenance of distal germ cell volumes. This identification of the external source is based on simple principle of volume conservation and reveals a vital piece of information that was heretofore unknown. The transition of this source profile and the current from germ cell to rachis occur within close proximal vicinity of the transition between growth modes identified before. This alluded that perhaps the transition of tissue hydraulics is the underlying cause of volume instability within the distal population, much like inflation instabilities of connected soap bubbles.

To formulate this hypothesis we derived a novel framework of tissue hydraulics that successfully captures the hydrodynamic fields across the germline and informed us of

---

an inversion of pressure differences between germ cells and rachis concurrent to the inversion of the germ-cell to rachis current. We further derive a framework of mechanical stability to evaluate the effect of such pressure inversions and we identify a stability switch or a discontinuous transition between states upon this pressure inversion with a simple example of a germ-cell doublet. While in the positive pressure difference regime, as the germ cells pump into the rachis homogeneous cell volumes are stable and any deviation from this symmetric configuration decays over time and symmetry of the system is restored. On the contrary, when pressure difference inverts and germ cells are rather inflated from within, the symmetric configuration become unstable and any heterogeneity between two connected germ cells amplify nonlinearly leading to increasingly asymmetric structures eventually achieving a configuration where one cell engulf the entirety of the tissue. We identify this discontinuous transition to be a symmetric breaking phenomena modulated by a pressure field. We term this as a hydraulic instability. This growth of asymmetry has close parallel to coarsening and condensation. Based on this simple idea, we make the deduction that the growth and shrinkage transition for germ cells is driven by the tissue hydraulics and the associated insatiability. We test this proposition by eliminating the bio-chemical pathway responsible for cell death and find that even in the absence of cell elimination this transition of tissue hydraulics and the volume instability persist and the transition of tissue hydraulics precedes the onset of volume heterogeneity. This tissue hydraulics driven selection mechanism explains the stability of distal germ cells despite the inherently open structure of germ cells, provides a tested mechanism of not only selection of germ cells but also a mechanism that perpetually ensure growth and hence survival of the chosen cell. This provides a fresh outlook on this age-old problem of oogenesis and a quintessential example of mechanical instability driving a cell fate decision, a robust alternative to biochemical switches.

Building upon this elegant model of a germ cell doublet to a system of  $N$  cells we evaluate the question of stability and whether such multicellular structures can stably pump and exchange cytoplasm through their common luminal core. We find the same stability criteria for the  $N$ -dimensional systems. In the regime in which all the cells are pumping and contributing cytoplasm (hence cells have higher pressure than lumen) to the lumen is stable and homogeneous symmetric structures are restored if small deviations are introduced. On the contrary, when the pressure difference and the direction of the cytoplasmic exchange inverts, we find a similar coarsening phenomena, where volume differences around the mean amplify and eventually all the volume condenses to one cell, must like Ostwald ripening of droplets. From a naive perspective this could be viewed as a transition between cooperative and competitive behavior i.e. when the resources abundant in terms of source, cooperation is favored and under resource limitation competition and a redistribution instability emerges.

Extending this naive analogy further, we discover a mapping between our model of hydrodynamically interacting cells to a system of replicator equations and it adopts the form of Darwinian selection model when lumen pressure is higher than cell pressure. We derive the growth of the average fitness of the population and we find a modified form of the celebrated Fisher's fundamental theorem of natural selection. This mapping provides a elegant way to extend this general idea of hydraulic instability and brings

forth an evolutionary perspective on the nature of cooperation and competition of cells within syncytial structures that share and distribute resources via hydrodynamic flows. We find the physical interpretation of the fitness function to be the relative rate of growth/shrinkage, which also can be thought of as an adaptive sensor. This weaves in the idea of adaptability into this fascinating framework.

In all, we find a physical mechanism of stability and instability of a tissue driven by hydrodynamic fields that underlie the symmetry breaking of growth and shrinkage and hence the eventual decision of life and death. This brings forth novel ideas of symmetry breaking, hydrodynamics, developmental biology and evolutionary dynamics together with important consequences in the context of other syncytial structures. This provides an elegant derivation of basic equations of evolutionary dynamics from fundamental principles of hydrodynamics.

## Outlook

The realization that in the absence of a decision maker virtually all decision making processes are symmetry breaking, is a powerful conceptual advance in biology. This beautiful example of how lingering residual effects upon a physical instability can compromise the outcome at much larger lengthscales, will be foundational to questions of cellular decision making. Within the framework of this hydraulic symmetry breaking we surprisingly recover equations and concepts of evolutionary dynamics and selection, a connection embedded within the spirit of biological questions that we asked. We suspect this relationship has fundamental general consequences in the mysterious context of multicellular cooperation and paves the path for future theoretical musings into the transitions of complex multicellular collectives.

# Appendices

# Appendix A

## Germ cell nuclear growth and allometry

### A.1 Nuclear growth

A germ cell grows upto 20 folds in size along its' maturation from distal tip to proximal turn, meanwhile the nucleus of a germ cell also transitions across functional states. We find that the germ cell nuclei grow also 10 fold in volume starting from the distal end to the proximal turn.

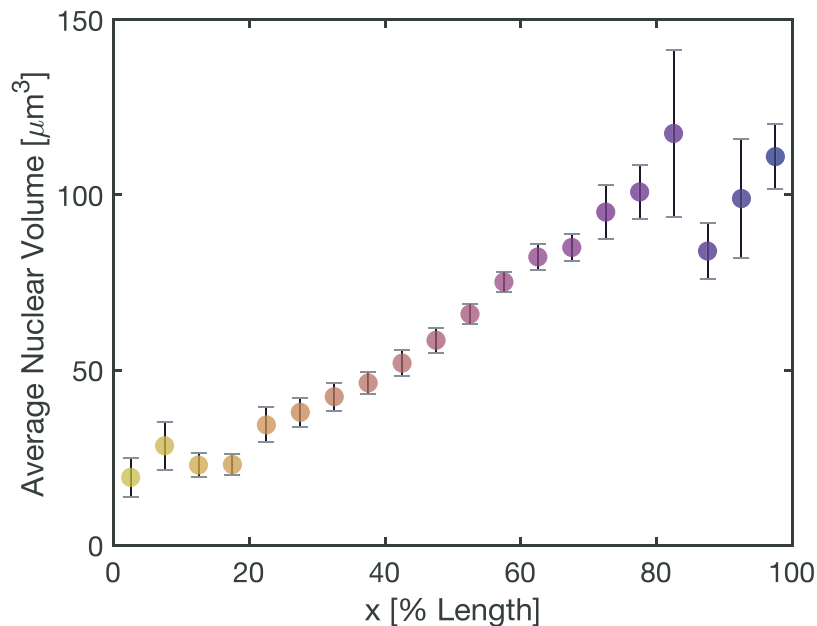


**Figure A.1:** Average nuclear volume is represented along the distal-proximal axis.

### A.2 Allometric scaling and proportional growth

Cellular organelles such as the nucleus, mitotic spindle adapt their size to the dimensions of the cell. Size regulation of cellular organelle is of fundamental importance

to biology [84–90]. Various mechanisms have been proposed to understand emergence of scaling behavior between organelle and cell size. The germline provides a unique model to investigate the question of scaling, as the cells have open boundaries and are syncytial. We correlate the average nuclear size at a given location along DP axis with average germ cell size (Fig.A.2) .

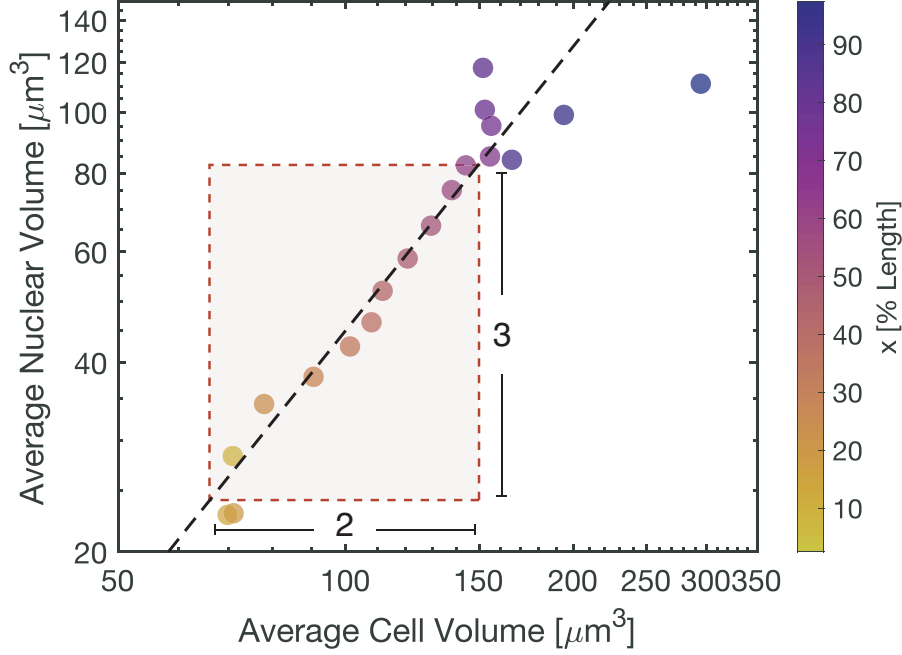


**Figure A.2:** Average nuclear size scales with average cell volume. Allometric relationship breaks down in proximal gonad. Color code indicates position along the DP axis.

We find that an allometric scaling can be deduced between nuclear size and germ cell size for majority of the germline. This relationship breaks down near the proximal end and could originate from bimodal cell volumes, hence we shall restrict the discussion up to the scaling region. We propose the following scaling relationship,

$$V_n = \left( \frac{V_c}{V_0} \right)^{1+\beta} \quad (\text{A.1})$$

where  $V_n$  &  $V_c$  are the nuclear and cell volume respectively and  $V_0$  being the offset volume.  $\beta$  is the allometric exponent that quantifies deviation from volume scaling, i.e.  $\beta = 0$  indicates perfect volume scaling,  $\beta < 0$  indicates a sub-volume scaling (e.g. surface scaling) and  $\beta > 0$  a super-volume scaling. We find using a fitting procedure,  $\beta = 0.5 \pm 0.05$  and  $V_0 = 1.7 \pm 0.01 \mu\text{m}^3$ . However within the gonad both germ cells and nuclei are growing, hence they must dynamically maintain this relationship

between  $V_c(t)$  &  $V_n(t)$  and this restricts their growth dynamics. As a result,

$$\frac{dV_n}{dt} = (1 + \beta) \frac{V_c^\beta}{V_0^{1+\beta}} \frac{dV_c}{dt} \quad (\text{A.2})$$

$$= (1 + \beta) \left( \frac{V_c}{V_0} \right)^{1+\beta} \frac{1}{V_c} \frac{dV_c}{dt} \quad (\text{A.3})$$

Inserting the expression for  $V_n(t)$  we obtain,

$$\implies \frac{1}{V_n} \frac{dV_n}{dt} = (1 + \beta) \frac{1}{V_c} \frac{dV_c}{dt} \quad (\text{A.4})$$

This constitutes the law of proportionate growth for such a scaling relationship. In future, it would be interesting to validate this temporal relationship. However there exists some simple deductions that do not require temporal information. In Chapter 2, we found that the effective growth rate of distal germ cells is fairly constant and does not depend on cell size, presumably due to growth by material uptake from surrounding. One can approximate Eq.A.4 as,

$$\frac{\delta V_n}{V_n} \simeq \tau_n (1 + \beta) \frac{g_c}{V_0} V_n^{-\frac{1}{1+\beta}} \quad (\text{A.5})$$

where  $\tau_n$  is the timescale of nuclear growth,  $g_c = \langle dV_c/dt \rangle$  is the effective growth rate of distal germ cells. This implies that with growing nuclear volume ( $V_n$ ), relative variation will decrease. We try to provide an estimate of the prefactor. We estimated  $g_c \sim 0.04 \mu\text{m}^3/\text{min}$  in chapter 2. One can assume  $\tau_n$  is limited by the nuclear cycle that ranges between 2 to 5 hrs [43]. Inserting the estimated values of  $g_c$ ,  $V_0$ ,  $\beta$  and an example value of  $\tau_n = 4\text{hr} = 240\text{min}$  into Eq.A.5 we obtain,

$$\frac{\delta V_n}{V_n} \simeq 5.5 V_n^{-2/3} \quad (\text{A.6})$$

To test this rudimentary prediction we correlate CV ( $= \sigma/\mu$ ) of nuclear size with average nuclear size and overlay the predicted curve (Fig.A.3).



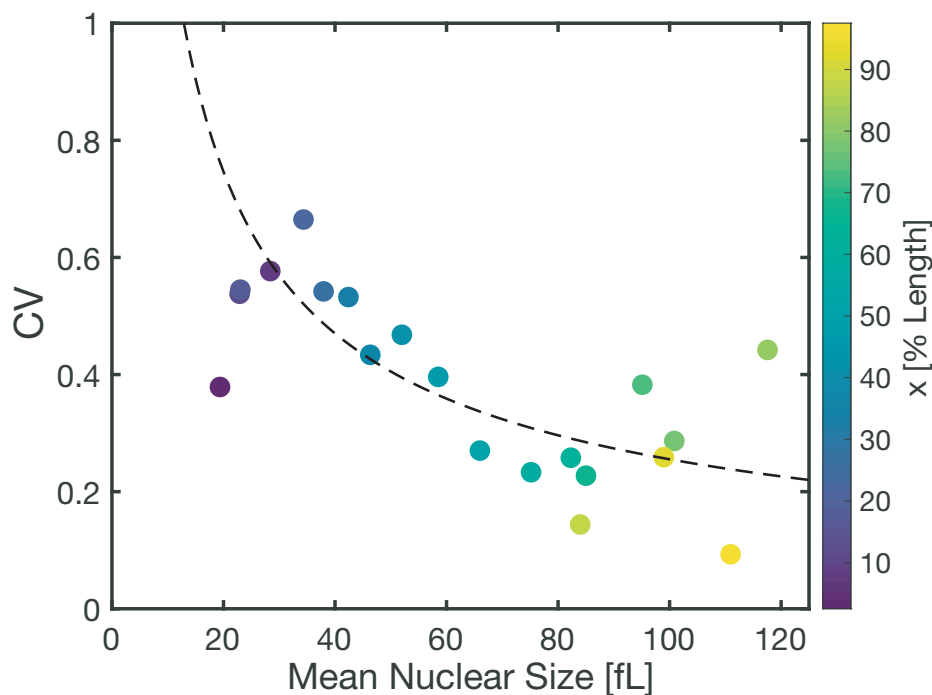


**Figure A.3:** Coefficient of variation of nuclear size is plotted against average nuclear size. Dashed line shows predicted curve Eq.A.6. Color code indicates position along the DP axis.

## A.3 Conclusion

Here we provide a brief discussion of nuclear growth in the germline. Throughout the thesis, we limit the discussion of oocyte growth solely to the volume of the cytoplasm contained. However, not only germ cells must take up volume to grow, they also must produce valuable cytoplasmic material (e.g. proteins, enzymes etc.), for this purpose the proportionate growth of organelles like nuclei, ER is essential. While mechanisms, such as "limited resource model" can account for nuclear size scaling in most cells [84], these concepts do not apply in the germline as the cells are open and access a vast reservoir of cytosolic matter. This raises fundamental questions on what physical mechanisms must underlie size scaling while exchange with an infinite pool of cytosol is present.

A fascinating finding pertains to the decreasing heterogeneity of the nuclear volumes, along the Distal Proximal axis as the average size of the nuclei grow. This is in sharp contrast to the growing heterogeneity of cell volumes along the DP axis. A plausible interpretation could be proposed in terms of a bet-hedging strategy to circumvent the slow growth of nuclei. The ideal case would be where only the nuclei of the future oocyte hence the future larger cells grow, for which it is essential to ascertain which one of the germ cells grow to oocyte – a decision we have shown to rely on an instability, hence naturally uncertain. An alternative strategy would be of the responsive kind, where the nuclear growth would rapidly adapt to the growing germ cell, however the

unstable growth of germ cells are via pressure driven cytoplasmic redistributions which are much faster than the import limited growth of nuclei. We find that the nuclear population becomes more homogeneous in size as they grow larger. This is indicative of a hedged-bet solution, showing an equivalent weights on all nuclei. The bet-hedging strategy presents a trade-off solution in this uncertain environment, much like many biological systems [91–93].

# Appendix B

## Viscous steady flow through a pipe

In this chapter we shall discuss some basic results related to viscous flow through channels and pipes. We will extend this analysis to special cases to take into account more realistic geometries and effects. These discussions will help guide certain direct results implemented in chapter 2 & 3.

We shall consider an incompressible viscous fluid. Hence in the low Reynolds number regime, the steady velocity field is prescribed as solution to the Stoke's equation,

$$\eta \nabla^2 \vec{v} = \nabla p \quad (\text{B.1})$$

where  $\vec{v}$  is the velocity,  $\eta$  the viscosity and  $p$  is the pressure field. This equation is supplemented by the condition of incompressibility,

$$\nabla \cdot \vec{v} = 0 \quad (\text{B.2})$$

This also has a simple implication that the pressure field is harmonic and is given by the Laplace's equation,

$$\nabla^2 p = \nabla \cdot \nabla p = \nabla \cdot (\eta \nabla^2 \vec{v}) = \nabla^2 (\eta \nabla \cdot \vec{v}) = 0 \quad (\text{B.3})$$

### B.1 Viscous flow through an ideal pipe

Let us consider a case of an ideal cylindrical tube of length  $l$  and duct radius  $R$ . We shall define the axis of symmetry as the  $z$ -axis and consider a cylindrical coordinate system  $(r, \phi, z)$  to respect the symmetry of the problem. We prescribe the pressures at both ends of the tube as  $p(z=0) = P_0$  and  $p(z=l) = P_l$ . Now we shall seek solutions of the velocity field  $\vec{v} = (v_r, v_\phi, v_z)$ . Due to azimuthal symmetry of the problem  $v_\phi = 0$  and since the pressure field has no gradient in the radial direction, we can limit our discussions to the flow velocity  $v_z$ .

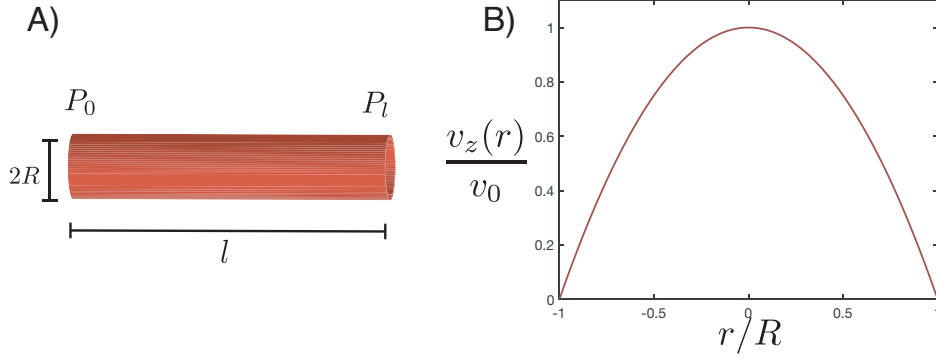


**Figure B.1:** A) Schematic of a pipe of length  $l$  and circular cross-section of radius  $R$  is shown. Inlet pressure  $P_0$  and outlet pressure  $P_l$  is indicated. B) Parabolic velocity profile of  $v_z(r)$  is shown across the normalized radial position  $r/R$ .

The Stoke's equation thus reduces to,

$$\eta \frac{1}{r} \frac{d}{dr} \left( r \frac{dv_z}{dr} \right) = \frac{dp_z}{dz} \quad (\text{B.4})$$

The pressure field is given by the solution to the Laplace's equation  $\nabla^2 p = 0$  and the boundary condition. We find that,

$$\frac{dp}{dz} = -\frac{\Delta p}{l} \quad (\text{B.5})$$

where  $\Delta p = P_l - P_0$ . The general solution to the Eq.B.4 yields,

$$v_z(r) = -\frac{1}{4\eta} \frac{\Delta p}{l} r^2 + a \ln r + b \quad (\text{B.6})$$

We impose that  $v_z(0)$  is finite, as a result the prefactor to the diverging logarithmic term  $a = 0$ . We choose the no-slip boundary condition  $v_z(R) = 0$  and obtain,

$$v_z(r) = \frac{1}{4\eta} \frac{\Delta p}{l} R^2 \left( 1 - \frac{r^2}{R^2} \right) \quad (\text{B.7})$$

This parabolic nature of the velocity profile is preserved for all pressure driven flows in channels and pipes. One can also identify that the given parabolic profile has a maxima at  $r = 0$  and is given by,

$$v_0 = \frac{1}{4\eta} \frac{\Delta p}{l} R^2 \quad (\text{B.8})$$

We can then estimate the volume flux/discharge rate,

$$Q = \int_0^{2\pi} d\phi \int_0^R v_0 \left( 1 - \frac{r^2}{R^2} \right) r dr = \pi R^2 \frac{v_0}{2} = \frac{\pi R^4}{8\eta} \frac{\Delta p}{l} \quad (\text{B.9})$$

This relationship is the well known Hagen-Poiseuille law, originally discovered ex-

perimentally by Jean Leonard Marie Poiseuille at the age of 18 [94]. One can define a hydraulic resistance  $k = Q/\Delta p$ , which here is given by  $k = \pi R^4/8\eta l$ . It is trivial to see that the average velocity  $\bar{v} = Q/\pi R^2 = v_0/2$ . The local shear rate of the flow in the circular pipe is simply  $\dot{\gamma} \simeq \bar{v}/R$  and scales with  $\sim R$ .

This result still extends to pipes with non-uniform radii along the symmetry axis. While the appropriate treatment of this problem is through the lubrication theory, we can assume the case of slowly varying radii. In that case we can ask what is the discharge rate of the tube as  $R(z)$ . A simple interpretation is that the hydraulic resistance becomes function of space. The following equation hold locally ,

$$-\frac{dp}{dz} = \frac{8\eta Q}{\pi R(z)^4} \quad (\text{B.10})$$

Integrating along the length we find,

$$\Delta p = \frac{8\eta Q}{\pi} \int_0^L R(z)^{-4} dz \quad (\text{B.11})$$

Hence the effective hydraulic conductivity is simply,

$$k_e = \frac{\pi}{\eta} \frac{1}{l} \left[ \int_0^L R(z)^{-4} dz \right]^{-1} \quad (\text{B.12})$$

If the pipe is not hollow but consists of two concentric cylinders of radii  $R_1$  &  $R_2$  where  $R_1 > R_2$ , we may still employ this analysis by applying Eq.B.6 with the boundary conditions  $v_z(R_1) = v_z(R_2) = 0$ ,

$$v_z(r) = \frac{\Delta p}{4\eta l} \left[ R_1^2 - r^2 + \frac{R_1^2 - R_2^2}{\ln(R_1/R_2)} \ln \frac{r}{R_1} \right] \quad (\text{B.13})$$

We can then compute the discharge rate,

$$Q = \frac{\pi \Delta p}{8\eta l} \left[ R_1^4 - R_2^4 + \frac{(R_1^2 - R_2^2)^2}{\ln(R_1/R_2)} \right] \quad (\text{B.14})$$

General discussions of the effect of cross-section shape on the hydraulic conductance of a pipe is an active area of research. Some variations of the circular pipe are of particular importance in the context of biological fluid dynamics. For a pipe of ellipsoidal cross-section described by  $x^2/a^2 + y^2/b^2 = 1$  with no-slip boundary conditions the velocity field is given by,

$$v_z = \frac{\Delta p a^2 b^2}{2\eta l (a^2 + b^2)} \left( 1 - \frac{x^2}{a^2} - \frac{y^2}{b^2} \right) \quad (\text{B.15})$$

and the discharge is,

$$Q = \frac{\pi \Delta p}{4\eta l} \frac{a^3 b^3}{a^2 + b^2} \quad (\text{B.16})$$

In comparison to the discharge of a circular pipe ( $Q_o$ ) with same cross-sectional area,

$$\frac{Q}{Q_o} = \frac{2\epsilon}{1 + \epsilon} \quad (\text{B.17})$$

where  $\epsilon = b/a$  is the ellipticity. One can see that this ratio has a maxima for  $\epsilon = 1$ , corresponding to a circular pipe, hence emphasizing how deviation from a circle to ellipse reduces the hydraulic conductance of the pipe and hence efficiency of discharge per unit volume of the pipe. To emphasize this case we can consider two more example, of a square channel and of an equilateral triangle.

For the case of the square one obtains,

$$Q \simeq \frac{0.035144a^4}{\eta} \frac{\Delta p}{l} \quad (\text{B.18})$$

where  $a$  is the length of the side of the square. If we now evaluate the efficiency of discharge with respect to a circular pipe of same area we find,

$$\frac{Q}{Q_o} \simeq 0.88327 \quad (\text{B.19})$$

The reduced discharge is due to sharp corners, which is amplified in the case of an equilateral triangle for which  $Q/Q_o \simeq 0.72552$ .

## B.2 Influence of curvature on Poiseuille flow

If a pipe along its axis of symmetry develops significant curvature as is often the case in biological systems, purely axial flow of viscous fluid is no longer possible and secondary flows develop in the cross-sectional plane. For a fully developed steady flow in such a pipe with circular cross-section, the secondary flows develop primarily as two vortices parallel to the local centreline of the channel/pipe. As a result the maxima of the axial velocity is shifted outward.

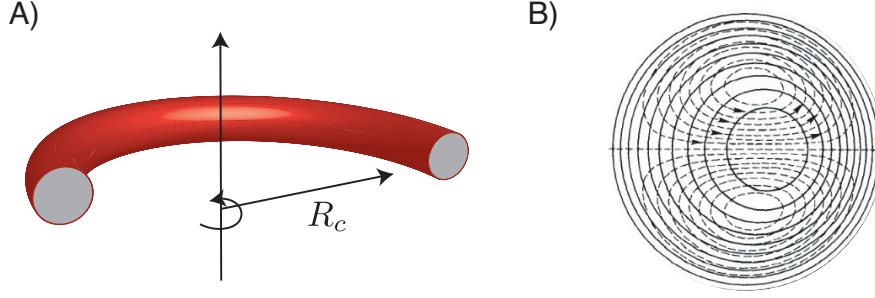


**Figure B.2:** (A) Schematic of a curved pipe is shown with radius of curvature  $R_c$  (B) Solid lines denote constant axial velocity contours while the dashed lines indicate secondary flow. (Adapted from [95])

Let us consider a pipe with uniform radius of curvature  $R_c$  of the centreline. The flow in such geometry is characterized by the Dean number  $\kappa = Re\sqrt{R/R_c}$ , where  $Re$  is the Reynold's number. A fluid element in the center of the pipe experiences an inward acceleration  $\sim \bar{v}^2/R_c$ , where  $\bar{v}$  is the average axial velocity. The body force is then resisted by viscous forces in the cross-section  $\sim \eta v_\perp/R^2$ , where  $v_\perp$  is the secondary flow velocity. A balance of these two effects yield,

$$\frac{v_\perp}{\bar{v}} \simeq Re \frac{R}{R_c} \quad (\text{B.20})$$

From this form one can see that for low  $Re$  the criteria for ignoring effect of curvature is simply  $R < R_c$ . If this criterion is satisfied, one can simply employ a perturbative analysis. One finds that the discharge rate with respect to a straight circular pipe can be fully characterized by the Dean number  $\kappa$ ,

$$\frac{Q}{Q_o} = 1 - 0.0306 \left(\frac{\kappa}{576}\right)^2 + 0.0120 \left(\frac{\kappa}{576}\right)^4 + O\left[\left(\frac{\kappa}{576}\right)^6\right] \quad (\text{B.21})$$

For a more elaborate discussion see [95].

## B.3 Influence of slip on Poiseuille flow

In an experimental system the assumption of no-slip at the boundary may not hold. In that case finite velocities at the boundary may exist and experimental characterization of such phenomena has been extensively exploited in the context of fluid-solid

boundaries. Conventionally, slip at the boundary is often discussed by introducing the concept of "slip length",  $\lambda$ . For example, for a circular pipe of radius  $R$ , the slip boundary condition is given by,

$$v_z(r = R) = -\lambda \frac{dv_z}{dr}$$

Hence the axial velocity is given by,

$$v_z(r) = -\frac{dp}{dz} \frac{R^2}{4\eta} \left( 1 - \frac{r^2}{R^2} + \frac{2\lambda}{R} \right) \quad (\text{B.22})$$

which does not distort the parabolic nature of the velocity profile however deviates linearly around. This leads to the discharge rate,

$$Q = -\frac{dp}{dz} \frac{\pi R^4}{8\eta} (1 + K_n) \quad (\text{B.23})$$

where  $K_n = \lambda/R$  is dimensionless number and has analogous interpretation to Knudsen number in gas flows. The deviation from a no-slip flow is hence,

$$\frac{Q}{Q_o} = 1 + 4\frac{\lambda}{R} \quad (\text{B.24})$$

We note that careful measurements of slip lengths on smooth solvophobic surfaces suggest  $\lambda \simeq 30nm$  [96]. In that case for a channel of radius  $10\mu m$ , the correction term  $4\lambda/R \simeq 4(30 \times 10^{-4}) \simeq 0.01$ , which corresponds to an 1% effect on the ideal flow.

Interestingly here the discharge rate and hence the amount of transported volume is higher than the ideal pipe due to extra flow at the boundary. Equivalently the hydraulic conductance is higher by a factor of  $4\lambda/R$ .



## B.4 Viscous flow through a leaky pipe

We have seen how the pressure profile is simply linear along the tube and has no intrinsic lengthscale and simply mimic the geometry. Let us consider a special case where the walls of the pipe are permeable/leaky and allow leakage across walls. This is of crucial importance to us as many biological tubes are leaky, especially the nematode germline. The tube is embedded within a fluid of constant pressure  $p_0$ . The pressure at the inlet  $z = 0$  is  $p_1 > p_0$ . The flow problem is described by,

$$\eta \frac{1}{r} \frac{\partial}{\partial r} \left( r \frac{\partial v_z}{\partial r} \right) = \frac{\partial p_z}{\partial z}, \frac{\partial p}{\partial r} = 0 \quad (\text{B.25})$$

with the boundary conditions:

$$v_r(0, z) = 0, v_z(R, z) = 0, v_r(R, z) = \kappa_w (p - p_0) \quad (\text{B.26})$$

This yields the same parabolic solution for  $v_z(r)$  and the discharge rate is again described by Eq.B.9. Now the continuity equation yields,

$$\frac{d}{dz} Q + 2\pi R v_r|_{r=R} = 0 \implies \frac{d^2 p}{dz^2} - \frac{16\eta\kappa_w}{R^3} (p - p_0) = 0 \quad (\text{B.27})$$

It is convenient to non-dimensionalize the equation with  $P = (p - p_0)/(p_1 - p_0)$  and  $Z = z/l$  so that we have,

$$\frac{d^2 P}{dZ^2} - \Lambda^2 P = 0 \quad (\text{B.28})$$

with the boundary conditions  $P(0) = 1$  &  $P(1) = 0$ . We have introduced  $\Lambda = (16\eta\kappa_w l^2/R^3)^{1/2}$ , which introduces a internal lengthscale  $\Lambda^{-1}$ . Note that the pressure here does not satisfy the Laplace's equation but rather the general form of Helmholtz equation, describing a general class of problems. of which Laplace's equation is a special case. The solution to the Eq.B.28 yields the pressure profile along the leaky tube as,

$$P(Z) = \frac{\sinh(\Lambda(1 - Z))}{\sinh \Lambda} \quad (\text{B.29})$$

and is plotted in Fig.B.3 B for different values of  $\Lambda$ . For  $\Lambda \ll 1$  one can use an expansion around  $\Lambda = 0$  to obtain,

$$P(Z) = 1 - Z + \frac{\Lambda^2}{6} Z(1 - Z)(Z - 2)$$

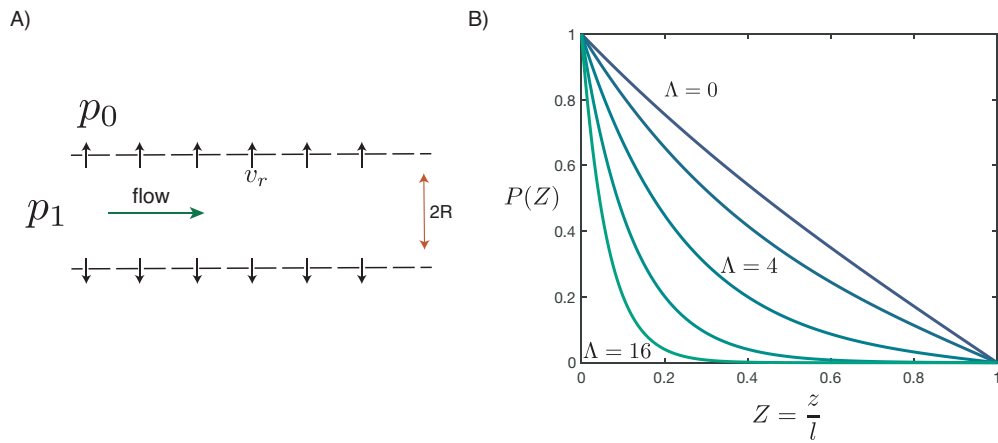


**Figure B.3:** (A) Schematic of a leaky pipe is shown with reference pressure  $p_0$  and inlet pressure  $p_1$  (B) Non-dimensional pressure profile  $P$  is plotted against non-dimensional axial position  $Z$  for various values of  $\Lambda = (16\eta\kappa_w l^2 / R^3)^{1/2}$

# Bibliography

- [1] N. T. Chartier, A. Mukherjee, J. Pfanzelter, S. Fürthauer, B. T. Larson, A. W. Fritsch, R. Amini, M. Kreysing, F. Jülicher, and S. W. Grill. A hydraulic instability drives the cell death decision in the nematode germline. *Nature Physics*, pages 1–6 (2021)
- [2] K. S. Thomson. *Morphogenesis and evolution*. Oxford University Press (1988)
- [3] J. B. Bard and J. Bard. *Morphogenesis: the cellular and molecular processes of developmental anatomy*, volume 23. Cambridge University Press (1992)
- [4] B. K. Hall. *Evolutionary developmental biology*. Springer Science & Business Media (2012)
- [5] D. W. Thompson et al. *On growth and form*. Cambridge Univ. Press (1942)
- [6] T. Lecuit. *Tissue remodeling and epithelial morphogenesis*, volume 89. Elsevier (2009)
- [7] A. M. Turing. The chemical basis of morphogenesis. *Bulletin of mathematical biology*, **52**(1-2): 153–197 (1990)
- [8] P. Roca-Cusachs, V. Conte, and X. Trepat. Quantifying forces in cell biology. *Nature cell biology*, **19**(7): 742–751 (2017)
- [9] S. Van Helvert, C. Storm, and P. Friedl. Mechanoreciprocity in cell migration. *Nature cell biology*, **20**(1): 8 (2018)
- [10] N. I. Petridou, Z. Spiró, and C.-P. Heisenberg. Multiscale force sensing in development. *Nature cell biology*, **19**(6): 581–588 (2017)
- [11] H. Honda and G. Eguchi. How much does the cell boundary contract in a monolayered cell sheet? *Journal of theoretical biology*, **84**(3): 575–588 (1980)
- [12] F. Graner and J. A. Glazier. Simulation of biological cell sorting using a two-dimensional extended potts model. *Physical review letters*, **69**(13): 2013 (1992)
- [13] R. Farhadifar, J.-C. Röper, B. Aigouy, S. Eaton, and F. Jülicher. The influence of cell mechanics, cell-cell interactions, and proliferation on epithelial packing. *Current Biology*, **17**(24): 2095–2104 (2007)
- [14] A. G. Fletcher, M. Osterfield, R. E. Baker, and S. Y. Shvartsman. Vertex models of epithelial morphogenesis. *Biophysical journal*, **106**(11): 2291–2304 (2014)
- [15] M. C. Gibson, A. B. Patel, R. Nagpal, and N. Perrimon. The emergence of geometric order in proliferating metazoan epithelia. *Nature*, **442**(7106): 1038–1041 (2006)
- [16] C. Bielmeier, S. Alt, V. Weichselberger, M. La Fortezza, H. Harz, F. Jülicher, G. Salbreux, and A.-K. Classen. Interface contractility between differently fated cells drives cell elimination and cyst formation. *Current Biology*, **26**(5): 563–574 (2016)
- [17] B. Monier, M. Gettings, G. Gay, T. Mangeat, S. Schott, A. Guarner, and M. Suzanne. Apico-basal forces exerted by apoptotic cells drive epithelium folding. *Nature*, **518**(7538): 245–248 (2015)

- [18] N. Kamiya. *Protoplasmic streaming*, volume 8. Springer Science & Business Media (2012)
- [19] R. E. Goldstein and J.-W. van de Meent. A physical perspective on cytoplasmic streaming. *Interface focus*, **5**(4): 20150030 (2015)
- [20] S. Ganguly, L. S. Williams, I. M. Palacios, and R. E. Goldstein. Cytoplasmic streaming in drosophila oocytes varies with kinesin activity and correlates with the microtubule cytoskeleton architecture. *Proceedings of the National Academy of Sciences*, **109**(38): 15109–15114 (2012)
- [21] K. Yi, J. R. Unruh, M. Deng, B. D. Slaughter, B. Rubinstein, and R. Li. Dynamic maintenance of asymmetric meiotic spindle position through arp2/3-complex-driven cytoplasmic streaming in mouse oocytes. *Nature cell biology*, **13**(10): 1252–1258 (2011)
- [22] L. D. Landau. *Fluid Mechanics: Volume 6*. Pergamon (1959)
- [23] J. Prost, F. Jülicher, and J.-F. Joanny. Active gel physics. *Nature physics*, **11**(2): 111–117 (2015)
- [24] S. Ramaswamy. The mechanics and statistics of active matter. *Annual Review of Condensed Matter Physics*, **1**(1): 323–345 (2010)
- [25] F. Jülicher, K. Kruse, J. Prost, and J.-F. Joanny. Active behavior of the cytoskeleton. *Physics reports*, **449**(1-3): 3–28 (2007)
- [26] F. Jülicher, S. W. Grill, and G. Salbreux. Hydrodynamic theory of active matter. *Reports on Progress in Physics*, **81**(7): 076601 (2018)
- [27] M. C. Marchetti, J.-F. Joanny, S. Ramaswamy, T. B. Liverpool, J. Prost, M. Rao, and R. A. Simha. Hydrodynamics of soft active matter. *Reviews of Modern Physics*, **85**(3): 1143 (2013)
- [28] J.-F. Joanny, K. Kruse, J. Prost, and S. Ramaswamy. The actin cortex as an active wetting layer. *The European Physical Journal E*, **36**(5): 1–6 (2013)
- [29] A. Mietke, F. Jülicher, and I. F. Sbalzarini. Self-organized shape dynamics of active surfaces. *Proceedings of the National Academy of Sciences*, **116**(1): 29–34 (2019)
- [30] V. Ruprecht, S. Wieser, A. Callan-Jones, M. Smutny, H. Morita, K. Sako, V. Barone, M. Ritsch-Marte, M. Sixt, R. Voituriez, et al. Cortical contractility triggers a stochastic switch to fast amoeboid cell motility. *Cell*, **160**(4): 673–685 (2015)
- [31] A. Reversat, F. Gaertner, J. Merrin, J. Stopp, S. Tasciyan, J. Aguilera, I. de Vries, R. Hauschild, M. Hons, M. Piel, et al. Cellular locomotion using environmental topography. *Nature*, pages 1–4 (2020)
- [32] H. Turlier, B. Audoly, J. Prost, and J.-F. Joanny. Furrow constriction in animal cell cytokinesis. *Biophysical journal*, **106**(1): 114–123 (2014)
- [33] A.-C. Reymann, F. Staniscia, A. Erzberger, G. Salbreux, and S. W. Grill. Cortical flow aligns actin filaments to form a furrow. *Elife*, **5**: e17807 (2016)
- [34] M. Mayer, M. Depken, J. S. Bois, F. Jülicher, and S. W. Grill. Anisotropies in cortical tension reveal the physical basis of polarizing cortical flows. *Nature*, **467**(7315): 617–621 (2010)

- [35] S. R. Naganathan, S. Fürthauer, M. Nishikawa, F. Jülicher, and S. W. Grill. Active torque generation by the actomyosin cell cortex drives left–right symmetry breaking. *Elife*, **3**: e04165 (2014)
- [36] L. G. Pimpale, T. C. Middelkoop, A. Mietke, and S. W. Grill. Cell lineage-dependent chiral actomyosin flows drive cellular rearrangements in early caenorhabditis elegans development. *Elife*, **9**: e54930 (2020)
- [37] S. J. Streichan, M. F. Lefebvre, N. Noll, E. F. Wieschaus, and B. I. Shraiman. Global morphogenetic flow is accurately predicted by the spatial distribution of myosin motors. *Elife*, **7**: e27454 (2018)
- [38] S. Münster, A. Jain, A. Mietke, A. Pavlopoulos, S. W. Grill, and P. Tomancak. Attachment of the blastoderm to the vitelline envelope affects gastrulation of insects. *Nature*, **568**(7752): 395–399 (2019)
- [39] M. De Cuevas, M. Lilly, and A. Spradling. Germline cyst formation in drosophila. *Annual review of genetics*, **31**(1): 405–428 (1997)
- [40] K. Haglund, I. P. Nezis, and H. Stenmark. Structure and functions of stable intercellular bridges formed by incomplete cytokinesis during development. *Communicative & integrative biology*, **4**(1): 1–9 (2011)
- [41] M. E. Pepling, M. De Cuevas, and A. C. Spradling. Germline cysts: a conserved phase of germ cell development? *Trends in cell biology*, **9**(7): 257–262 (1999)
- [42] D. N. Robinson and L. Cooley. Stable intercellular bridges in development: the cytoskeleton lining the tunnel. *Trends in cell biology*, **6**(12): 474–479 (1996)
- [43] E. Hubbard and D. Greenstein. Introduction to the germ line. *WormBook*, **1**(4) (2005)
- [44] J. Kimble and J. White. On the control of germ cell development in caenorhabditis elegans. *Developmental biology*, **81**(2): 208–219 (1981)
- [45] J. Austin and J. Kimble. glp-1 is required in the germ line for regulation of the decision between mitosis and meiosis in c. elegans. *Cell*, **51**(4): 589–599 (1987)
- [46] L. W. Berry, B. Westlund, and T. Schedl. Germ-line tumor formation caused by activation of glp-1, a caenorhabditis elegans member of the notch family of receptors. *Development*, **124**(4): 925–936 (1997)
- [47]
- [48] U. Wolke, E. A. Jezuit, and J. R. Priess. Actin-dependent cytoplasmic streaming in c. elegans oogenesis. *Development*, **134**(12): 2227–2236 (2007)
- [49] R. Amini, E. Goupil, S. Labella, M. Zetka, A. S. Maddox, J.-C. Labbé, and N. T. Chartier. C. elegans anillin proteins regulate intercellular bridge stability and germline syncytial organization. *Journal of Cell Biology*, **206**(1): 129–143 (2014)
- [50] J. Ranft, M. Basan, J. Elgeti, J.-F. Joanny, J. Prost, and F. Jülicher. Fluidization of tissues by cell division and apoptosis. *Proceedings of the National Academy of Sciences*, **107**(49): 20863–20868 (2010)
- [51] T. Bittig, O. Wartlick, A. Kicheva, M. González-Gaitán, and F. Jülicher. Dynamics of anisotropic tissue growth. *New Journal of Physics*, **10**(6): 063001 (2008)

- [52] T. Bittig, O. Wartlick, M. González-Gaitán, and F. Jülicher. Quantification of growth asymmetries in developing epithelia. *The European Physical Journal E*, **30**(1): 93–99 (2009)
- [53] R. Etournay, M. Popović, M. Merkel, A. Nandi, C. Blasse, B. Aigouy, H. Brandl, G. Myers, G. Salbreux, F. Jülicher, et al. Interplay of cell dynamics and epithelial tension during morphogenesis of the drosophila pupal wing. *Elife*, **4**: e07090 (2015)
- [54] I. Bonnet, P. Marcq, F. Bosveld, L. Fetler, Y. Bellaïche, and F. Graner. Mechanical state, material properties and continuous description of an epithelial tissue. *Journal of The Royal Society Interface*, **9**(75): 2614–2623 (2012)
- [55] T. L. Gumienny, E. Lambie, E. Hartweg, H. R. Horvitz, and M. O. Hengartner. Genetic control of programmed cell death in the caenorhabditis elegans hermaphrodite germline. *Development*, **126**(5): 1011–1022 (1999)
- [56] P. Campinho, M. Behrndt, J. Ranft, T. Risler, N. Minc, and C.-P. Heisenberg. Tension-oriented cell divisions limit anisotropic tissue tension in epithelial spreading during zebrafish epiboly. *Nature cell biology*, **15**(12): 1405–1414 (2013)
- [57] D. Krndija, F. El Marjou, B. Guirao, S. Richon, O. Leroy, Y. Bellaïche, E. Hannezo, and D. M. Vignjevic. Active cell migration is critical for steady-state epithelial turnover in the gut. *Science*, **365**(6454): 705–710 (2019)
- [58] S. Taheri-Araghi, S. Bradde, J. T. Sauls, N. S. Hill, P. A. Levin, J. Paulsson, M. Vergasola, and S. Jun. Cell-size control and homeostasis in bacteria. *Current biology*, **25**(3): 385–391 (2015)
- [59] S. Jun, F. Si, R. Pugatch, and M. Scott. Fundamental principles in bacterial physiology? history, recent progress, and the future with focus on cell size control: a review. *Reports on Progress in Physics*, **81**(5): 056601 (2018)
- [60] A. Shingleton. Allometry: the study of biological scaling. *Nature Education Knowledge*, **3**(10): 2 (2010)
- [61] P. B. Coulter. *Measuring inequality: A methodological handbook*. Routledge (2019)
- [62] C. E. Willert and M. Gharib. Digital particle image velocimetry. *Experiments in fluids*, **10**(4): 181–193 (1991)
- [63] R. J. Adrian. Twenty years of particle image velocimetry. *Experiments in fluids*, **39**(2): 159–169 (2005)
- [64] L. Adrian, R. J. Adrian, and J. Westerweel. *Particle image velocimetry*. 30. Cambridge university press (2011)
- [65] W. Thielicke and E. Stamhuis. Pivlab—towards user-friendly, affordable and accurate digital particle image velocimetry in matlab. *Journal of Open Research Software*, **2**(1) (2014)
- [66] J. Happel and H. Brenner. *Low Reynolds number hydrodynamics: with special applications to particulate media*, volume 1. Springer Science & Business Media (2012)
- [67] C. K. Batchelor and G. Batchelor. *An introduction to fluid dynamics*. Cambridge university press (2000)
- [68] D. J. Acheson. *Elementary fluid dynamics*. Acoustical Society of America (1991)

- [69] L. D. Landau and E. M. Lifshitz. *Fluid mechanics 2nd ed.* Pergamon Press (1987)
- [70] F. Weinhaus and W. Barker. On the equilibrium states of interconnected bubbles or balloons. *American Journal of Physics*, **46**(10): 978–982 (1978)
- [71] W. Dreyer, I. Müller, and P. Strehlow. A study of equilibria of interconnected balloons. *The Quarterly Journal of Mechanics and Applied Mathematics*, **35**(3): 419–440 (1982)
- [72] R. A. Sampson. Xii. on stokes,Äôs current function. *Philosophical Transactions of the Royal Society of London.(A.)*, (182): 449–518 (1891)
- [73] R. Roscoe. Xxxi. the flow of viscous fluids round plane obstacles. *The London, Edinburgh, and Dublin Philosophical Magazine and Journal of Science*, **40**(302): 338–351 (1949)
- [74] R. J. Ryham. On the viscous flows of leak-out and spherical cap natation. *Journal of Fluid Mechanics*, **836**: 502–531 (2018)
- [75] J. Kierzenka and L. F. Shampine. A bvp solver based on residual control and the maltab pse. *ACM Transactions on Mathematical Software (TOMS)*, **27**(3): 299–316 (2001)
- [76] J. Kierzenka and L. F. Shampine. A bvp solver that controls residual and error. *JNAIAM J. Numer. Anal. Ind. Appl. Math*, **3**(1-2): 27–41 (2008)
- [77] S. Alt. *Epithelial mechanics in 3D - how form follows force*. Dissertation, Technische Universität Dresden (2016)
- [78] S. Alt, P. Ganguly, and G. Salbreux. Vertex models: from cell mechanics to tissue morphogenesis. *Philosophical Transactions of the Royal Society B: Biological Sciences*, **372**(1720): 20150520 (2017)
- [79] H. A. Messal, S. Alt, R. M. Ferreira, C. Gribben, V. M.-Y. Wang, C. G. Cotoi, G. Salbreux, and A. Behrens. Tissue curvature and apicobasal mechanical tension imbalance instruct cancer morphogenesis. *Nature*, **566**(7742): 126–130 (2019)
- [80] K. Rehai-Bell, A. Love, M. E. Werner, I. MacLeod, J. R. Yates III, and A. S. Maddox. A sterile 20 family kinase and its co-factor ccm-3 regulate contractile ring proteins on germline intercellular bridges. *Current Biology*, **27**(6): 860–867 (2017)
- [81] J. I. Alsous, N. Romeo, J. A. Jackson, F. Mason, J. Dunkel, and A. C. Martin. Dynamics of hydraulic and contractile wave-mediated fluid transport during drosophila oogenesis. *bioRxiv* (2020)
- [82] J. Hofbauer, K. Sigmund, et al. *Evolutionary games and population dynamics*. Cambridge university press (1998)
- [83] M. A. Nowak. *Evolutionary dynamics: exploring the equations of life*. Harvard university press (2006)
- [84] N. W. Goehring and A. A. Hyman. Organelle growth control through limiting pools of cytoplasmic components. *Current Biology*, **22**(9): R330–R339 (2012)
- [85] S. C. Weber and C. P. Brangwynne. Inverse size scaling of the nucleolus by a concentration-dependent phase transition. *Current Biology*, **25**(5): 641–646 (2015)
- [86] S. Uppaluri, S. C. Weber, and C. P. Brangwynne. Hierarchical size scaling during multicellular growth and development. *Cell Reports*, **17**(2): 345–352 (2016)

- [87] D. L. Levy and R. Heald. Mechanisms of intracellular scaling. *Annual review of cell and developmental biology*, **28**: 113–135 (2012)
- [88] E. M. Rieckhoff, K. Ishihara, and J. Brugués. How to tune spindle size relative to cell size? *Current opinion in cell biology*, **60**: 139–144 (2019)
- [89] E. Rieckhoff, F. Berndt, S. Golfier, F. Decker, M. Elsner, K. Ishihara, and J. Brugués. Spindle scaling is governed by cell boundary regulation of microtubule nucleation. *bioRxiv* (2020)
- [90] C. C. Wesley, S. Mishra, and D. L. Levy. Organelle size scaling over embryonic development. *Wiley Interdisciplinary Reviews: Developmental Biology*, page e375 (2020)
- [91] E. Kussell and S. Leibler. Phenotypic diversity, population growth, and information in fluctuating environments. *Science*, **309**(5743): 2075–2078 (2005)
- [92] J. N. Carey and M. Goulian. A bacterial signaling system regulates noise to enable bet hedging. *Current genetics*, **65**(1): 65–70 (2019)
- [93] M. Acar, J. T. Mettetal, and A. Van Oudenaarden. Stochastic switching as a survival strategy in fluctuating environments. *Nature genetics*, **40**(4): 471–475 (2008)
- [94] S. P. Sutera and R. Skalak. The history of poiseuille’s law. *Annual review of fluid mechanics*, **25**(1): 1–20 (1993)
- [95] S. Berger, L. Talbot, and L. Yao. Flow in curved pipes. *Annual review of fluid mechanics*, **15**(1): 461–512 (1983)
- [96] L. Bocquet and E. Charlaix. Nanofluidics, from bulk to interfaces. *Chemical Society Reviews*, **39**(3): 1073–1095 (2010)





# Versicherung

Hiermit versichere ich, dass ich die vorliegende Arbeit ohne unzulässige Hilfe Dritter und ohne Benutzung anderer als der angegebenen Hilfsmittel angefertigt habe; die aus fremden Quellen direkt oder indirekt übernommenen Gedanken sind als solche kenntlich gemacht. Die Arbeit wurde bisher weder im Inland noch im Ausland in gleicher oder ähnlicher Form einer anderen Prüfungsbehörde vorgelegt. Die Arbeit wurde in Dresden am Max-Planck-Institut für Physik komplexer Systeme unter der Betreuung von Prof. Frank Jülicher und am Max-Planck-Institut für molekulare Zellbiologie und Genetik unter der Betreuung von Prof. Stephan W. Grill angefertigt.

---

Arghyadip Mukherjee  
Dresden, November 2020